Max-Planck-Institut für Kolloid- und Grenzflächenforschung
Forschungsgruppe Mechano(bio)chemie

Molecular Control of Extracellular Matrix-inspired Biohybrid Hydrogels

Dissertation

zur Erlangung des akademischen Grades
"doctor rerum naturalium"
(Dr. rer. nat.)
im Promotionsfach "Chemie"
mit Spezialisierung "Angewandte Analytik und Umweltchemie"

eingereicht an der
Mathematisch-Naturwissenschaftlichen Fakultät
der Humboldt-Universität zu Berlin

von

Geonho Song

Gutachter/innen:
Prof. Dr. Kannan Balasubramanian
Prof. Dr. Kerstin G. Blank
Prof. Dr. Jürgen P. Rabe

Datum der Verteidigung: 07. April 2022

(komm.) Präsident der Humboldt-Universität zu Berlin
Prof. Dr. Peter Frensch

Dekan der Mathematisch-Naturwissenschaftlichen Fakultät
Prof. Dr. Elmar Kulke

Declaration of Originality

The research in this dissertation, submitted to the Department of Chemistry at the Humboldt University of Berlin, has been performed from January 2018 to November 2021 in the Max Planck research group Mechano(bio)chemistry under the supervision of Prof. Dr. Kerstin G. Blank at the Max Planck Institute of Colloids and Interfaces (MPIKG), Germany. I declare that I have completed the thesis independently using only the aids and tools specified. I have not applied for a doctor's degree in the doctoral subject elsewhere and do not hold a corresponding doctor's degree. I have taken due note of the Faculty of Mathematics and Natural Sciences PhD Regulations, published in the Official Gazette of Humboldt-Universität zu Berlin no. 42/2018 on 11/07/2018.

Eidesstattliche Erklärung

Die Forschungsarbeit der vorliegenden Dissertation wurde am Institut für Chemie an der Humboldt-Universität zu Berlin eingereicht. Diese Dissertation wurde im Zeitraum von Januar 2018 bis November 2021 in der Max-Planck-Forschungsgruppe Mechano(bio)chemie unter der Leitung von Prof. Dr. Kerstin G. Blank am Max-Planck-Institut für Kolloid- und Grenzflächenforschung (MPIKG) in Potsdam angefertigt. Hiermit versichere ich an Eides statt, dass die vorliegende Dissertation von mir eigenständig und ausschließlich unter Verwendung der zitierten Literatur und Hilfsmittel erstellt wurde. Die Dissertation wurde bisher nicht in gleicher oder ähnlicher Form einer anderen Prüfungsbehörde zur Erlangung eines akademischen Grades vorgelegt und ich führe keinen Doktorgrad in einer vergleichbaren Disziplin. Ich habe die Promotionsordnung der Mathematisch-Naturwissenschaftlichen Fakultät in Kenntnis genommen, die im Amtlichen Mitteilungsblatt der Humboldt-Universität zu Berlin Nr. 42/2018 am 11.07.2018 veröffentlicht wurde.

Geonho Song

Berlin, November 2021

Summary

Understanding natural biological materials and utilizing the obtained knowledge for the development of novel biomimetic materials has drawn enormous attention from the areas of chemistry and material science. In many complex biomolecular materials, proteins are the main building blocks. Establishing their molecular structure-function relationships thus forms the basis for understanding the emerging properties of various biological soft materials, such as the extracellular matrix (ECM). Inspired by common association motifs of ECM proteins, simplified model peptides have been developed for functional studies and as biomimetic building blocks for synthetic biomaterials. Used as hydrogel building blocks, these peptides can, for example, mimic several features of the respective ECM proteins, such as self-assembly and stimuli-responsiveness. In general, ECM-inspired biomaterials are in high demand for many biological applications such as cell culture and tissue engineering as well as soft electronics and robotics. Despite this strongly growing need, general principles for establishing bottom-up control of the viscoelastic properties of such materials is still lacking.

The aim of this thesis was to utilize ECM-inspired and molecularly controlled model peptides for the synthesis of peptide-polymer hybrid hydrogels. Specifically, collagen-mimetic peptides (CMPs) and coiled coil (CC)-forming peptides were utilized to crosslink the biocompatible and hydrophilic polymer poly(ethylene glycol) (PEG), making use of the ability of these peptides to dynamically self-assemble. A series of different CMPs and CCs were designed with the goal of investigating the relationship between the molecular crosslink characteristics and the bulk viscoelastic properties of the resulting hydrogels. In more detail, a set of CMPs was utilized to investigate how their kinetic properties affect stress relaxation in the resulting hydrogel networks. CCs of different oligomerization states were employed to test how the resulting crosslink functionality determined the linear viscoelastic range, the overall material stiffness as well as the linear and non-linear viscoelastic properties.

In the CMP-crosslinked hydrogel network, the three sequences $(POG)_7$, $(POG)_{10}$ and $(PPG)_{10}$ were used, as both length and sequence are known to be responsible for the thermodynamic and kinetic stability of the folded collagen triple helical structures. The two CMPs $(POG)_7$ and $(PPG)_{10}$ showed similar thermodynamic stabilities (i.e. melting temperatures, T_m) of approximately 30 °C, while T_m was ~60 °C for $(POG)_{10}$. In line with the thermodynamic stability, $(POG)_7$ and $(PPG)_{10}$ also displayed faster apparent dissociation kinetics when compared to $(POG)_{10}$. As a result of the extremely slow dissociation rate of $(POG)_{10}$, the resulting hydrogel exhibited aging and compressed exponential stress relaxation. In contrast, the other CMP-crosslinked hydrogels showed commonly observed stretched exponents. Compressed

exponential relaxation has rarely been observed for hydrogels, although a similar relaxation behavior has been seen for a number of different soft glassy materials, such as colloidal gels and concentrated emulsions. Even though the presence of non-equilibrium structures and jamming has been discussed as the source of compressed exponential relaxation, the underlying mechanisms had not yet been elucidated. In this work, knowledge of the molecular crosslink properties allowed for establishing a direct link between the dissociation kinetics of the crosslinks with the relaxation behavior of the network. This result was further confirmed in temperature-controlled stress relaxation tests. Lowering the temperature to reduce the dissociation rates of $(POG)_7$ and $(PPG)_{10}$ shifted their relaxation behavior into the compressed exponential regime. The hydrogel presented here is thus the first example of an out-of-equilibrium soft material system where compressed exponential stress relaxation can be directly linked to the kinetic parameters of its molecular constituents.

The timescales of stress relaxation are frequently linked to the kinetics of the crosslinks; however, increasing evidence shows that also the crosslink functionality critically determines the viscoelastic behavior of the network. CMPs always form a trimeric superhelical assembly, leading to a crosslink functionality of 3. To investigate the importance of this parameter, the CMPs were replaced with CCs. The oligomerization state of CC superhelices is easily altered when exchanging residues in the hydrophobic core. Dimeric, trimeric and tetrameric CCs were employed to obtain dynamic crosslinks with functionalities between 2 and 4. These were combined with linear (2 arms) or star-shaped PEG (4 arms), where the PEG additionally introduces covalent crosslink junctions with functionalities of 2 and 4. The hydrogels with the largest linear viscoelastic range were obtained when either the covalent or the dynamic crosslink had a functionality of 2. Increasing the crosslink functionality, decreased the effective chain length and the hydrogels failed at smaller strains. Furthermore, the stiffness and viscoelastic properties of the resulting hydrogels appeared to depend more strongly on the crosslink functionality than on the thermodynamic stabilities of the dynamic CC crosslinks. In combination, these results clearly show the importance of network topology as a key parameter for tuning the properties of dynamically crosslinked hydrogels.

Rheology is a powerful method to determine the bulk material properties; however, the fate of dynamic crosslinks upon mechanical deformation or stress relaxation cannot be observed in real-time. In contrast, optical spectroscopy provides molecular insights into the structure and kinetics of self-assembling protein and peptide-building blocks. Towards the long-term goal of integrating rheology with optical detection methods, a self-reporter system using a conventional fluorophore was implemented for real-time pictures about the assembly of CMPs. If used in the hydrogel network, this strategy could allow for quantifying the ratio of free peptides vs. folded CMPs (i.e. crosslinks) as well as their dissociation and association kinetics

during deformation and subsequent self-healing. When 5(6)-carboxyfluorescein (CF) was coupled at the N-terminus of chemically synthesized CMPs, the fluorescence was reduced as a result of fluorescence self-quenching (FSQ). In addition, the fluorescence intensity increased approximately 4-fold upon thermal or chemical denaturation; however, no significant increase in fluorescence was observed in a kinetic measurement where unlabeled CMPs were added as a competitor. This is most likely a result of the extremely slow dissociation rates of the CMPs at room temperature. Considering the comparably small intensity difference between free peptides and folded CMPs as well as the slow dissociation kinetics, self-quenched CMPs may not yield the desired self-reporting system for hydrogels. Possibly CC heterooligomers, equipped with a Förster resonance energy transfer (FRET) reporter system, may be a more suitable choice that can be implemented in the future.

In summary, this dissertation utilized ECM-inspired model peptides as physical and dynamic crosslinks. Using such molecularly controlled peptides, integrated into a well-defined, synthetic polymer network, allowed for investigating the influence of molecular crosslink properties on the rheological behavior of the resulting hydrogels. Employing CMPs with slow dissociation kinetics, hydrogels have been synthesized that resemble soft glassy materials with compressed exponential relaxation and aging. Furthermore, network connectivity has been shown to be an underutilized design parameter for tuning the rheological properties of hydrogels. Combining molecularly controlled crosslinks with a fluorescence reporter system that allows to read out crosslink status will ultimately allow for more detailed insights into the response of such networks to mechanical perturbation and thus aid the synthesis of ECM-inspired biomaterials with tunable and self-reporting properties.

Zusammenfassung

Das Verständnis natürlicher biologischen Materialien und die Nutzung des erworbenen Wissens für die Entwicklung neuer biomimetischer Materialien ist von großem Interesse in der Chemie und den Materialwissenschaften. In vielen komplexen biomolekularen Materialien sind Proteine die Hauptbausteine. Die Etablierung der Struktur-Funktionsbeziehungen dieser Proteinbausteine ist notwendig, um die Eigenschaften der daraus aufgebauten weichen, biologischen Materialien zu verstehen, wie z. B. die extrazelluläre Matrix (*extracellular matrix - ECM*). Inspiriert durch bekannte Faltungsmotive von ECM-Proteinen, wurden vereinfachte Modellpeptide entwickelt, um deren Funktion zu untersuchen oder diese als biomimetische Bausteine für synthetische Biomaterialien zu verwenden. Diese Modellpeptide besitzen die grundlegenden Eigenschaften der jeweiligen ECM-Proteine, wie z. B. die Fähigkeit zur Selbstassemblierung oder die Reaktion auf externe Stimuli. Im Allgemeinen gibt es eine große Nachfrage für ECM-mimetische Biomaterialien. Diese werden in vielen biologischen Anwendungsbereichen wie der Zellkultur und der Gewebezüchtung (*tissue engineering*) genutzt, sowie der weichen Elektronik (*soft electronics*) und Robotik (*soft robotics*). Trotz des wachsenden Bedarfs, fehlen allgemeine Prinzipien, die es erlauben, die viskoelastische Eigenschaften der Materialien auf molekularen Ebene zu bestimmen und anzupassen.

Ziel dieser Arbeit war die Synthese von hybriden Hydrogelen, die aus einem synthetischen Polymer und ECM-inspirierten Modellpeptiden zusammengesetzt sind. Insbesondere Kollagen-mimetische Peptide (*collagen-mimetic peptides - CMPs*) und Coiled-Coil-formende Peptide (CCs) wurden benutzt, um das biokompatible und hydrophile Polymer Polyethyleneglykol (PEG) zu vernetzen. Dabei wurde von der Fähigkeit dieser Peptide zur dynamischen Selbstassemblierung Gebrauch gemacht. Verschiedener CMPs und CCs wurden entworfen, mit dem Ziel die Zusammenhänge zwischen den Eigenschaften molekularer Vernetzer und den makroskopischen viskoelastischen Eigenschaften der resultierenden Hydrogele zu untersuchen. Unter Verwendung einer Reihe von CMPs wurde der Einfluss ihrer kinetischen Eigenschaften auf die Spannungsrelaxation der Hydrogelnetzwerke untersucht. Darüber hinaus wurden CCs unterschiedlicher Oligomerisierungsgrade verwendet, um zu testen, wie die Funktionalität der resultierenden Vernetzer den linearen viskoelastischen Bereich und die allgemeine Steifigkeit des Materials bestimmt, sowie die linearen und nichtlinearen viskoelastischen Eigenschaften beeinflusst.

Für das CMP-vernetzte Hydrogel wurden die drei Sequenzen $(POG)_7$, $(POG)_{10}$ und $(PPG)_{10}$ benutzt. Es ist bekannt, dass sowohl die Länge als auch die Sequenz der CMPs für die thermodynamische und kinetische Stabilität der assemblierten und gefalteten Kollagen-

Tripelhelix verantwortlich sind. Die CMPs (POG)$_7$ und (PPG)$_{10}$ besitzen eine ähnliche thermodynamische Stabilität mit einer Schmelztemperatur von ca. 30 °C, wohingegen diese für (POG)$_{10}$ etwa 60 °C betrug. In Übereinstimmung mit der thermodynamischen Stabilität besaßen (POG)$_7$ und (PPG)$_{10}$ auch eine schnellere Dissoziationsrate im Vergleich zu (POG)$_{10}$. Basierend auf der extrem langsamen Dissoziationsrate von (POG)$_{10}$ zeigte das resultierende Hydrogel eine sogenannte gestauchte exponentielle Spannungsrelaxation (*compressed exponential relaxation*) sowie einen Alterungsprozess. Im Gegensatz dazu wiesen die anderen CMP-vernetzten Hydrogele das häufig beobachtete gestreckte exponentielle Relaxationsverhalten auf (*stretched exponential relaxation*). Eine gestauchte exponentielle Spannungsrelaxation wurde bisher nicht bei Hydrogelen beobachtet. Dieses Relaxationsverhalten ist jedoch charakteristisch für eine Reihe weicher, glasartiger Materialien (wie z. B. kolloidale Gele und konzentrierte Emulsionen). Als Ursache für das gestauchte exponentielle Verhalten werden Nichtgleichgewichtsstrukturen und eine sogenannte Staubildung (*jamming*) diskutiert. Allerdings ist über die zugrundeliegenden Mechanismen wenig bekannt. Basierend auf der Kenntnis der molekularen Eigenschaften, konnte in der vorliegenden Arbeit eine direkte Verbindung zwischen der Dissoziationskinetik der molekularen Vernetzer und dem Relaxationsverhalten des Netzwerks hergestellt werden. Dieses Ergebnis wurde durch temperaturabhängige Spannungsrelaxationstests bestärkt. Durch die Herabsetzung der Temperatur, und die daraus folgende Reduktion der Dissoziationsrate, wurde das Relaxationsverhalten der (POG)$_7$- und (PPG)$_{10}$-vernetzten Hydrogele in den Bereich der gestauchten exponentiellen Relaxation verschoben. Die hier präsentierten Hydrogele sind die ersten Beispiele eines weichen Materials im Nichtgleichgewicht, bei dem diese Relaxationseigenschaften direkt mit den kinetischen Parametern der molekularen Bestandteile in einen Zusammenhang gebracht werden können.

Die Zeitskalen der Spannungsrelaxation werden oft mit den kinetischen Eigenschaften der Vernetzer in Verbindung gebracht. Jedoch gibt es vermehrt Hinweise darauf, dass auch die Funktionalität der Vernetzer das viskoelastische Verhalten des Netzwerkes maßgeblich mitbestimmt. Mit ihrer trimeren Superhelixstruktur, besitzen CMP-Vernetzer grundsätzlich eine Funktionalität von 3. Um die Wichtigkeit dieses Parameters im Detail zu untersuchen, wurden die CMPs mit CCs ersetzt. Ihr Oligomerisierungsgrad kann leicht variiert werden, indem die Aminosäuren im hydrophoben Kern des CCs ausgetauscht werden. In dieser Arbeit wurden dimere, trimere und tetramere CCs benutzt, um dynamische Vernetzer mit Funktionalitäten von 2 bis 4 zu erhalten. Die entsprechenden CC-Vernetzer wurden entweder mit linearem PEG (zweiarmig) oder sternförmigem PEG (vierarmig) kombiniert, wobei das PEG zusätzlich kovalente Vernetzungspunkte mit Funktionalitäten von 2 und 4 darstellt. Die Hydrogele wiesen den größten linearen viskoelastischen Bereich auf, wenn entweder die

kovalenten oder dynamischen Vernetzer eine Funktionalität von 2 besaßen. Die Erhöhung der Funktionalität führte zu einer Verkürzung der effektiven Polymerlänge, so dass das Hydrogel bereits bei kleinerer Spannung brach. Des Weiteren zeigten die Steifigkeit und die viskoelastischen Eigenschaften eine stärkere Abhängigkeit von der Vernetzerfunktionalität als von den thermodynamischen Stabilitäten der dynamischen CC-Vernetzer. Zusammenfassend zeigen diese Ergebnisse die Bedeutung der Netzwerktopologie als Schlüsselparameter, um die viskoelastischen Eigenschaften dynamisch vernetzter Hydrogelen zu bestimmen.

Die Rheologie ist eine leistungsstarke Methode, um makroskopische Materialeigenschaften zu bestimmen. Jedoch kann das Verhalten dynamischer Vernetzer bei mechanischer Deformation oder Spannungsrelaxation nicht in Echtzeit beobachtet werden. Im Gegensatz dazu liefert die optische Spektroskopie strukturelle und kinetische Information über selbstassemblierende Proteine und Peptidbausteinene. Mit dem langfristigen Ziel Rheologie mit optischen Detektionstechniken zu integrieren, wurde ein Fluoreszenz-Reportersystem getestet, das potenziell über den Assemblierungszustand der CMPs im Hydrogelnetzwerk informieren kann. Insbesondere sollte das Verhältnis von freien Peptiden zu gefalteten CMP-Vernetzern quantifiziert werden, sowie deren Dissoziations- und Assoziationskinetik während einer Deformation und der darauffolgenden Selbstheilung. Dazu wurde an den N-Terminus von chemisch synthetisierten CMPs 5(6)-Carboxyfluorescein gekoppelt. Im assemblierten Zustand nahm die Fluoreszenz durch Fluoreszenzlöschung (*fluorescence self-quenching*) ab. Gleichzeitig nahm nach einer thermischen oder chemischen Denaturierung die Intensität der Fluoreszenz um das Vierfache zu. Jedoch wurde kein signifikanter Anstieg der Fluoreszenz in einer kinetischen Messung beobachtet, bei der nicht Fluoreszenz-markierte CMPs als Kompetitor eingesetzt wurden. Dieses Ergebnis resultiert höchstwahrscheinlich aus den sehr langsamen Dissoziationsraten der verwendeten CMPs bei Raumtemperatur. Aufgrund der vergleichsweise kleinen Intensitätsunterschiede zwischen freien Peptiden und assemblierten CMPs, sowie der langsamen Dissoziationskinetik, erscheint das verwendete Reportersystem für Hydrogele wenig geeignet. Als Alternative für zukünftige Anwendungen könnten CC-Heterooligomere dienen, die mit einem Förster-Resonanzenergietransfer-Reportersystem ausgestattet sind.

Zusammenfassend wurden Im Rahmen dieser Dissertation ECM-inspirierte Modellpeptide als physikalische und dynamische Vernetzer für Hydrogele eingesetzt. Eine Vielzahl an Eigenschaften dieser Modellpeptide ist auf molekularer Ebene kontrollierbar, so dass wohldefinierte, synthetische Polymernetzwerke hergestellt werden konnten. Dies ermöglichte es, den Einfluss der molekularen Vernetzereigenschaften auf das rheologische Verhalten der resultierenden Hydrogele zu untersuchen. Unter Verwendung von Kollagen-mimetischen Peptiden mit langsamer Dissoziationskinetik wurden Hydrogele synthetisiert, die weichen,

glasartigen Materialien mit einem gestauchten exponentiellen Relaxationsverhalten entsprechen und auch einen Alterungsprozess zeigen. Darüber hinaus wurde gezeigt, dass Netzwerkkonnektivität ein bis dato selten gebrauchter Designparameter ist, um die rheologischen Eigenschaften von Hydrogelen nach Wunsch zu kontrollieren. Die Kombination molekular einstellbarer Vernetzer mit einem Fluoreszenz-Reportersystem, welches deren Zustand auslesen kann, kann detaillierte Einblicke in das Reaktionsvermögen solcher Netzwerke auf mechanische Stimuli ermöglichen. Das Verständnis molekularer Prozesse erlaubt langfristig die Synthese von ECM-inspirierten Biomaterialien, deren Eigenschaften nach Wunsch einstellbar sind und die selbst ihren mikroskopischen und mesoskopischen Zustand anzeigen (*self-reporting*).

Table of contents

Abbreviations

A	absorbance
ACN	acetonitrile
AS	amplitude sweep
Boc	t-butoxyloxycarbonyl
Bzl	benzyl
CC	coiled coil
CD	circular dichroism
CF	5(6)-carboxyfluorescein
CMP	collagen-mimetic peptide
conc.	concentration
CSK	cytoskeleton
CTH	collagen triple helix
DHB	2,5-dihydroxybenzoic acid
DIPEA	N,N-diisopropylethylamine
DMF	dimethylformamide
DOPA	3,4-dihydroxyphenylalanine
d	diameter
ECM	extracellular matrix
EDT	ethane-1,2-dithiol
EDTA	ethylenediamine tetraacetic acid
Fmoc	fluorenylmethyloxycarbonyl
FRET	Förster resonance energy transfer
FS	frequency sweep
FSQ	fluorescence self-quenching
GdmCl	Guanidinium chloride
HCTU	O-(1H-6-Chlorobenzotriazole-1-yl)-1,1,3,3-tetramethyluronium hexafluorophosphate
Hetero2	heterodimer
HF	hydrofluoric acid
Homo2	homodimer
Homo3	homotrimer
Homo4	homotetramer

KWW	Kohlrausch-Williams-Watts
L	left-handed, counter-clockwise
linear-PEG	linear-shaped poly(ethylene glycol), 2-arm poly(ethylene glycol)
LAOS	large-amplitude oscillatory shear
LVE	linear viscoelastic
LVER	linear viscoelastic region
MALDI	matrix-assisted laser desorption/ionization
ME	molar ellipticity
MS	mass spectrometer
NHS	N-hydroxysuccinimide
NMR	nuclear magnetic resonance
NP	normal-phase
PEG	poly(ethylene glycol)
PG	protecting group
PPII	polyproline II
PyAOP	(7-azabenzotriazol-1-yloxy)tripyrrolidinophosphonium hexafluorophosphate
R	right-handed, clockwise
R_g	radius of gyration
R_h	hydrodynamic radius
RT	room temperature
RP	reverse-phase
RS	rotatory sweep
SAOS	small-amplitude oscillatory shear
SEC	size-exclusion chromatography
SGM	soft glassy material
star-PEG	star-shaped poly(ethylene glycol)
SPPS	solid-phase peptide synthesis
SR	stress relaxation
TCEP	tris(2-carboxyethyl)phosphine
TFA	trifluoroacetic acid
TIPS	triisopropylsilane
TOF	time-of-flight

1   Introduction

Interest in biomimetic and bioinspired materials has grown enormously over the last decades, both in the research fields of chemistry and materials science [1, 2]. Knowledge about biological materials has increased tremendously [3] and their unique characteristics are now well described, including hierarchical structure, multifunctionality, and self-organization. These principles increasingly find application for the development of novel biomaterials that mimic and are inspired from natural systems [4].

Hydrogels, defined as chemically and/or physically crosslinked polymeric networks, are at the forefront of this field. As a direct result of their hydrophilic three-dimensional nature, they have high water content and viscoelastic properties similar to most soft biological materials. These include the mammalian cytoskeleton (CSK) [5] and the extracellular matrix (ECM) [6]. Biomimetic and bioinspired hydrogels show promising biomedical applications, e.g. as cell culture matrices [7] in tissue engineering [8]. They further find use in the emerging area of soft robotics, where they can be utilized as sensors [9] or actuators [10].

Protein-based biopolymers serve as a great platform for the synthesis of bioinspired hydrogels as they are biocompatible, tunable at the amino acid level and sensitive to external cues (e.g. temperature, pH, light, electric/magnetic fields and chemical triggers) [11-15]. Proteins or peptides can be engineered as hydrogel building blocks and utilized to mimic natural protein-based soft materials, such as collagen, keratin and elastin [4, 16, 17], or protein-containing composite materials, such as chitin, bone or nacre. Even though the protein building blocks of many biological materials are increasingly characterized and utilized, knowledge about the relationship between molecular structures and bulk mechanical properties of the resulting materials are often poorly understood.

In this work, I have developed biomimetic and bioinspired hydrogels based on different protein association motifs found in the CSK and the ECM. Specifically, I have utilized triple helical CMPs and *de novo* designed CC superhelical structures to physically (i.e. dynamically) crosslink the well-characterized polymer polyethylene glycol (PEG). The thermodynamic and kinetic properties of the self-assembled supramolecular peptide structures were tuned based on the amino acid sequence and length as molecular design parameters. These parameters are expected to determine the bulk viscoelastic properties of the resulting peptide-polymer hybrid hydrogels. The molecular characteristics of the peptides used were studied with spectroscopic methods (e.g. circular dichroism (CD) and fluorescence spectroscopy) to establish a link between the thermodynamic/kinetic properties of the peptides and the

viscoelastic properties of the resulting peptide-crosslinked bulk materials, measured with shear rheology.

In this introduction, I will give the fundamental information about the CSK and the ECM as a source of biomimicry and bioinspiration and the essential design parameters of the CMP and CC protein association motifs, utilized as dynamic crosslinks in peptide-polymer hybrid hydrogels. Also, I will describe examples of biomimetic and bioinspired hydrogels and their physical and chemical properties. Furthermore, I will introduce how such bio-inspired crosslinks can be converted into a fluorescence-based system that self-reports on the kinetics of peptide association and dissociation and, as an outlook, also on the assembly state of the resulting hydrogel network.

1.1   The extracellular matrix as a viscoelastic biopolymeric network

The ECM primarily consists of fibrous proteins (e.g. collagen, elastin, fibronectin, laminin), polysaccharides (e.g. proteoglycans) and enzymes as well as biominerals (e.g. hydroxyl-apatite) [18]. It mainly serves as a scaffold network, providing physical and mechanical support for cells growing within tissues. Recently, various roles in biochemical and biomechanical processes have also been highlighted, such as tissue morphogenesis, differentiation and homeostasis [19]. During tissue development, the ECM organizes into a tissue-specific composition and topology, shaped through cell-ECM interactions (**Figure 1**).

Different ECMs are heterogeneous in composition and architecture. This is caused by the intrinsic disorder of the fibrous protein-based network, which is filled with proteoglycans in the interstitial spaces [20]. As a direct result of its fibrous nature, the ECM network displays non-linear elasticity, dynamic network remodeling as well as structural and mechanical heterogeneity [21, 22]. In addition to this heterogeneity, cell-ECM interactions further change the local microenvironment. Cellular traction forces, generated by intracellular motor proteins (e.g. myosins), are transmitted locally at focal adhesion sites and thus cause local stiffening on the ECM [23]. As a direct result of structural disorder and slow network remodeling dynamics, the ECM can be considered to be in an out-of-equilibrium state. Similar to the CSK [24, 25], it is thus expected to display characteristic features of soft glassy materials (SGMs) [26, 27], such as foams [28], fractal colloidal gels [29], and concentration emulsions [30].
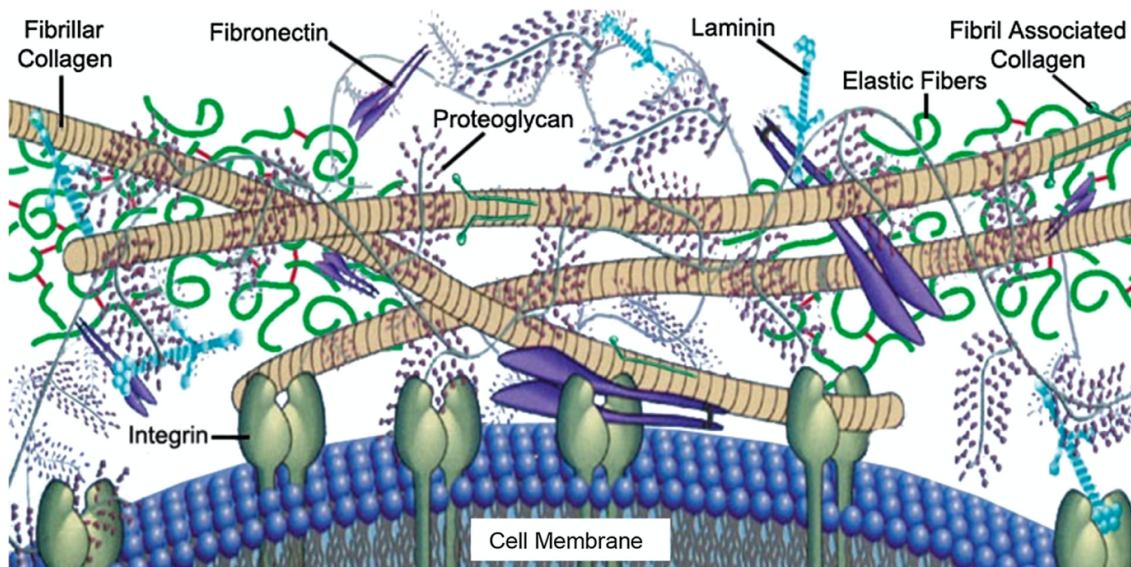
Figure 1. Representative scheme of the ECM. The cell is attached to the extracellular constituents through transmembrane proteins (integrins) that connect the CSK and the ECM. The collagen fibrous network represents the main structural scaffold of the ECM. Other ECM proteins (e.g. fibronectins, laminins, and elastins) have also their own structural, mechanical, and/or biochemical functions in the matrix. Proteoglycans fill the interatrial spaces within the hydrated network. Reprinted with permission from references [31, 32] Copyright © 2013, John & Wiley & Sons, Copyright © 2016, Elsevier.

The CSK and the ECM are viscoelastic, just as most other biological materials (**Figure 2-A**). They exhibit both viscous and elastic behavior and relax to load or deformation in a time-dependent manner. Viscous fluids show flow behavior and dissipate the energy from loading. In contrast, elastic solids store energy and recover their original shape once the load is removed. The viscoelasticity of the ECM and ECM-mimicking materials has a crucial effect on cellular behavior, including cell spreading, growth, proliferation, migration, differentiation and organoid formation [6]. Therefore, when developing novel biomaterials to mimic the ECM, viscoelasticity is a key design parameter.

Stress relaxation, one key feature of viscoelastic materials, has a strong influence on cellular behavior in the ECM [33]. When the external load or deformation is removed, the stress in the material decays in a time-dependent manner due to the viscous portion of the material. Most soft tissues, such as liver, breast, muscle, and skin, relax the applied stress over time scales from tens to hundreds of seconds (**Figure 2-B**) [6]. But also, hard skeletal tissues (e.g. bone, tendon, ligaments, and cartilage) exhibit viscoelastic behavior (**Figure 2-A**).
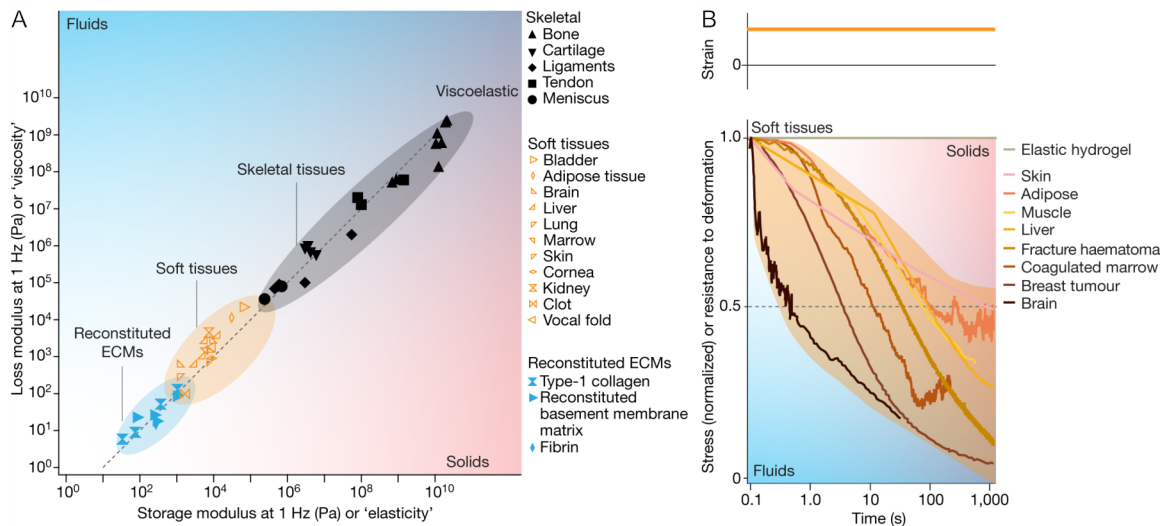
Figure 2. Viscoelastic behavior of biological tissues and extracellular matrices. A Plot of the viscoelastic moduli (i.e. loss and storage moduli) of hard and soft tissues as well as reconstituted ECMs, measured at a frequency of 1 Hz. **B** Stress relaxation of soft tissues in response to a step deformation. The measurements in **A** and **B** were performed with a range of instrumental strategies, such as shear rheology, nanoindentation and tensile tests. Tissues from different mammalian species were used, incl. human, rat, mouse, bovine, sheep, porcine, and canine tissues. Reprinted with permission from reference [6] Copyright © 2020, Springer Nature.

1.2   Biomimetic and bioinspired hydrogels

Hydrogels are physically and/or chemically crosslinked three-dimensional networks of hydrophilic polymers. The water-rich environment within the network and the mechanical properties of these soft materials are attractive for many biological applications, such as cell culture and tissue engineering. Protein-based biomolecular systems provide versatile and biocompatible design templates for the synthesis of biomimetic and bioinspired hydrogels. In protein-polymer networks, the synthetic polymeric backbone provides defined and also tunable properties while the protein-based building blocks introduce a variety of unique features, such as stimuli-responsiveness, self-healing and possibly higher-order self-assembly [16, 17].

In this chapter, I will give a brief background on hydrogels that are based on the concept of biomimicry and bioinspiration, specifically focusing on peptide-polymer hybrid hydrogels. In addition, I will introduce key chemical and physical properties of hydrogels, such as crosslink functionality and network architecture.

1.2.1 Advances in hydrogel technology

Hydrogels are formed from hydrophilic polymer chains via chemical or physical crosslinking. Due to the reticulate crosslinking structure, hydrogels are able to absorb a significant amount of water. They swell to an equilibrated structure while remaining an insoluble network. The first synthetic hydrogel, based upon polyhydroxyethylmethacrylate (PHEMA), was reported by Wichterle and Lim in 1960 [34]. In this work, hydrogels were defined as materials with high water content, inertness to biological processes, permeability for biomacromolecules (e.g. enzymes, metabolites) and sufficient mechanical strength to serve as a physical scaffold [34].

The absorption of water into the hydrophilic polymeric network is based on the balance between capillary forces, osmotic pressure, and hydration forces. Water uptake causes an expansion of the network [35] and swelling ratios (i.e. increase in hydrogel weight fraction due to solvent absorption) can exceed 5000 in superabsorbent hydrogels [36]. The water-rich environment within the porous network structure is key for mimicking the natural ECM and for the use of hydrogels in a variety of biomedical applications, such as cell culture, tissue engineering, controlled drug delivery, wound dressings, and biosensor development [37].

Hydrogels have been classified in many different ways, depending on their crosslinking mechanisms, source of raw materials as well as their physical and chemical properties [37]. As the basic construction of the network is accomplished via crosslinking of the individual chains, the crosslinking mechanism is frequently used to categorize hydrogels. In chemically crosslinked hydrogels, network formation is achieved via the introduction of chemical (i.e. covalent) bonds between individual chains. This can be achieved via specifically designed crosslinking molecules and/or during the polymerization process. In physically crosslinked (i.e. dynamic) hydrogels, gelation is based on physical interactions, such as chain entanglements, electrostatic interactions, hydrogen bonding, hydrophobic interaction, and chain crystallization [38]. Chemically crosslinked hydrogels generally have higher mechanical strength and degradation resistance while physical hydrogels show dynamic properties and higher sensitivity in response to environmental stimuli. Hybrid systems, combining chemical and physical crosslinks, find increasingly broad interest as they combine dynamic properties with excellent mechanical stability [39, 40].

Another classification of hydrogels is based on the origin of their molecular constituents. Natural hydrogels are usually derived from biological building blocks, such as proteins and polysaccharides. Proteins used for hydrogel preparation include the fibrous ECM proteins collagen, elastin and fibrin. Polysaccharide-based hydrogel building blocks are, for example, glycosaminoglycan and alginate. In addition, also decellularized ECM samples are used as a

natural hydrogel source. Natural hydrogels are inherently biocompatible and often contain bioactive functional units to promote cell activities [41]. At the same time, natural materials have a number of limitations. They lack tunability and, as a result of their inherent complexity and batch-to-batch variation, the physical and chemical properties are often not reproducible. Synthetic hydrogels conventionally refer to networks consisting of synthetic polymers, mainly derived from petroleum oil. Their physicochemical properties differ according to their chemical composition, structure, synthetic method (e.g. reaction conditions, crosslinking agents), and water content (i.e. swelling ratio). All these parameters can be adjusted to obtain desired properties for specific needs. In contrast to heterogeneous natural materials, synthetic polymers usually have a simple and repetitive structure. Their properties are thus more controllable and reproducible. Poly(acrylic acid), polyacrylamide, poly(N-isopropylacrylamide), poly(ethylene glycol) and poly(vinyl alcohol) are commonly used for the synthesis of polymeric hydrogels [42]. New trends in the area of polymeric hydrogels is the integration of biocompatible synthetic polymers with natural biomolecules, such as DNA/RNA, proteins/peptides, and polysaccharides [43, 44]. Using the ability of biomolecules to form supramolecular structures and to respond to a range of different stimuli provides additional design principles and functionality towards engineering 'smart' biomaterials [45].

With growing interest into smart materials, hydrogels that can change or adjust their properties in response to the external environment are a topic of intense research. Along these lines, many hydrogels have been developed where the sol-gel transition, swelling ratio, network structure or mechanical strength can be altered as a function of pH, temperature or ionic strength [46]. The resulting smart hydrogels find application in areas such as (i) pH and/or temperature triggered, controlled drug delivery [12, 47]; (ii) biomedical devices like shape memory bio-implants or smart valves [48, 49]; (iii) biosensors for the detection of specific biomolecules (e.g. glucose) [50]; (iv) tissue engineering and regenerative medicine, incl. growth factor delivery, stimuli-responsive cell adhesive surfaces and three-dimensional cell culture systems [51-54].

Despite strongly growing interest into hydrogels, developing applications is still a challenging task. One key reason is the current poor understanding of the network structure on mesoscopic scales, which would be required to devise design strategies for controlling and tuning physical and chemical network properties. This includes the mechanical hydrogel properties, which are often critical for the respective application. For example, the stiffness of hydrogels needs to be controlled for cell applications [55]. And also the viscoelasticity has been shown to be an important parameter [6]. Most conventional hydrogels have limited stiffness and low to intermediate stretchability [56]. Lately, soft stretchable hydrogels have been developed with application in load-bearing hydrogels [57], soft robotics [58], and

6

wearable devices [59]. However, due to their structural complexity and lack of control over the physical properties, these hydrogels have been developed for a specific application and general design principles are still lacking.

To overcome current hurdles, biomimetic and bioinspired hydrogels have been highlighted as an excellent design strategy, in particular considering the multiscale, hierarchical architecture found in natural materials. The molecular structures of biomolecules allow for the formation of self-organized structures, which are highly controlled across mesoscopic and macroscopic scales. Polysaccharide-based materials, consisting of glucosaminoglycans (e.g. hyaluronic acid), alginate, chitin and its derivatives (e.g. chitosan), have been broadly used in natural or hybrid hydrogels [60]. Also, nucleic acid-based materials have been developed, making use of the high specificity of base pairing and well-established synthetic methods [44]. Proteins based materials are outstandingly diverse and are formed from self-assembled globular or rod-like proteins. These include actin and tubulin or keratin and collagen, respectively. In the following sections, I will primarily focus on hydrogels made of natural protein building blocks and peptide-polymer hybrid materials that are inspired by natural protein building blocks.

1.2.2   Hydrogels inspired by self-assembling protein building blocks

For living organisms, proteins are essential biomacromolecules. Compared to synthetic polymers, they often have higher molecular weights and form complex three-dimensional structures. Proteins are produced at the ribosome where the genetic information is translated into a specific amino acid sequence. The amino acid sequence determines the three-dimensional structure as well as the ability to form higher-order assemblies. The thermodynamic, kinetic and mechanical stabilities of individual proteins and their assemblies are primarily based on non-covalent interactions, such as hydrogen bonds as well as ionic and hydrophobic interactions. Therefore, understanding sequence-structure-property relationships of proteins is key to utilizing proteins as material building blocks. A wide variety of natural proteins has been implemented into hydrogel systems to improve their functionality, often making use of the ability of these proteins to self-assemble into supramolecular structures (**Figure 3**) [61]. Instead of using natural proteins, their complex characteristics are often simplified and mimicked and a wide variety of synthetic biomimetic and bioinspired hydrogels has been developed.
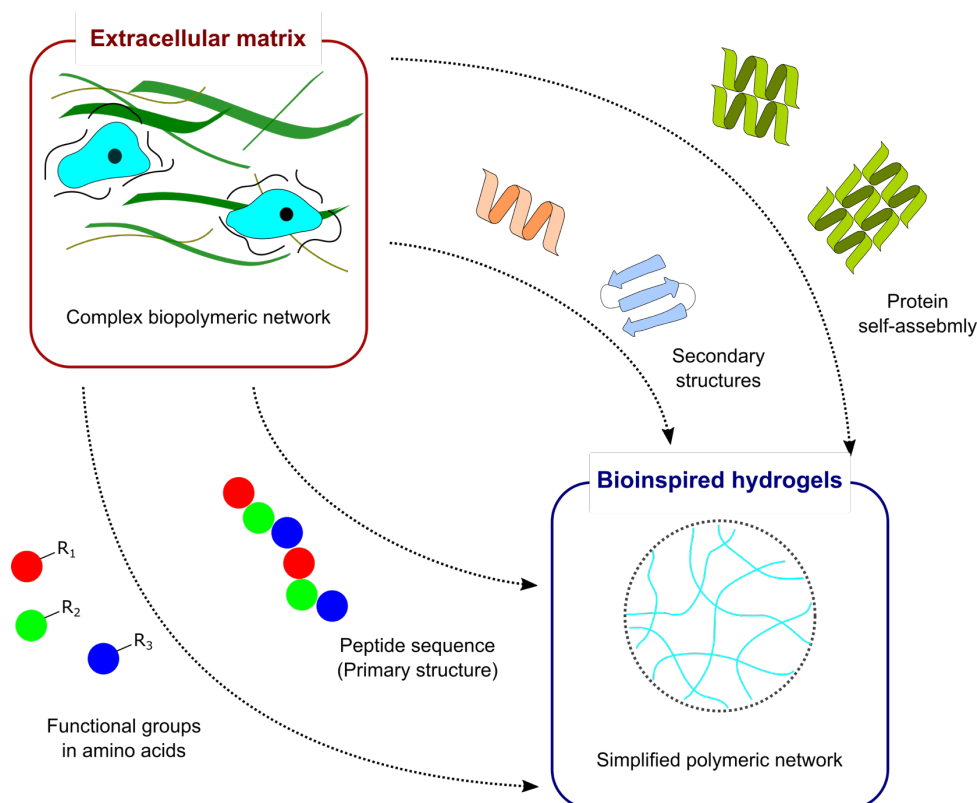
Figure 3. General strategy for designing biomimetic and bioinspired hydrogels. Adapted from reference [61]. Protein-based biomolecular system was represented as a model system which can be found in complex biopolymeric network (e.g. ECM). At the molecular level, biologically and/or chemically active functional groups on amino acids (i.e. monomer) can provide insights on the design strategy inspired by natural biological systems. The sequential connection of the monomers can form polypeptides, which drives folding into well-defined secondary structures of proteins (e.g. α-helix, β-sheet), and further into supramolecular structures through protein self-assembly. These fundamental understandings on the biological systems can be utilized as design parameters to develop novel bioinspired materials in cooperation with well-established and simplified polymeric platform.

Mimicking natural protein-based materials has been a topic of intense research [62-64]. In the case of proteins, the amino acid side chains are often the key functional unit responsible for protein association, self-assembly and function. To mimic specific properties, it can be sufficient to mimic the various chemistries of the side chains. An impressive example of this principle is based on the ability of histidine to coordinate metal ions. Histidine-metal coordination has been found in marine mussel proteins and spider fangs where it serves a stabilizing role and further allows energy dissipation and self-healing [65]. The latter originates from the reversibility of histidine-metal coordination and has inspired the design of a range of different physically crosslinked bioinspired hydrogels (**Figure 4-A**) [66, 67]. In addition to histidine, mussel byssus proteins also contain catechol groups, introduced via post-translational modification of tyrosine to yield 3,4-dihydroxyphenylalanine (DOPA) [68]. DOPA has also been used as a pH-sensitive dynamic crosslink via catechol-metal coordination [69] (**Figure 4-B**).
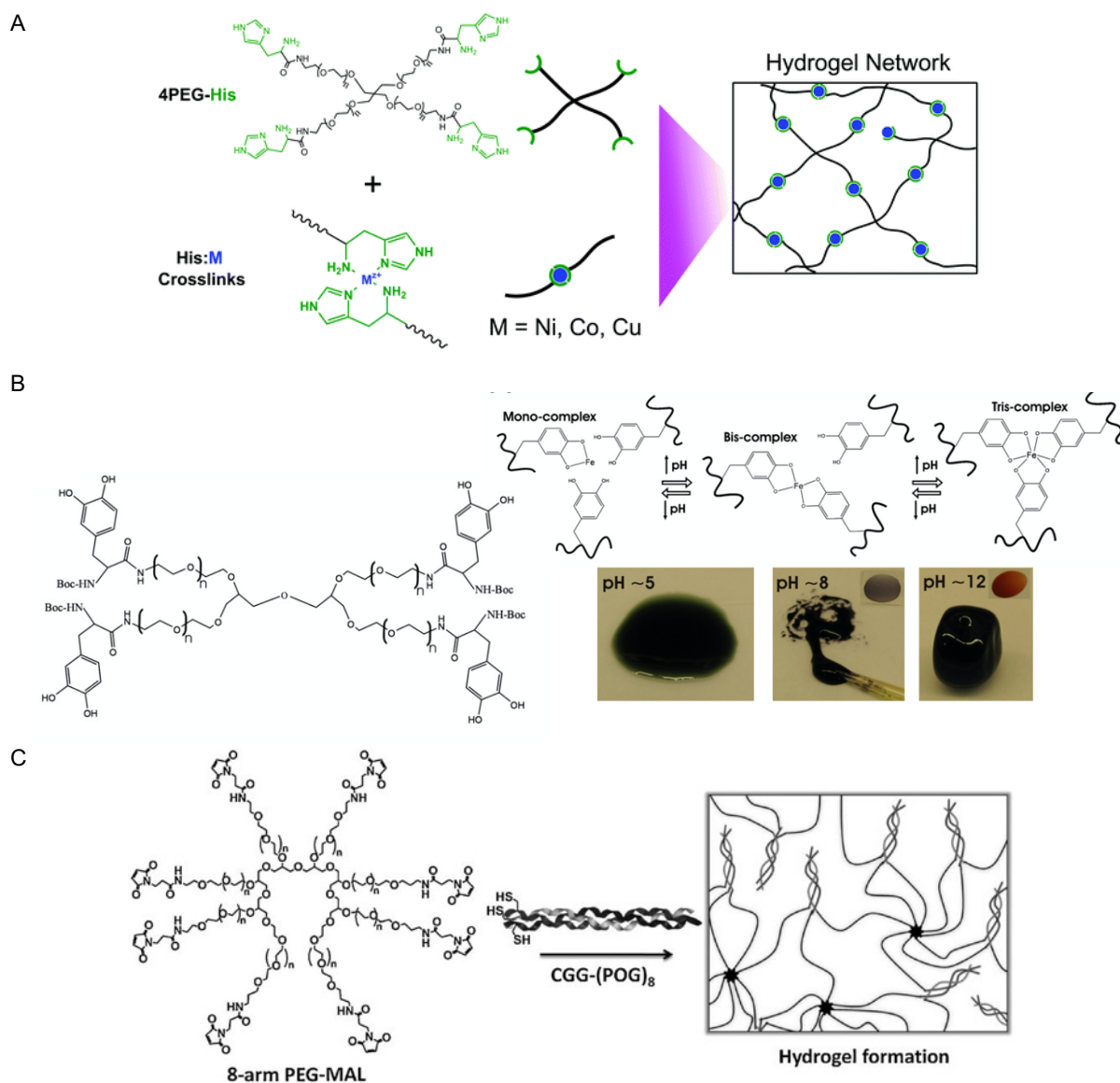
Figure 4. Representative hydrogel designs inspired by natural protein building blocks. A Physically crosslinked PEG-based hydrogel using histidine-metal coordination. Histidine-metal coordination strategy was inspired by mussel proteins. Addition of three different metal ions M^{2+} (M = Ni, Co, Cu) allowed the formation of metal coordination as physical crosslinks in the PEG network. Reprinted with permission from reference [66] Copyright © 2017 The Royal Society of Chemistry. **B** Mussel-inspired DOPA-Fe^{3+} crosslinked PEG hydrogels. Reprinted with permission from reference [69]. DOPA shows pH dependence, resulting in catechol-Fe^{3+} complexes of different stoichiometry. DOPA is again coupled to end-functionalized star-PEG as a physical crosslink. **C** PEG-based hydrogel physically crosslinked with collagen-mimetic peptides (CMPs). Reprinted with permission from reference [71] Copyright © 2011, WILEY-VCH Verlag GmbH & Co. The CMP, which forms a triple helical supramolecular self-assembly, was coupled to 8-arm PEG.

Instead of using individual amino acids or their functional groups, synthetic peptides that are able to fold into specific secondary structures (e.g. α-helix, β-sheet, polyproline II helices) are frequently employed. A typical example is the α-helical coiled coil (CC) association motif that occurs in intermediate filaments and myosin as well as several ECM proteins. CC-forming peptides exhibit self-assembly behavior, they thus form superhelical structures with different oligomerization states [70]. Similarly, synthetic CMPs fold into triple helical collagen-like

structures [71, 72] (**Figure 4-C**). As a result of their self-assembled nature, both CCs and CMPs are temperature-sensitive and can further be programmed to form sub to micrometer-size fibrous structures and hydrogels, similar to their natural counterparts.

1.2.3 Peptide-polymer hybrid hydrogels

The protein association motifs introduced above have frequently been used to physically crosslink synthetic polymers to obtain well-defined peptide-polymer hybrid hydrogels (**Figure 4-C**) [71, 73]. This is a direct result of their ability to self-assemble and self-heal. The natural protein sequence, e.g. from keratin or collagen, is reduced to the core association motif to obtain synthetic CC or CMP peptides with a typical length of 20-40 amino acids. On the polymer side, PEG and its derivatives have been widely used for the synthesis of hybrid hydrogels. The properties of PEG have been well characterized, which provides a clear advantage for application development [74]. PEG is a polymer with high hydrophilicity and biocompatibility as well as relatively low cytotoxicity [75, 76]. In contrast to other synthetic polymers (e.g. poly(lactic acid) and its copolymers [77]), PEG-based polymers usually show a low polydispersity. The synthetic procedure is well optimized so that molecular weight and polydispersity can be tightly controlled. Further, linear or branched architectures with different numbers of arms (e.g. 2, 4, 8 arms) are available [78].

Various chemistries can be utilized at the termini of linear or branched PEGs to couple protein association motifs (**Figure 5**) [79]. Among the well-established coupling reactions, the Michael addition between maleimide and thiol functional groups is commonly used. In addition, activated esters, such as the N-hydroxysuccinimide (NHS) ester, are available to couple molecules with amine groups. Both reactions display high coupling efficiencies in mild conditions (i.e. room temperature and neutral to mildly basic pH) and the required functional groups are easily introduced into peptides. The thiol group is available in the amino acid cysteine and amine groups are present at the N-terminus and in the side chain of lysine. Due to the growing need of peptide/protein-polymer conjugates for biomedical or pharmaceutical applications, also a wide range of alternative, bioorthogonal coupling methods has been developed over the last years, such as the azide-alkyne "click" reaction [80].
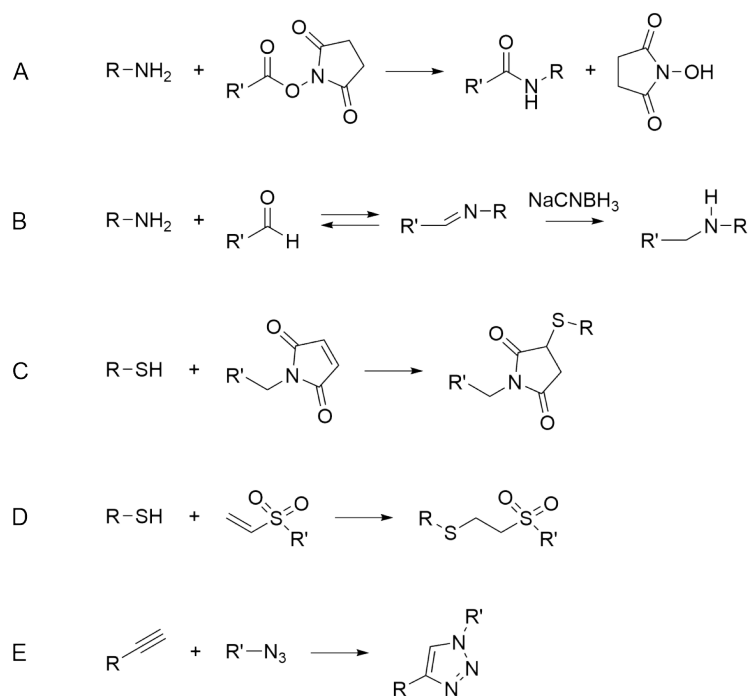
Figure 5. Representative coupling chemistries used for peptide-PEG conjugations. In all structures, R represents the peptide chain and R' denotes the PEG chain. **A** The reaction between an amine and the NHS ester produces an amide bond. **B** The reaction of an amine with an aldehyde forms a Schiff base. The Schiff base can subsequently be reduced to a secondary amine using a borohydride. **C** Michael addition between a thiol-containing peptide (e.g. cysteine) and a maleimide derivative. **D** The reaction between a thiol and a vinyl sulfone group produces a thioether bond. **E** The cycloaddition between an alkyne and an azide yields a triazole.

The majority of peptide-PEG hybrid hydrogels are based on star-PEGs, where the peptides physically crosslink the arms of the PEG. In this network design, the peptides serve as the only crosslinks and their properties directly determine the viscoelastic properties of the hydrogel. In addition, peptide-based physical crosslinks have also been inserted into otherwise covalently crosslinked networks where they introduce a viscoelastic component into an elastic material [81]. Self-assembled peptide association motifs (e.g. superhelices) exist in different oligomerization states. As a result, they intrinsically determine the crosslink functionality and thus also the network topology. For example, a dimeric peptide association motif connects two network chains at a crosslinking junction while a tetrameric crosslink connects (a maximum of) four network chains. At the same time, also the molecular geometry of the PEG molecules determines the network topology. For star-PEGs, the branching point confers another, covalent crosslinking junction. When comparing existing designs of peptide-PEG hybrid hydrogels, it becomes evident that different combinations of crosslink functionalities have been used for both the physical (self-assembling peptide) and covalent (star-PEG) crosslinks. In many studies, dimeric or trimeric peptides were combined with a 4-arm PEG backbone [70, 72]. Trimeric peptides were also coupled to linear-PEG (i.e. 2-arm PEG) [82] and even 8-arm star-PEGs were used [71]. Although a strong effect of the crosslink

functionalities of peptide and PEG on the bulk hydrogel properties can be expected, no systematic studies have been carried out so far. While PEGs with different crosslink functionalities are easily available, physical crosslinks with different functionality but otherwise similar properties are more difficult to obtain.

1.3 Molecular design strategies for dynamic crosslinks: collagen and coiled coils as key protein association motifs in the ECM

Inspired by natural protein building blocks, this work uses collagen triple helices (CTHs) and α-helical CC structural motifs for the synthesis of peptide-polymer hybrid hydrogels. Triple helical motifs are the fundamental element of the collagen structural hierarchy. The CMPs used here provide a trivalent crosslink with unique physical and chemical properties. Even though CMP-crosslinked hydrogels have been synthesized earlier [83, 84], it has not yet been investigated how the molecular crosslink properties (e.g. their thermodynamic and kinetic stability) determine the bulk material behavior. Once fundamental design principles are understood, CMPs with bioactive sequences can be utilized to develop a novel type of functional hydrogel, inspired by the ECM protein collagen. CC structural motifs offer another building block to serve as a dynamic crosslink in bioinspired hydrogels. CC structural motifs are highly interesting as their oligomerization state can easily be tuned via well-known changes in the amino acid sequence [85, 86]. This provides a possibility to investigate how the crosslink functionality affects the bulk viscoelastic behavior of the resulting hydrogels. Hydrogels crosslinked with trimeric CCs can further serve as an interesting reference system for the CMP-crosslinked hydrogels. In the following sections, I will introduce fundamental knowledge about CMPs and CCs relevant for this work. I will focus on their structures as well as thermodynamic and kinetic parameters that determine the crosslink properties in the network.

1.3.1 Collagen-mimetic peptides as trivalent crosslinks with slow kinetics

As a key ECM building blocks, collagen type I has a macroscale fibrous structure (diameter, d ~10 μm) that critically determines the overall structure as well as the mechanical properties of the ECM. Collagen fibers are composed of microfibrils (d ~100 nm) where collagen

molecules are arranged in a staggered manner, resulting in a distinctive D-periodic banding pattern [87]. The collagen molecule is a right-handed triple helix, consisting of three polyproline II (PPII) helices. These PPII helices self-assemble via supramolecular interactions (mainly hydrogen bonds). At a molecular level, the individual polypeptide chains are characterized by the repetitive sequence motif (X-Y-G). In principle, any amino acid can occur at the X and Y positions while glycine (Gly, G) is obligatory at every third position. Gly is buried at the center of the triple helical structure, forming an essential triple helix stabilizing hydrogen bond, whereas the X and Y residues are exposed toward the environment (**Figure 6**) [88]. While higher-order architectures of other collagen types can differ, the repeating sequence motif (X-Y-G) is shared in all fibrous regions. Frequently, the X and Y positions are occupied by the amino acids, proline (Pro, P) and hydroxyproline (Hyp, O), respectively. These amino acids confer structural stability to individual PPII helices as well as the supramolecular triple helical assembly [84].

CMPs have frequently been used for investigating the sequence-structure-function relationship of the collagen triple helix. Short-length polypeptides of the repeating (X-Y-G) sequence have been employed as synthetic collagen model systems among which $(PPG)_n$ and $(POG)_n$ are the most widely studied. For these model systems, their helical structure and thermal stability has been determined in a number of experiments [84, 89-93]. Because of their short length of ~20-40 amino acids, CMPs show re-association after thermal denaturation. This is not the case for full-length collagens, which form a gelatin hydrogel upon cooling. The small size of CMPs also allows their structural characterizations with X-ray crystallography and nuclear magnetic resonance (NMR) spectroscopy along with thermodynamic and kinetic analyses [84].
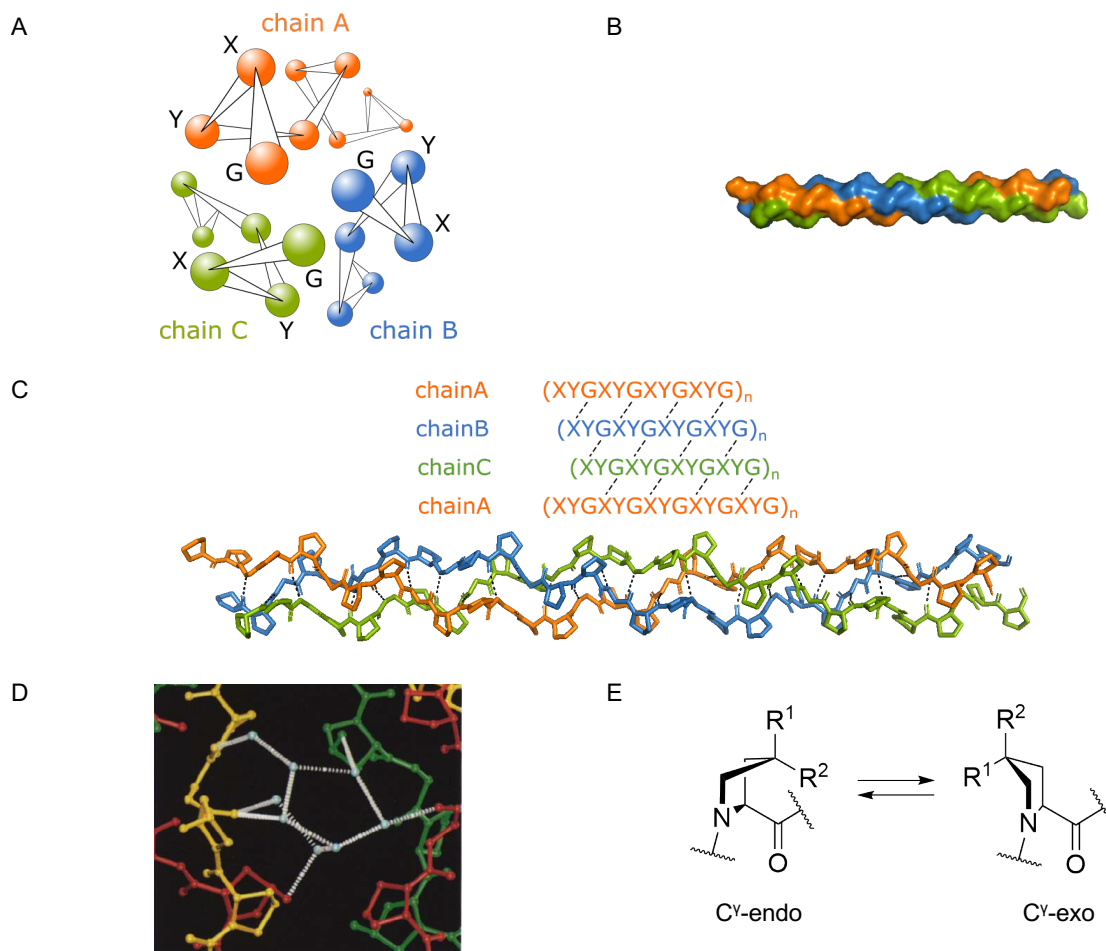
Figure 6. Structure of a collagen triple helix (CTH). A Schematic top view of the CTH. Glycine (G), located every third amino acid, is packed at the center of the helical structure and the X and Y amino acids are exposed toward the environment. The three individual chains are visualized with different colors. **B** Side view, showing the intertwined structure of the CTH. The CTH of $(PPG)_{10}$ peptide was used as an example (PDB ID: 1K6F) [94]. For visualization, the three identical chains are shown with different colors. The figure was produced with PyMOL Molecular Graphics System (version 2.5.1 Schrödinger,LLC.) **C** Intermolecular hydrogen bonding of the CTH. One-residue staggering of the individual chains facilitates the bonding pattern of G→X (black dotted lines). With the CTH of $(PPG)_{10}$ peptide, the intermolecular hydrogen bonds were visualized using PyMOL. **D** Surface hydration network, involving carbonyl groups on peptide backbones and hydroxly groups at Hyp residues. Reprinted with permission from reference [95] Copyright © 1995 Elsevier. X-ray structures show that carbonyl groups from the peptide backbone can form water bridges with hydroxly groups at Hyp residues, staggered by one amino acid. **E** Ring conformations of Hyp, displaying C^{γ}-endo and C^{γ}-exo ring puckering. If Hyp is located in the Y position, the exo puckering induces preorganization of the chains via stereoelectronic effects, enhancing the association rate and stability of the triple helical structure.

The thermodynamic stability of CMPs is increased by the presence of the post-translationally modified amino acid Hyp [92, 96]. X-ray crystallography of CMPs provided key information about the triple helical structure and yielded first insights into the role of Hyp in thermodynamically stabilizing the CMP structure. Hyp provides an anchoring point for water molecules that form the hydration network around the CMPs (**Figure 6-D**) [95]. It was initially discussed that differences in the hydration network around Pro and Hyp may contribute to CMP stability; however, altered stereoelectronic effects and/or intrinsic imino acid propensities within the Pro ring provided an alternative explanation. It has been proposed that the hydroxyl

group of Hyp determines the preferred ring structure, causing C^γ-exo ring puckering of 4R-Hyp in the Y position (**Figure 6-E**) [92]. This hypothesis is based on the inductive effect of the hydroxyl group in 4R-Hyp, which favors C^γ-exo ring puckering in the Y position. In contrast, 4S-Hyp favors C^γ-endo ring puckering in the same position, causing a destabilization effect [97]. However, in the X position, the conformational isomers of Hyp have the opposite effect [91]. Ultimately, the specific conformational preference (ring puckering) of Hyp in the Y position leads to a preorganization of the PPII helices and enhanced conformational stability in CMPs with the sequence $(POG)_n$. Preorganization reduces the entropic cost of the association process and thus increases the association rate of $(POG)_n$ [92, 97]. In addition to the role of imino acids (e.g. Pro and its derivatives), also other specific amino acids affect triple-helix stability and PPII propensity, which has been studied with host-guest peptide models [98-100]. In the Y position, the most stable amino acid is arginine or Hyp, followed by methionine. In the X position, the most favorable amino acid is Pro, followed by charged amino acids [97].

In addition to the CMP structure and thermodynamic properties, also the kinetics of CMP association has been investigated with the goal of understand the role of Hyp. The association of fibrous proteins like collagen is complicated due to their multimeric nature. In contrast to globular proteins, which possess fast dissociation and re-association kinetics, the association of long and linear superhelical motifs is much slower [101, 102]. *In vitro*, the association kinetics of collagen is extremely slow and hardly reaches equilibrium. Similarly, slow kinetics have also been observed for CMPs. After a temperature jump, a new thermal equilibrium was only reached after 10 to 15 h [103]. Considering that three chains need to come together (trimeric nucleation), the local concentration of CMPs is key to determine the association kinetics [93]. For high local concentrations, when trimeric nucleation is fast enough, *cis-trans* isomerization of the Pro ring becomes the rate-limiting step. However, if the concentration of free monomers is low, self-association of the triple helix is mainly dominated by the kinetics of trimeric nucleation (**Figure 7**) [103]. When nucleation is the rate-limiting step, the apparent nucleation rate (k_a) varies depending on the CMP sequence. For example, it was reported that the nucleation rate is ~1000 times faster for $(POG)_{10}$ than for $(PPG)_{10}$. This can be considered to be a direct effect of the enhanced conformational stability conferred by Hyp [93].

$$\begin{array}{c} \text{C} \\ + \\ \text{2C} \underset{k_2}{\overset{k_1}{\rightleftharpoons}} \text{D*} \xrightarrow{k_3} \text{H*} \xrightarrow{k_4} \text{H} \end{array}$$
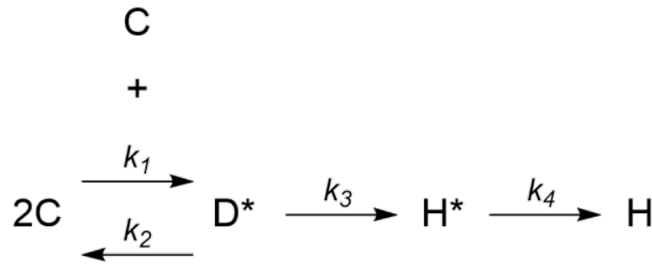
Figure 7. Association mechanism of CMPs. C represents a single peptide chain CMP (monomer). Two monomers form a dimeric nucleus (D*) with the association rate (k_1). The unstable dimeric intermediate can dissociate with the dissociate rate (k_2). Upon binding a third monomer, the dimeric nucleus grows into a trimeric nucleus (H*) with the rate k_3. From H*, the helix propagates with the rate k_4 to form the collagen triple helix (H). The apparent nucleation rate (k_a) is defined as $k_a = (k_1/k_2)*k_3$. The propagation rate (k_4) is determined by *cis-trans* isomerization of the Pro rings.

CMPs are versatile building blocks for biomimetic and bioinspired materials as both the sequence (e.g. Pro vs. Hyp) and length of the peptides are tunable. Both parameters in combination determine the thermodynamic and kinetic properties of the CMPs and are thus expected to affect the bulk mechanical properties of the resulting bio-inspired hydrogels. In this work, the CMPs will be combined with 4-arm star-PEG and serve as self-assembling physical crosslinks. Specifically, it will be investigated how the thermal stabilities and the expected slow association/dissociation kinetics of different CMPs determine the viscoelastic properties of the resulting hydrogels.

1.3.2   Coiled coil structural motifs as multivalent dynamic crosslinks

Coiled coils (CCs) are supercoiled helical bundles of two or more α-helical peptides. In the early 1950s, their α-helical structure was first revealed by Crick [104] and Pauling [105] when performing X-ray diffraction studies on α-keratin. Since this early work, it has been established that CCs are highly abundant in natural proteins [106] and the typical CC structure was defined as a protein structural motif [107]. Nature uses the CC motif in many different hierarchically built structures. For example, the CC motif of α-keratin serves as a building block for hairs, scales, feathers, threads, and egg capsules, which all exhibit excellent mechanical properties [108, 109].

CCs are frequently found as structural and mechanical building blocks in intracellular compartments (e.g. as part of CSK fibers and molecular motor proteins) as well as in extracellular structures (e.g. in cartilage, blood clots and the basal lamina). CC-containing proteins further serve important roles in cell signaling [110], transcription, gene regulation,

cellular transport [111], force sensing [112] and chromosome segregation [113, 114]. In a mechanical context, CC motifs are often found in load-bearing structures where they preserve mechanical integrity or facilitate structural transitions. CC function critically depends on the specific amino acid sequence and length, their oligomerization state and the force loading geometry [106].

In the CSK, CC motifs are found in fibrous proteins as well as short leucine zippers [115]. The CSK is an entangled and dynamically crosslinked meshwork, primarily composed of actin filaments, microtubules and intermediate filaments. The intermediate filament proteins keratin or vimentin [116, 117] mainly consist of CC motifs. Furthermore, the molecular motor proteins myosin, kinesin and dynein, are also composed of CC motifs [118, 119]. While most CSK structures assemble from dimeric CC motifs, CCs in the ECM are more variable. Laminins, which are network-forming fibrous ECM proteins, contain a heterotrimeric CC motif [120]. Also, matrilins [121] and thrombospondins (TSP1 and TSP2) [122] consist of a trimeric CC structure. Tenascins form a hexameric state, based on a trimeric CC motif involved in oligomerization [123]. CC-containing ECM proteins have a variety of roles in biological processes and their oligomerization state provides multivalency and, as a result, higher binding affinity to other ECM proteins [122]. In general, trimeric CCs are also expected to be mechanically more stable (i.e. tougher and stronger) than dimeric CCs [106].

CC motifs are broadly used in bioengineering as hydrogel building blocks, as they can easily be prepared synthetically, using solid-phase peptide synthesis. The CC sequence is composed of repetitions of seven amino acids with residues usually denoted as (*abcdefg*). In this so-called CC heptad, the sequence consists of hydrophobic (H) and polar (P) amino acid residues arranged in the pattern of HPPHPPP. To form a stable CC, usually 3 or more contiguous repeats are required [124, 125]. While the stability of the individual helices is supported by hydrogen bonds along the axis of the helix (**Figure 8**) [126], the driving force behind the formation of the superhelical structures is the hydrophobic interaction at the tightly packed core (*a* and *d* positions). Furthermore, the presence of charged residues at the *e* and *g* positions allows for more stable superhelical structures due to the contribution of ionic interactions (**Figure 8**) [127]. Homo- and heterotypic assemblies with parallel, antiparallel or mixed topologies can be formed [115, 128]. The helical stability is also influenced by the solvent exposed amino acids in the *b*, *c*, and *f* positions, depending on their respective helix propensities [129].

Synthetic CC peptides have been introduced into biomimetic and bioinspired hydrogels as physical crosslinks. Self-assembling CC peptides allow fast and highly specific crosslinking [130]. They further provide the hydrogel with the ability to self-heal once crosslinks are

dissociated by mechanical deformations [70, 131], change in pH or temperature [132, 133] as well as chemical denaturants [134]. CCs can thus introduce stimuli-responsiveness into physically crosslinked hydrogels. Dimeric CCs have predominantly been used for this purpose as they provide a well-defined divalent crosslinking stoichiometry. Considering the tunability of CC oligomerization states, CCs are an interesting system to investigate the role of crosslink functionality (see section 1.2.3) on the viscoelastic characteristics of the resulting hydrogels. This work utilizes structurally closely related dimeric, trimeric and tetrameric CC crosslinks to test how the interplay of the thermodynamic CC stability and crosslink functionality affect the linear viscoelastic range, stress relaxation and crosslink rupture in CC-crosslinked star-PEG hydrogels.
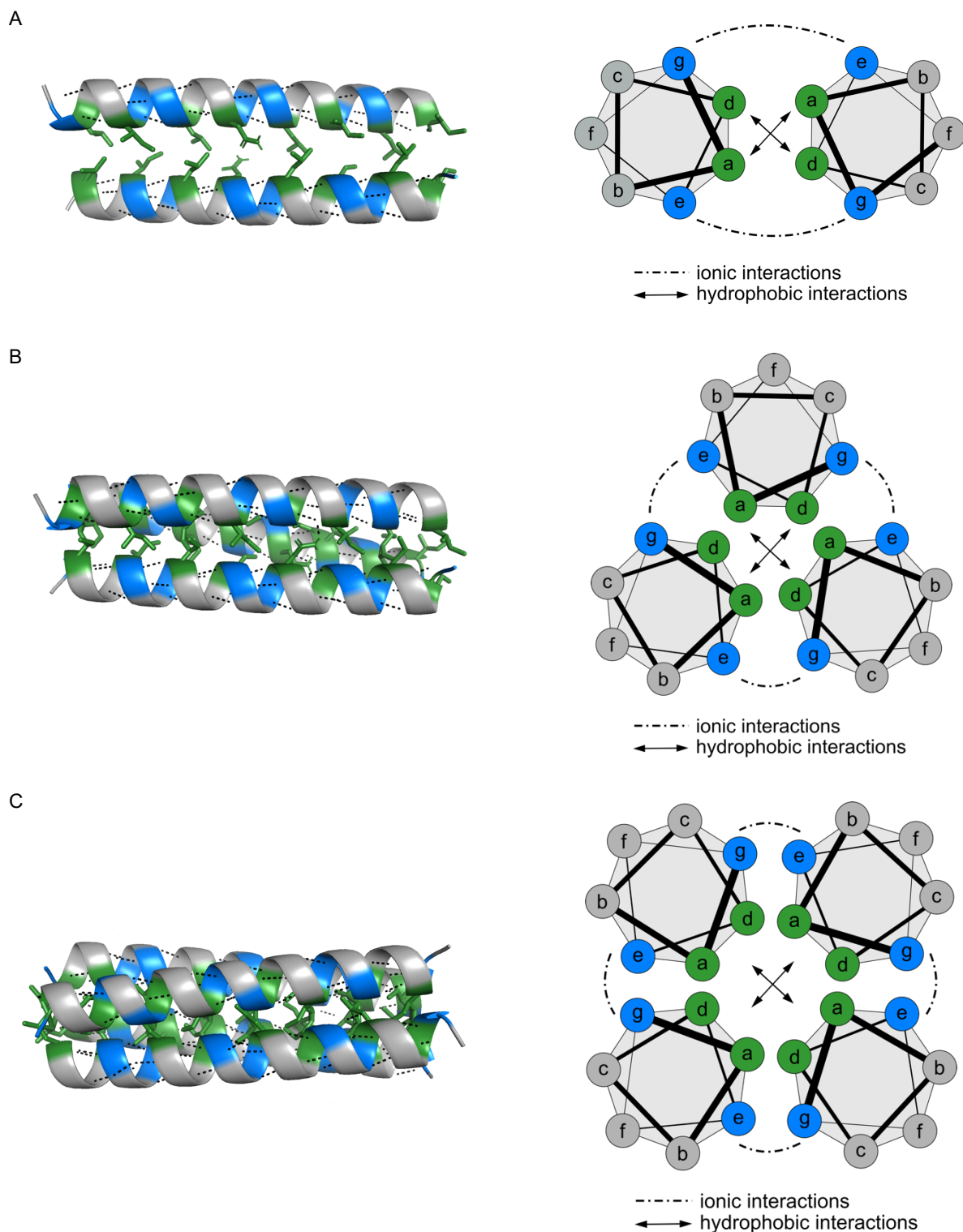
Figure 8. Structures of three different CC oligomerization states. Homodimeric (**A**), homotrimeric (**B**), and homotetrameric (**C**) CCs in side view (left) and helical wheel representation (right). Amino acids at the hydrophobic core (*a* and *d* positions) were highlighted with green and charged residues (*e* and *g* positions) are colored in blue. In the side view, intramolecular hydrogen bonds along the individual α-helices are indicated as black dotted lines. Black dash-dotted lines indicate ionic interactions between charged residues and black double arrows represent hydrophobic interactions. Models were predicted using CC-Builder 2.0 [135] and the CC structures (in side view) were produced with PyMOL Molecular Graphics System, Version 2.5.1 Schrödinger, LLC.

19

1.4   Self-reporting CMPs based on fluorescence self-quenching

Conventional shear rheology is a robust method to investigate bulk material properties of hydrogels. Its main limitation is that it does not reveal the molecular picture, particularly under large mechanical deformations. Information about crosslink rupture and possible re-association can only be inferred indirectly from the stress-relaxation experiment. Under load or deformation, physically crosslinked hydrogels exhibit a mechanical response and reach material failure when the load or deformation is large enough to break the crosslinks. Therefore, understanding the kinetics of crosslink dissociation and re-association events at the molecular level is critical to understand and control mechanical failure and recovery.

Fluorescence labeling strategies can provide an elegant solution for visualizing the association state of self-assembling molecular building blocks, such as CMPs and CCs. In a hydrogel network, fluorescently labeled crosslinks can become self-reporting molecular sensors that report on the number of formed crosslinks, both globally and locally [136-139]. Importantly, they further provide a real-time optical readout to monitor the rupture of the crosslinks upon deformation. FRET and fluorescence self-quenching (FSQ) have been broadly employed as a self-reporting strategy in the fields of mechanobiology and mechanochemistry and are also suitable for monitoring crosslink association and dissociation [140-143].

FRET is a non-radiative energy transfer process that is mediated by long-range dipole-dipole interactions between the donor and acceptor fluorophores. It is necessary that the donor and the acceptors fluorophores are positioned in close proximity (typically 10-100 Å) as well as in a favorable orientation [144]. Compared to FRET, which is usually realized with two different fluorophores with overlapping excitation and emission spectra, the FSQ strategy needs only one type of fluorophore. This significantly simplifies the labeling and measurement procedures. Importantly, it is technically much easier to implement FSQ for homoligomeric crosslinks. FSQ assays are based on the close proximity between two or more identical fluorophores that quench each other as a result of intermolecular interactions [145]. Increasing the distance between the dye molecules through dissociation reduces fluorophore interactions and decreases FSQ. As a result, the original fluorescence intensity (i.e. monomer state of the fluorophore without quenching) is recovered. The fluorescence intensity thus increases several-fold compared to the quenched state in the assembled structure [145, 146].
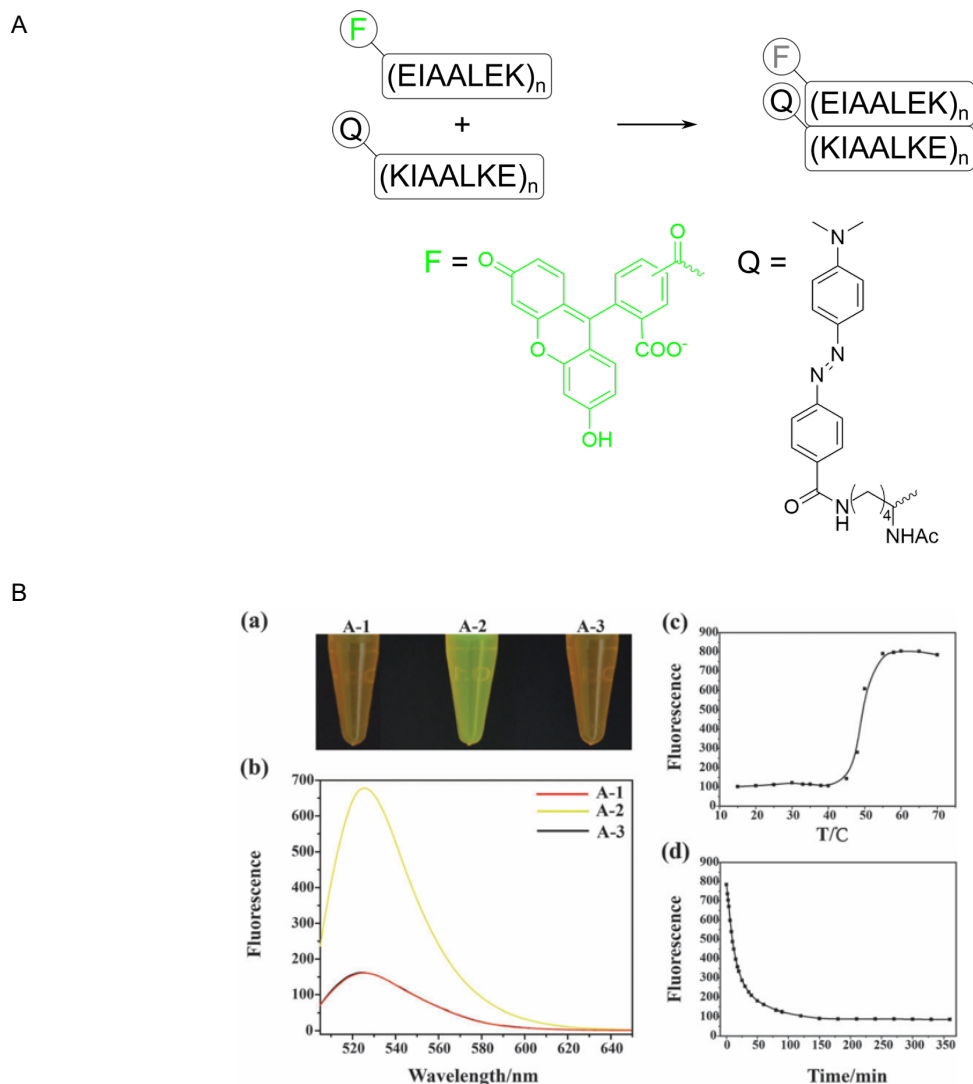
Figure 9. Fluorescence self-reporter systems to monitor the assembled states of CC peptides (A) and CMPs (B). A Upon the association of the CC superhelices, the fluorescence of 5(6)-carboxyfluorescein (CF, F) can be reduced by the proximity of the dabcyl-based fluorescence quencher (Q) This FRET-based strategy is usually employed for heterodimeric CC systems where one chain is labeled with a donor fluorophore and the other is coupled with an emitting or non-emitting acceptor fluorophore (FRET acceptor or quencher). **B** CF-G(PRGPOG)$_5$ as a representative of CF-labeled CMPs, showed FSQ while they form the triple helical state. Reprinted with permission from reference [146] Copyright © 2016, Royal Society of Chemistry. At temperatures above T_m, i.e. CMPs are in the predominantly monomeric state, high fluorescence intensity was observed with an absorption maximum at 497 nm and emission maximum at 524 nm. At temperatures below T_m, the CF molecules were in the close proximity due to the formation of the CTH while FSQ caused a significant decrease in the fluorescence intensity.

Recently, fluorescence techniques have been introduced for investigating the structure of collagen. Early studies focused on the intrinsic fluorescence of collagen fibers in tissues [148, 149]. More recently, CMPs equipped with a FSQ reporter system have been introduced for diagnostic, prognostic and therapeutic applications with the goal of probing and visualizing damaged (or denatured) collagen triple helical fragments in collagen-related diseases [150-153]. The FSQ strategy has further been used to assess the helical composition of CMPs at

the nanomolar concentration (**Figure 9-B**) [146] and for visualizing the self-assembly of CMP-based nanofibers [154]. For the synthesis of FSQ-labeled CMPs, CF was frequently used. The excitation maximum of CF is located at 490 nm and its emission has a maximum at 515 nm. CF carries a free carboxyl group that allows for coupling with the free amine group at the N-terminus of peptides [155]. In this work, CF-labeled CMPs will be synthesized. The goal is to first test if the FSQ strategy can be used for measuring the kinetics of chain association and dissociation. If possible, it will be interesting to further investigate the application potential of the labeled CMPs for observing crosslink formation, rupture and re-association in a CMP-crosslinked hydrogel.

2   Aims of this thesis

From a structural and mechanical points of view, ECMs are intricate protein-based networks containing a range of different macromolecules. The CTHs as well as CCs are representative protein association motifs that are abundantly found in ECM proteins. Both of the motifs are crucial in defining the structure and mechanics of ECMs. The ability of the CTH and CC structures to self-assemble has been utilized for the synthesis of various dynamically crosslinked biohybrid hydrogels [70-72, 131, 156-161]. The further development of such hydrogels towards applications is currently limited as only few studies attempted to link their viscoelastic properties to the molecular properties of the peptides used as the dynamic crosslinks in the networks. Towards this aim, I utilized a range of molecularly controlled peptide building blocks to crosslink the well-defined polymer PEG. Specifically, the thermodynamic and kinetic properties of the crosslinks, as well as their functionality, was systematically designed to elucidate how these microscopic molecular parameters are closely related to the viscoelastic properties of the macroscopic material. Specifically, I utilized CMPs with different thermodynamic and kinetic properties and α-helical CCs with controlled oligomerization state in order to provide answers to three questions below:

1) How do the thermodynamic and kinetic properties of CMP-based crosslinks affect the viscoelastic properties of the collagen-inspired hydrogels?

Based on existing knowledge about CMPs, peptide length and sequence are ideal design parameters to tune the molecular properties of CMP-based dynamic crosslinks. For the three CMP sequences $(POG)_7$, $(POG)_{10}$, and $(PPG)_{10}$ the following thermodynamic and kinetic properties were already known before I started this work. The thermodynamic stability, i.e. the melting temperature T_m, of $(POG)_7$ is close to $(PPG)_{10}$ (T_m ~30 ˚C) while $(POG)_{10}$ shows a significantly higher melting temperature (T_m ~ 60°C). It had further been shown that $(POG)_n$ peptides possess faster association rates (k_{on}) than $(PPG)_n$ peptides, based on the preferred conformation of the Pro rings in the respective structures. With the goal of understanding collagen association, CMP association had already been studied in great detail; however, little information was available about the kinetics of CMP dissociation. The first goal of this work was thus to determine the dissociation rates (k_{off}) for the chosen CMPs, following temperature-jump induced dissociation via CD spectroscopy (**Chapter 4.2.1**)

Provided that T_m, k_{on} and k_{off} are known for all CMPs, these parameters can subsequently be related to the bulk viscoelastic properties of the resulting hydrogels. For example, $(POG)_7$ and $(POG)_{10}$ are expected to show a similar association rate while T_m is remarkably different. If the resulting hydrogels display distinctive viscoelastic properties, k_{on} can be excluded as the determining factor. Knowledge of the previously measured (T_m and k_{on}) and newly established (k_{off}) molecular properties of the CMPs is thus considered to provide insight into the importance of the respective parameters on the stress relaxation behavior of CMP-crosslinked polymeric networks based on 4-arm PEG. In particular, it was planned to elucidate if and how the relaxation time is determined by the thermodynamic and/or the kinetic crosslink properties (**Chapter 4.2.2 and 4.2.3**). An alternative way to control the kinetic crosslink properties of CMP crosslinks is to change the temperature where the viscoelastic hydrogel properties are measured. With this strategy, k_{on} and k_{off} can be altered for one and the same hydrogel without changing the CMP crosslink. Measurements at different temperatures thus ideally complement and validate the experiments performed with peptides of different length and sequence (**Chapter 4.2.4**).

Another important crosslink feature that is considered to be relevant for the viscoelastic properties of dynamically crosslinked hydrogels is the network connectivity. As the crosslink functionality of CMPs is restricted by the trimeric nature of collagen, another ECM-inspired peptide building block was used that provided crosslinks with different oligomerization states. CC protein structural motifs can be designed to assemble into dimers, trimers and tetramers and are thus an ideal model system to answer the following question:

2) How does crosslink functionality affect the material properties of CC-inspired hydrogels?

The oligomerization state of CCs is easily tuned and depends on the specific side chains of the amino acids packed into the hydrophobic core of the superhelix, i.e. at the *a* and *d* positions in the (*abcdefg*)$_n$ heptad repeat. Recently, Woolfson et al. have introduced a set of homodimeric, homotrimeric, and homotetrameric CCs [85]. These are based on the same original sequence and only the *a* and *d* positions were modified to obtain the desired oligomerization state. Even though the thermodynamic stabilities T_m of these CCs vary from 56 to higher than 90 ˚C [85], they represent one of the most promising currently available model systems to serve as divalent, trivalent, and

tetravalent crosslinks in a hydrogel network. I thus utilized these CCs to investigate if and how crosslink functionality affects a range of hydrogel properties, again using star-PEG as the to-be-crosslinked polymer (**Chapter 4.3.2**).

The crosslink functionality, as an important means to control network connectivity, has not yet been systematically investigated, partly because of the lack of suitable crosslinks with tunable oligomerization state. Using the proposed combination of CCs and PEG, allows for tuning both the functionality of the dynamic CC crosslinks and of the PEG itself. Using 4-arm star-PEG vs. linear PEG (i.e. 2-arm) can be considered as another covalent crosslink junction located at the "molecular center" of the respective PEG backbone. The aim of this work is thus to investigate if and how the combination of dynamic and covalent crosslink functionalities affects the linear viscoelastic range and the overall stiffness of the resulting hydrogels as well as their stress relaxation properties and dynamic rupture (**Chapter 4.3.3**).

While controlling the molecular properties of CMP and CC crosslinks is a powerful means to investigate correlations between microscopic and macroscopic network properties, real-time information about the network response to deformation is lacking. To fill this gap, a fluorescence self-reporting system was tested for its potential to serve as a mechanosensitive molecular probe that provides information on the status of individual crosslinks upon rupture and self-healing.

3) Can fluorescently labeled CMPs or CCs be designed to serve as molecular probes to monitor crosslink assembly state in the network?

Self-reporting peptide systems based on FSQ are promising for visualizing the status of individual crosslinks. The aim of this chapter was to investigate the possibility of designing a fluorescence self-reporting system that distinguishes between associated CMPs (i.e. formed crosslinks) and free peptides. Such a reporter system cannot only provide information on the number of crosslinks formed. It can further be employed as a real-time mechanosensitive probe that specifically reports on crosslink rupture and self-healing during and after mechanical deformation. Earlier work has shown that CMPs N-terminally labeled with the widely used organic fluorophore CF show FSQ due to the close proximity of three fluorophores at the N-terminus. In this work, CF-labeled CMPs were synthesized and their suitability for the intended application was tested. Particularly, the intensity ratio between the associated and quenched structure and the

free peptide was measured (**Chapter 4.4.1**). In addition, dissociation was monitored in a competitive assay with unlabeled CMPs, following the change in fluorescence intensity at room temperature. The latter can be considered equivalent to measuring the internal dynamics of crosslink exchange in a network crosslinked with labeled and unlabeled CMPs (**Chapter 4.4.2**). For the future, this work may provide design principles for the introduction of fluorescence reporter systems into ECM-inspired peptides. Such systems have the potential to serve as mechanosensitive probes for monitoring crosslink rupture or reformation in hydrogel networks in real-time

Overall, in this dissertation my aim was to investigate how molecular crosslink parameters determine the bulk viscoelastic properties of ECM-inspired hydrogels. CMPs and CCs served as tunable physical and dynamic crosslinks in peptide-polymer hybrid networks. For the CMP-crosslinked networks, the molecular aspects focused on the thermodynamic and kinetic properties of the crosslinks and their effect on stress relaxation. For the CC-crosslinked networks, the focus was on crosslink functionality, making use of CCs with different oligomerization states. Towards the design of self-reporting peptide crosslinks, I tested a promising approach based on FSQ. It is intended that this reporter system will allow for studying crosslinking rupture and reformation during mechanical deformation. In combination, this work promotes the development of novel hydrogels that mimic and are inspired by biological systems, with tunable and self-reporting properties that my find use in biomedical and soft material-based applications.

3 Materials and methods

In this chapter, the experimental procedures are described in detail, including all information about the peptides, buffers, and chemicals used for each experiment.

3.1 Chemicals and buffers

All salts used for buffer preparation were purchased from Carl Roth (Karlsruhe, Germany). Unless stated otherwise, the other chemicals were obtained from Sigma Aldrich (Taufkirchen, Germany). The buffer solutions were prepared using ultrapure water (Integra UV plus Reinstwassersystem, Siemens aquaris SG water, Hamburg, Germany). Borate buffer (pH 8.9), coupling buffer (pH 7.2) or phosphate buffered saline (PBS, pH 7.4) were used depending on the peptide and intended experiment. For hydrogel preparation, borate buffer was used for the conjugation of the CMP N-terminus to star-PEG functionalized with NHS-esters. In contrast, coupling buffer was used for the CC-crosslinked hydrogels, where cysteine-containing peptides were coupled to the maleimide-terminated star-PEG. The respective buffer was also used for the corresponding CD experiments, performed with CTH- or CC-forming peptides. Lastly, PBS and borate buffer were used for the characterization of FSQ-labeled CMPs. The detailed composition of the buffers and their use for the different experiments is also summarized in **Table 1**. For all CD measurements, the buffers were filtered, using a syringe filter with 0.2 µm pore size (VWR international, Darmstadt, Germany).

Table 1. Composition of the buffers used. All the buffers used in different experiments were prepared with ultrapure water and their pH values were adjusted at room temperature. Ethylenediaminetetraacetic acid (EDTA) was used in coupling buffer.

Name	Composition		pH	Measurement
Borate buffer	50 mM	$H_3BO_3/Na_2B_4O_7$	8.9	CD spectroscopy Rheology Fluorescence measurements
Coupling buffer	50 mM 50 mM 10 mM	Na_2HPO_4 NaCl EDTA	7.2	CD spectroscopy Rheology
PBS	10 mM 2 mM 137 mM 2.7 mM	Na_2HPO_4 KH_2PO_4 NaCl KCl	7.4	CD spectroscopy Fluorescence measurements

3.2 Peptides

Collagen mimetic peptides

The CMPs H-(PPG)$_{10}$-OH and H-(POG)$_{10}$-OH were purchased from PeptaNova (Sandhausen, Germany). The peptide H-(POG)$_7$-OH was synthesized by Caslo (Lyngby, Denmark). The purity of all peptides was >90 %.

Coiled coil peptides

All CC peptides were synthesized chemically using semi-automated solid phase peptide synthesis (SPPS). Crude peptides were purified with high-performance liquid chromatography (HPLC). The detailed methods are given below.

Fluorescence-labeled collagen mimetic peptides

5(6)-carboxyfluorescein-labeled CMPs, used for the fluorescence experiments, were synthesized using SPPS and manual coupling for the fluorophore. First, the H-(PPG)$_{10}$-NH$_2$ and H-(POG)$_7$-NH$_2$ peptides were synthesized. Subsequently, CF was coupled to the N-

terminus using manual coupling. Crude peptides were purified with HPLC. Again, the detailed methods are given below.

3.2.1 Solid-phase peptide synthesis (SPPS)

Theoretical background

Since Emil Fischer successfully performed the first coupling between two amino acids in 1903, the further development of peptide synthesis has been a main focus of organic chemistry [162]. In 1963, a breakthrough pioneered by R. B. Merrifield allowed peptide synthesis on a solid-phase (resin) [163]. The growing peptide chain was immobilized on the resin, which enabled the controlled, step-wise addition of amino acids (**Figure 10**). This strategy has allowed for performing the reaction with higher completion and degree of polymerization. During each coupling step, the immobilized peptide chain is connected to the new amino acid via peptide bond formation, which involves an activator and a base. This requires that the N-terminus of the newly added amino acid carries a temporary protecting group so that it cannot participate in the coupling reaction. Usually, also the side chain functional groups are protected to prevent undesired side-reactions. To obtain high yields, an excess of amino acid is usually employed in each reaction step.

In the early implementation of SPPS by Merrifield, polystyrene-based resins were used. Nowadays, these have been replaced with crosslinked poly(dimethylacrylamide) resins [164] as well as polystyrene-based resins [165] that were copolymerized or grafted with hydrophilic chains (e.g. PEG). Merrifield also employed temporary protection strategies for the N-terminus of growing peptides, based on tert-butyloxycarbonyl (Boc)-based chemistry, combined with benzyl (Bzl)-type protecting groups for semi-permanent side chain protection [166]. The Boc group is acid labile and can be removed with trifluoroacetic acid (TFA); however, the Bzl-type protecting groups need to be cleaved using extremely strong acids, such as hydrofluoric acid (HF). Due to the toxicity and the requirement of special equipment for reactions with HF, Boc/Bzl chemistry has now been replaced with fluorenylmethoxycarbonyl (Fmoc)/tert-butyl protecting groups [167]. For the deprotection of the temporal Fmoc group, mild basic conditions can be utilized, e.g. piperidine. The tert-butyl-type protecting groups at the amino acid side chains are removed with TFA.
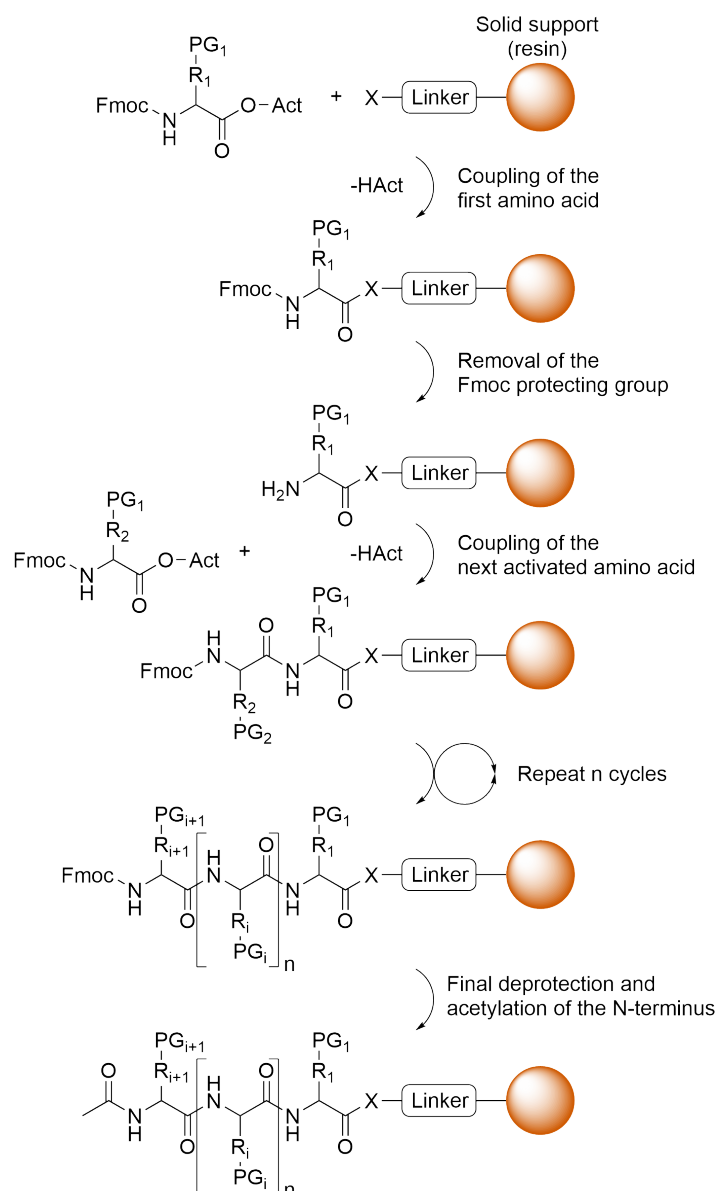
Figure 10. General scheme of the standard procedure employed for solid-phase peptide synthesis. The anchoring molecule (i.e. linker) functionalized on the surface of the solid support (i.e. resin) is coupled with the first amino acid. The amino acid is already protected with Fmoc as a temporary protecting group (Fmoc) for its amine group at the N-terminus as well as contains a semi-permanent protecting group (PG_i) on its side chain. For higher coupling efficiency, the C-terminus of the amino acids is activated with an activator (ester form, -Act). It promotes the formation of an ester or amide bond between the C-terminus of the amino acid and the functional group (X = -OH or $-NH_2$ form) of the linker. An activator molecule is released during the coupling reaction (HAct). The Fmoc protecting group at the N-terminus is removed with piperidine to enable the next coupling step exposing a free amine group at the growing chain on the resin. This coupling process is repeated n times until the desired peptide sequence is obtained. Before the final cleavage, the free N-terminus of the crude peptide can be capped with an acetyl group if necessary. TFA and/or a TFA-based cocktail is employed to cleave the linkage between the crude peptide and the resin. During this final cleavage, the semi-permanent side chain protecting groups are also removed.

A variety of chemistries are commercially available to couple the first amino acid to the resin. Esterification of the amino acid carboxyl group with a hydroxyl group or amidation with an amine group are generally used for the first coupling reaction. To improve the coupling efficiency, activated amino acids are introduced with 2-10 times excess compared to the resin

functionality [168]. Coupling reagents such as 2-(6-chlor-1*H*-benxotriazol-1-yl)-1,1,3,3-tetramethylaminium-hexafluor-phosphate (HCTU) or (7-Azabenzotriazol-1-yloxy)-trispyrrolidinophosphonium hexafluoro-phosphate (PyAOP) are broadly utilized. For in situ coupling, an organic base such as N,N-diisopropylethylamine (DIPEA) is used to form the carboxylate of the amino acids [169]. At the end of the coupling cycle, designed as necessary, the formed crude peptide can be optionally acetylated for deactivation of the N-terminal amine group. TFA-based cocktail solution (TFA:triisoproylsilane (TIPS):water = 95:2.5:2.5 %) for cysteine free peptides or a TFA solution including ethanedithiol (EDT) (TFA:TIPS:EDT:water = 92.5:2.5:2.5:2.5 %) for the peptides containing cysteine is used for the final cleavage of the all semi-permanent protecting groups of the amino acid residues as well as for releasing the synthesized peptides from the linker on the resin.

Experimental procedure

SPPS was performed using a Tribute® UV synthesizer (Gyros Protein Technologies Inc., Tucson, AZ, USA). H-rink amide ChemMatrix ® resin (Sigma Aldrich, Taufkirchen, Germany) was used on a 100 µmol scale. Amino acids and HCTU (Merck, Darmstadt, Germany) were used with 5x excess and DIPEA with 2.5x excess compared to the resin loading. For each coupling cycle, the coupling time was 30 min for the CMPs and 20 min for the CC peptides. Synthesis was performed at room temperature (RT). The C-terminus of all peptides was amidated after being released from the resin after the final cleavage with TFA:TIPS:EDT:water = 92.5:2.5:2.5:2.5 % for 2 h at RT. For the CC peptides, the N-terminus was acetylated, using a solution of acetic anhydride:pyridine:DMF (ratio = 1:1:3). The crude product was precipitated with ice-cold diethyl ether. The white precipitate was centrifuged at 4,700 x g for 15 min at 4 °C and the supernatant was discarded. The precipitation and washing steps were repeated three times and the final white pellet was dried under N_2 flow. The crude peptides were dissolved in 50 % acetonitrile (ACN)/water solution and lyophilized for storage at -20 °C.

For the fluorescence experiments, 5(6)-carboxyfluorescein was further coupled to the free amine at the N-terminus of the CMPs while the peptides were still coupled to the resin. The CF and PyAOP were dissolved in DMF with 5x excess and with 2x excess compared to the resin capacity, respectively. The peptide loaded on the resin was mixed with the CF/PyAOP/DMF solution and DIPEA was added with 20x excess dropwise into the mixture. The mixture was incubated for 24h, while the tube was rotated RT in the dark. The mixture was centrifuged at 4,700 x g for 30 min at RT and the supernatant was discarded. The CF-CMPs loaded on the resin were washed with DMF until the unreacted CF molecules were removed. The resin was mixed with piperidine:DMF = 20:80 % and incubated for 30 min at RT

on a rotary shaker for deprotection. The mixture was centrifuged again and washed with DMF and DCM several times and dried under N_2 flow. The CF-labeled CMPs were cleaved from the resin with TFA:TIPS:EDT:water = 92.5:2.5:2.5:2.5 % for 2 h at RT. The crude product was precipitated with ice-cold diethyl ether. The precipitate was centrifuged at 4,700 x g for 15 min at 4 °C and the supernatant was discarded. The precipitation and washing steps were repeated three times and the final pellet was dried under N_2 flow. The crude peptides were dissolved in 50 % acetonitrile (ACN)/water solution and lyophilized for storage at -20 °C.

3.2.2   Peptide purification with high-performance liquid chromatography

Theoretical background

HPLC has been developed as a powerful method for the purification of peptides from reaction byproducts and incomplete sequences. It is based on the distinctive interaction strengths of the sample species between a mobile and a stationary phase. In general, hydrophobicity (or hydrophilicity) and the overall net charge of the peptide determine the interaction with the stationary phase (column). The solvent (i.e. mobile phase) is another important factor for the separation process. In particular, longer peptides (more than 20-30 residues) may form secondary structure (e.g. α-helix, β-sheet) that affects the properties of the peptide to be purified [170].

Depending on these features, three major modes of HPLC have been traditionally employed. Size-exclusion chromatography (SEC) separates peptides according to their hydrodynamic radius (R_h), i.e. peptides of different size have different retention times on the column. In contrast, ion-exchange and reverse-phase (RP) chromatography make use of the net charge and hydrophobicity, respectively. Ion-exchange chromatography is thus extremely useful for basic (i.e. net positive charge) or acidic (i.e. net negative charge) peptides that interact with an oppositely charged surface on the stationary support. RP-HPLC is the most widely used mode for peptide purification due to its fast speed and high efficiency [170]. It can be seen as the opposite of normal-phase (NP) chromatography. For NP-HPLC the stationary phase is polar, and an initial gradient of mobile phase starts from a dominantly nonpolar composition. In contrast, RP-HPLC literally means the opposite approach where a nonpolar stationary phase is combined with a polar starting gradient. For RP-HPLC, silica-based supports are coated with hydrophobic octyl (C_8) or octadecyl (C_{18}) molecules. The peptides are eluted in the order of increasing overall hydrophobicity. For the mobile phase, aqueous TFA/ACN mixtures are used. This brings the advantage of an acidic volatile solvent system that enables

easy solvent removal when the purified peptides are freeze-dried after HPLC purification. RP-HPLC is sometimes used after an ion-exchange column as a multistep protocol for better separation performance.

Experimental procedure

The crude peptides, stored at -20 °C, were dissolved in ACN/water solution (20:80 %) and loaded onto the RP-HPLC (LC-20A Prominence, Shimadzu, Duisburg, Germany), equipped with a preparative C_{18}-column (Macherery Nagel, Düren, Germany). The mobile phase was prepared using water and ACN both with 0.1 % TFA. A linear gradient from 20 % to 80 % of ACN in water was used over 30 min and the flow rate was maintained constant at 25 mlmin^{-1}. During peptide elution, UV absorbance was monitored to detect a peptide bond at 220 nm and the peptides were collected accordingly. The final fractions were lyophilized and stored at -20 °C, after determining their molar mass with mass spectrometry. Detailed information on the preparative HPLC chromatograms of all peptides synthesized and purified is available in the appendix (**Figure S1, Figure S2**).

3.2.3   Mass spectrometry with the matrix-assisted laser desorption/ionization-time-of-flight (MALDI-TOF) method

Theoretical background

Matrix-assisted laser desorption/ionization (MALDI) is an ionization technique that uses an intense laser pulse for a short duration. It is frequently used for biopolymers, such as DNA, proteins and carbohydrates, as it allows for the ionization of these molecules in their intact form (i.e. low fragmentation). Generally, ionization is hard to be accomplished because of the high molecular weight and net charge (or high polarity) of biomolecules. These extremely non-volatile samples are mixed with a suitable matrix material, such as 2,5-dihydroxybenzoic acid (DHB), and placed on a special metallic plate in order for them to dry out and form crystals. Then a pulsed laser irradiates the sample, triggering desorption of the sample and matrix material. During this process, the matrix absorbs the energy of the laser and transmits it to the sample so that isolated and ionized molecules are transferred into the gas phase [171, 172]. Finally, the ionized molecules are accelerated into the mass spectrometer (MS) to analyze their exact molecular weights.

Time-of-flight (TOF) is the most widely used detection method, particularly in a combination with the MALDI ionization technique, mainly due to its large mass detection range [173]. It uses the kinetic energy distribution of the ionized molecules, described as m/z. After ionization, all ionized molecules are accelerated at the same initial position and velocity. But the time each ion takes to reach the detector at a fixed distance (time-of-flight) varies according to the ratio of their mass (m) and charge (q) (m/z) [173]. For single-charged ions, the lightest ions reach the detector first with a shorter time-of-flight than heavier ions. These arrival times can thus be displayed as the resulting mass spectrum.

Experimental procedure

The accurate molar mass and purity of the synthesized peptides were confirmed using MALDI-TOF (Autoflex Speed, Bruker, Berlin, Germany), using DHB as the matrix. The mass spectra of the purest fractions of the synthesized peptides are shown in the appendix (**Figure S1, Figure S2**). The detection mode and detector mass range were RP 700-5000 Da or LP 1000-4500 Da and the laser intensity varied from 50 to 80 %.

3.3 Biophysical characterization

3.3.1 Thermodynamic properties of the CMPs and CC-peptides based on circular dichroism (CD) spectroscopy

Theoretical Background

CD spectroscopy is a powerful method to investigate biological macromolecules [174]. Particularly, the secondary structure of peptides or proteins can be identified from their CD spectra [175]. Circular dichroism is defined as the differential absorption of circularly polarized light, rotating counterclockwise (i.e. left-handed, L) and clockwise (i.e. right-handed, R). Circular dichroism is a characteristic property of optically active (i.e. chiral) molecules. The circularly polarized light is generated using a modulation method, which is splitting linearly polarized light into the L and R circularly polarized components of the same magnitude under an alternating electric field [176] (**Figure 11-A, I**). Optically active molecules exhibit differential absorption of left-handed and right-handed circularly polarized light, resulting in a reduced

magnitude for one component compared to the other. Therefore, the resultant wave becomes elliptically polarized (**Figure 11-A, II**). CD spectrometers measure either the difference in absorbance between L and R components ($\Delta A = A_L - A_R$) or more commonly the degree of ellipticity (θ), defined as an angle whose tangent is the ratio between the minor and major axes of the resulting ellipse. The two values can be converted, using the following relationship between ΔA and θ in molar ellipticity [deg cm^2 dmol^{-1}], namely $\theta = 3{,}298\Delta A$ [177].
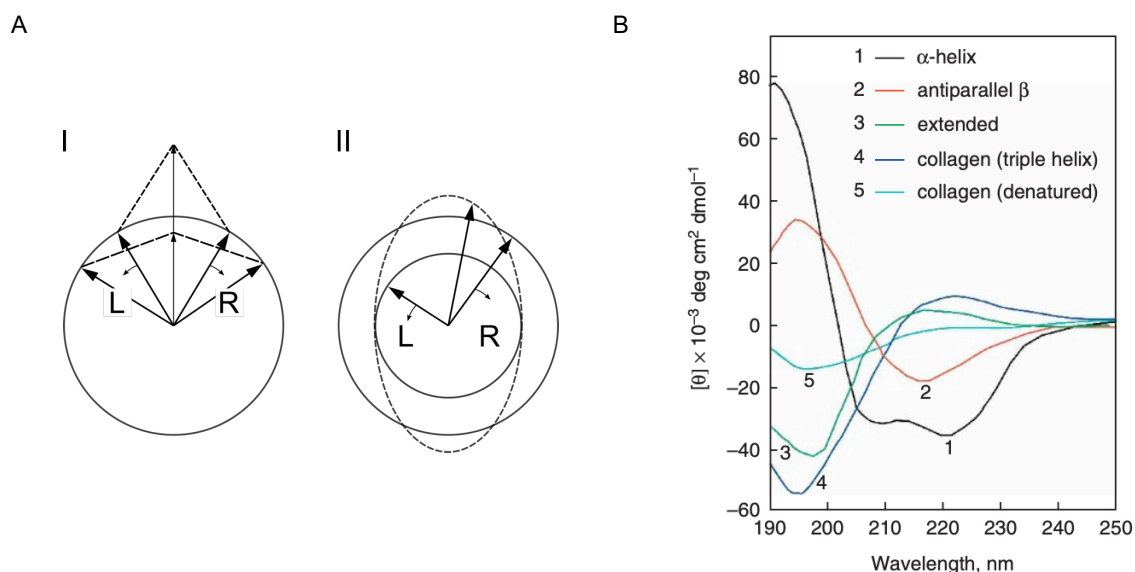
Figure 11. Circular dichroism (CD) spectroscopy for structural characterization of proteins. A The CD effect has its origin in the left (L) and right (R) circularly polarized components of plane polarized radiation [176]. When the amplitudes of the two L and R circularly polarized components are the same, the result is plane polarized light (solid line) (**I**). An optically active sample may show a larger absorption of one type of circularly polarized light compared to the other, thereby changing the ratio of the two components. The resultant is elliptically polarized radiation (dashed line) (**II**). A CD spectrometer measures the difference in absorbance between the L and R circularly polarized components in terms of the ellipticity (θ) in degrees. **B** Characteristic CD spectra of some representative secondary structures of polypeptides. For example, CD spectra of poly-L-lysine forming an α-helix (1 black), an antiparallel β-sheet (2 red) at pH 11.1 and a random coil (3 green) at pH 5.7. Further, placental collagen is shown in its native triple helical state (4 blue) and in the denatured state (5 cyan). Reprinted with permission from reference [177] Copyright © 2006, Springer Nature.

CD spectra of the peptides provide information about their secondary structure, i.e. the presence of α-helices, β-sheets, and collagen triple helices (**Figure 11-B**). Each secondary structure shows differential absorption at specific wavelengths and the position of minima and/or maxima in the respective spectra are characteristic for different peptide conformations. CD spectroscopy can further be used for thermodynamic or kinetic measurements where changes in the ellipticity at specific wavelengths are monitored as a function of temperature [177, 178]. For β-sheet conformations, a characteristic minimum at 218 nm is usually observed while α-helices possess two distinctive minima at 208 nm and 222 nm. Particularly the ratio between the two minima ($[\theta]_{222}/[\theta]_{208}$) can be an indication for the formation of α-helical coiled

coils when the ratio is close to or higher than 1 [179]. For collagens, a low maximum around 223-225 nm is generally used for identifying the distinctive collagen triple helical structure, combined with a deep minimum below the 200 nm region. However, the exact position of the maxima and minima vary for different CMPs and the structural origin of these peak shifts is still poorly understood.

Changes in ellipticity at a specific wavelength can be used for investigating the thermodynamic stability of a peptide (or a protein). Assuming a two-state model, the melting temperature (T_m) [177] can be obtained as well as Gibbs free energy (ΔG), enthalpy (ΔH) and entropy (ΔS) for peptide folding (association) and unfolding (dissociation):

$$nU \rightleftharpoons F_n$$
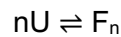
where F is the folded state, U is unfolded state, and n is the number of individual chains forming the folded state.

For peptides composed of identical subunits (e.g., homodimer, homotrimer, homotetramer), the equilibrium constant of folding (K_F) at a given temperature, T, is defined:

$$K_F = \frac{[F]}{[U]^n} \tag{1}$$

where [F] and [U] are the concentrations of folded and unfolded species at a given condition, respectively, and n refers to the number of the peptide chains forming the folded state.

From the equilibrium constant, the free energy of the folded structure (ΔG_F) is obtained:

$$\Delta G_F = -RT \ln K_F \tag{2}$$

where R is the gas constant (8.3145 J mol^{-1} K^{-1}) T is the absolute temperature (Kelvin, K) and K is the equilibrium constant of the association reaction, defined from **Equation 1**.

The fraction folded (f) is simply obtained from the concentrations of folded/unfolded states or the measured ellipticity under any condition i.

$$f = \frac{n[F]}{n[F] + [U]} = \frac{[\theta_i] - [\theta_U]}{[\theta_F] - [\theta_U]} \tag{3}$$

where θ_i is the observed ellipticity at any condition i and θ_F and θ_U are the ellipticities of the fully folded and fully unfolded states, respectively. Using the fraction folded, the temperature at which f = 0.5 (i.e., the midpoint of the denaturation curve) is referred to the melting temperature.

Equation 3 can be rearranged after insertion of **Equations 1 and Equation 2**:

$$\theta_i \;=\; \frac{([\theta_F] \;-\; [\theta_U])}{(1 + e^{(\Delta G/RT)})} \;+\; \theta_U \tag{4}$$

The free energy can be obtained from the Gibbs-Helmholtz equation to describe the folding event as a function of temperature:

$$\Delta G \;=\; \Delta H \left(1 - \frac{T}{T_m} \right) \;-\; \Delta C_p \left((T_m \;-\; T) \;+\; T ln \left(\frac{T}{T_m} \right) \right) \tag{5}$$

where ΔC_p is the change in heat capacity of the folding-unfolding transition. In practice, ΔC_p is negligible because the change in enthalpy (ΔH) is much bigger than ΔC_p [177].

At last, the **Equation 4** can be rewritten with insertion of **Equation 5**:

$$\theta_i \;=\; \frac{([\theta_F] \;-\; [\theta_U])}{\left(1 + e^{\left((\frac{\Delta H}{R})(\frac{1}{T} - \frac{1}{T_m}) \right)} \right)} \;+\; \theta_U \tag{6}$$

The four quantities ΔH, T_m, θ_F and θ_U from **Equation 6** are the fitted parameters when using the commercial analysis program (Global 3, Applied Photophysics, Leatherhead, UK), which includes pre- and post-baseline corrections. Alternatively, a manual calculation can be performed, where the fraction folded is obtained from the linear regressions of the baselines. Also, the first derivative of the sinusoidal thermal denaturation curve can be used. The temperature where the peak of the first derivative has a maximum corresponds to T_m and the width of the peak determines ΔH.

Experimental procedure

For the CD measurements, all CMP solutions were prepared with PBS or borate buffer with a concentration of 1.0 g mL^{-1}. The solutions were stored at 4 °C at least 48 h before the measurement to form a stable triple helical structure.

All the CC-peptides were dissolved in PBS or coupling buffer with a concentration of 50 μM. To reduce possible disulfide bonds between the thiol groups of the terminal cysteine residues, a concentration of 500 μM of tris(2-carboxyethyl)phosphine (TCEP) was additionally added. The measurement was performed only after the solutions have been incubated for over 48 h at 4 °C.

Thermal unfolding experiments were performed to determine the melting temperatures (T_m) of the CMPs and CC-peptides. A Chirascan qCD spectrometer (Applied Photophysics, Leatherhead, UK) was used to obtain the CD spectra of the CMPs and CC-peptides over a

temperature range from 4-90 ˚C. A quartz cuvette with 1 mm path length was used for the measurements (Hellma Analytics, Müllheim, Germany).

During the measurement, the temperature was increased in steps of 1 ˚C at a rate of 0.1 ˚C per minute for the CMPs and at a rate of 1 ˚C per minute for the CC peptides. Spectra were obtained across a range of wavelengths 200-250 nm and the integration time was 0.7 s. The peptide spectra were obtained by subtracting the background spectra measured for the respective buffer solutions.

The molar ellipticity (ME), θ_{ME} [deg cm^2 dmol^{-1}] was calculated according to **Equation 7**:

$$\theta_{ME} = \frac{100\ \theta_\lambda}{m\ d} \tag{7}$$

where θ_λ is the observed ellipticity [degree] at wavelength λ, m is molar concentration of the peptide [dmol^{-1}], and d is the path in the cuvette [cm].

To extract the T_m values, the spectra were globally fitted using Global 3 analysis software (Applied Photophysics, Leatherhead, UK). The obtained results were compared to the T_m values calculated via the first derivative of the thermal transition curves of the ellipticity at a characteristic wavelength: θ_{225nm} for collagen and of θ_{222nm} for α-helical CCs. The transition curves were further used to calculate the fraction folded (f_{TD} from thermal denaturaion). The temperature where f_{TD} = 0.5 also represents T_m. To obtain f_{TD}, the calculated ellipticity for fully associated, θ_F from pre-transition baseline and that for fully unfolded, θ_U from post-transition baseline were used in **Equation 8**.

$$f_{TD} = \frac{(\theta_i - \theta_U)}{(\theta_F - \theta_U)} \tag{8}$$

3.3.2 Kinetics of CMP association/dissociation based on temperature-jump experiments

Theoretical background

Circular dichroism is also a powerful method for investigating the kinetics of peptide/protein association and dissociation [178]. When the kinetics is slower than the time resolution of the measurement (e.g. association of collagen in vitro [103]), CD spectroscopy provides information about the change in the secondary structure over time.

Considering the two-state model described in **Equation 1**, the rate of folding (association) and unfolding (dissociation) at a given temperature can be expressed:

$$rate\ of\ folding, r_f = k_f[U]^n \tag{9}$$

$$rate\ of\ unfolding, r_u = k_u[F] \tag{10}$$

where k_f and k_u are the rate constants of folding and unfolding, respectively. When folding and unfolding are at equilibrium, the two rate constants are equal and the relationship between the equilibrium constant and the rates constants can be derived from the **Equation 1**:

$$K_F = \frac{k_f}{k_u} \tag{11}$$

To measure the rates of folding or unfolding, the equilibrium needs to be disturbed. This can for example, be achieved via a temperature jump. For example, for the thermally driven folding of a protein, the sample is first equilibrated at a high temperature where the protein is fully unfolded and then rapidly plunged into a cell holder in the CD spectrometer that is pre-equilibrated at a lower temperature where the protein is fully folded. During the folding process, the protein shows changes in ellipticity at a characteristic wavelength that can be used for the calculation of the rate constant. The number of the subunits (n) in the associated structure and the mechanism of folding determine the reaction order. If the reaction order is known, the rate constants can be calculated using the equations in **Table 2**.

Unfolding kinetics can be measured with basically the same method. But the temperature jump is performed from a temperature where the protein is fully associated to a higher temperature at which the protein unfolds. From **Equation 10**, the first order unfolding rate can be obtained when the initial change in ellipticity is linear after temperature jump. A linear slope in the log or natural log of fraction folded versus time can be used for fitting the first-order rate constants [178].

Table 2. Orders of reaction and rate equations for protein folding events using CD spectroscopy. In the respective equations, [U] is the concentration of the unfolded protein at any time t and $[U]_0$ is the concentration when the protein is fully unfolded. [U] can be calculated from the fraction folded, f with the relationship of $[U]_0(1-f)$, where f is $([\theta_t - \theta_U]/ [\theta_F - \theta_U])$. $[\theta_t]$ is the ellipticity at any time t, $[\theta_F]$ is the ellipticity of the fully folded state and $[\theta_U]$ is the ellipticity of the fully unfolded state. k is the rate constant of folding [178].

Reaction order	Rate equation	Integrated rate equation	Linear plot	Slope	Units of rate constant
0	$- \delta[U] / \delta t = k$	$[U] = [U]_0 - kt$	$[U]$ vs t	$-k$	$mol\ L^{-1}\ s^{-1}$
1st	$- \delta[U] / \delta t = k\,[U]$	$[U] = [U]_0\, e^{-kt}$	$\ln[U]$ vs t	$-k$	s^{-1}
2nd	$- \delta[U] / \delta t = k\,[U]^2$	$1/[U] = 1/[U]_0 + kt$	$1/[U]$ vs t	k	$L\ mol^{-1}\ s^{-1}$
3rd	$- \delta[U] / \delta t = k\,[U]^3$	$1/[U]^2 = 1/[U]_0^2 = 2kt$	$1/[U]^2$ vs t	$2k$	$L^2\ mol^{-2}\ s^{-1}$

Experimental procedure

To quantify the kinetics of unfolding, the CMPs were subjected to a temperature jump and the molecular response was monitored with CD spectroscopy. The CMPs were kept in an ice-water bath prior to the temperature jump. The samples were prepared as described above for the equilibrium unfolding experiments. To start the measurement, the ice-cold CMP solution was transferred to the cuvette, pre-equilibrated at the desired temperature in the cuvette holder. The pre-set temperatures were chosen such that they were within a range of temperatures close to the T_m of the CMPs, but never reached the T_m or exceeded it. This was necessary as the rate of unfolding was too slow to be reliably measured at temperatures more than 2-5 °C below T_m. Specifically, the temperatures were set in the range of 15-28 °C for $(POG)_7$, 18-31 °C for $(PPG)_{10}$ and 52-60 °C for $(POG)_{10}$. . In these temperature rages for each CMP, the triple helical structures are expected to find new equilibrium states after the temperature-jump, without drastic thermal denaturation near or above T_m. Kinetic data were collected at 225 nm with a time interval of 10 s and an integration time of 0.7 s.

To calculate f_{TD}, reference spectra were measured for the fully folded state (4 °C) and the fully unfolded state (60 °C for $(POG)_7$ and $(PPG)_{10}$ and 80 °C for $(POG)_{10}$). The reference spectra were measured two times and averaged. Subsequently, the fraction folded was calculated as described above, using the reference values at 225 nm for baseline subtraction.

For obtaining the apparent unfolding rates (i.e. dissociation rates), first-order kinetics was assumed. The fraction folded was plotted in logarithmic scale with a linear time axis. Linear fitting was performed in Origin Pro 2020 (OriginLab Corporation) to acquire the slope of the linear regime in a time window between 5-60 min. The initial 5 min were considered as a dead

time for temperature equilibration. The apparent unfolding rates (k_{off}^{app}) were obtained from the resulting slopes and activation energies were calculated using the Arrhenius equation (**Equation 12**).

$$ln\left(k_{off}^{app.}\right) = - \frac{E_a}{R} \frac{1}{T} + lnA$$

(12)

where E_a is an activation energy of the unfolding event of the triple helices of the CMPs and R is the gas constant of 8.314 kJ mol^{-1} K^{-1}.

3.3.3 Self-reporting system for peptide association/dissociation based on fluorescence self-quenching

Theoretical background

Luminescence is the emission of light from any substance that has absorbed electromagnetic radiation. When the excited electron has the opposite spin as the ground state electron (i.e. the electrons are paired), the emission of a photon is termed fluorescence. As a result of the pairing of the electron spins in the singlet state, the excited electron can relax to the ground state more rapidly and the fluorescence lifetime is near 10^{-9} s. [180]. The absorption and emission process of electromagnetic radiation are illustrated with the Jablonski diagram in **Figure 12**.

The Jablonski diagram describes the absorption and emission of electromagnetic radiation. When the molecule absorbs photons, the electrons in the electronic ground state (S_0) are excited to the excited electronic states (S_1, S_2). Each electronic energy level contains a number of vibrational energy levels in which the electrons can exist. Before absorbing a photon, electrons exist mostly at the lowest vibrational energy in the electronic ground state. At room temperature, thermal energy is not enough to excite the electron to higher vibrational energy levels. When the molecule absorbs enough energy from light, an electron can be excited to a higher energy level (S_1 or S_2 state). Within very short time (10^{-12} s or less), the molecule relaxes thermally and equilibrates at the lowest vibrational level of S_1 through internal conversion. Excited electrons in the lowest vibrational energy level of the S_1 state can return to the ground state (S_0) via the emission of a photon (fluorescence). This fluorescence photon has lower energy (i.e. longer wavelength) than the absorbed photon. This wavelength shift, observed when comparing absorption and emission spectra, is called Stokes shift.
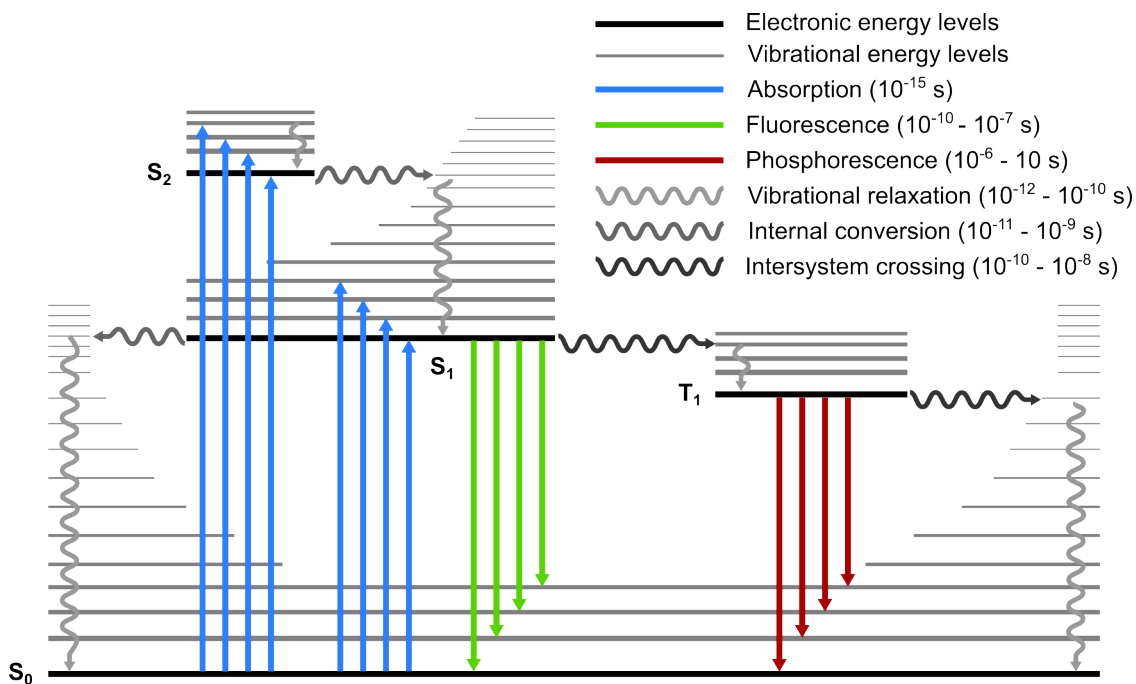
Figure 12. Jablonski diagram showing the processes of luminescence. The energy levels of a molecule with different electronic states are illustrated with black thick lines: S_0 is the singlet ground state of the molecule, S_1 is the first excited singlet state, and S_2 is the second excited singlet state. T_1 means the first excited triplet state. The singlet state is the electronic state when the total spin angular momentum is zero, whereas the triplet state has a total spin angular momentum of one. Each electronic state possesses vibrational states (solid gray lines). The colored arrows represent the various transitions between the electronic states through radiative (straight colored lines) or non-radiative (wavy gray lines) processes. When a molecule absorbs energy from a photon, an electron in the molecule can be excited from the ground state (S_0) to higher electronic states (S_1 or S_2). The associated energy can be released by vibrational relaxation to the S_1 state or even to the S_0 state. When the molecule relaxes in a radiative transition, the molecule emits light and its wavelength is proportional to the energy gap between the excited state and the grounded state. This process is called fluorescence (solid green lines). Through intersystem crossing, the excited energy in the singlet state can also be transferred to the triplet sate. This ultimately results in phosphorescence (radiative emission). Alternatively, the excited electron can return to the ground state by vibrational relaxation (non-radiative transition).

Electrons in the singlet excited state (S_1) can also undergo a spin conversion to the triplet state (T_1), in which the electron has the same spin with the ground-state electron. This process is called intersystem crossing. Emission of a photon upon transition from T_1 to S_0 is called phosphorescence. Due to the restriction in spin orientation, rate constants of phosphorescence are much smaller than those of fluorescence.

In general, molecules that are able to emit fluorescence, also called fluorophores, are aromatic structures with delocalized electrons. Typical examples are 5(6)-carboxyfluorescein (**Figure 9**) and rhodamine. Pairs of fluorescein and rhodamine are broadly used as donor and acceptor fluorophores for FRET. In the presence of FRET, the donor molecule relaxes to the ground state without photon emission, while its energy is transferred to the acceptor. As a result of this non-radiative energy transfer from the donor to the acceptor, the acceptor emits a photon upon returning to the ground state.

Fluorescence is generally measured using a spectrofluorometer. In a typical spectro-fluorometer, fluorescence is excited using a xenon arc lamp (or flash lamp for a standard microplate reader). The light then passes an excitation monochromator, which consists of two gratings to separate light with a single wavelength. This light enters to the sample chamber and passes through the sample cuvette directly. Fluorescence is collected at 90° angle to the incident light path in order to minimize the amount of excitation light reaching the detector. An emission monochromator scans and separates the emitted fluorescence and photons of the selected wavelength are detected with a photomultiplier tube.

The efficiency of fluorescence emission can be reduced by specific processes in the surroundings of the fluorophore, such as collisions with solvent molecules (or other quenchers), excited-state reactions, ground-state complex formation, and molecular rearrangements. This process is referred to as fluorescence quenching. Quenching and the resulting decrease in fluorescence intensity is usually avoided; however, it can also be used as a source of information about structural or conformational changes, e.g. occurring during protein folding (or dissociation). Particularly, fluorescence self-quenching is a powerful tool to study protein association or conformational changes at a single molecular level [145, 181]. Fluorescence emission can be quenched as a result of intermolecular interactions when two identical fluorophores are in close proximity. Therefore, when two fluorophores come into proximity upon protein association, the resulting decrease in fluorescence intensity can be used for spectroscopically monitoring the association reaction. Accordingly, the intensity is recovered when the distance between two dyes increases upon dissociation of the protein. Self-quenching requires almost van der Waals distance while FRET occurs at longer distances, typically 10-100 Å [181]. While the choice of reporter system largely depends on the protein structure, self-quenching is the method of choice for homooligomeric molecules (e.g. CTHs) as only one type of fluorophore is needed. Instead, FRET may be the better choice for heterooligomeric molecules where the introduction of two different fluorophores is synthetically easier to achieve.

Experimental procedure

To quantify the fluorescence of the CF-labeled CMPs, the CF-$(PPG)_{10}$ and CF-$(POG)_7$ peptides were subjected to fluorescence measurements with a spectrofluorometer (FluoroMax4, HORIBA Jobin Yvon GmbH, Bensheim, Germany).

For thermal denaturation measurements, the CF-$(PPG)_{10}$ solutions were prepared in PBS with a concentration of 0.1 µM. The emission spectra were recorded over a wavelength range of 505-650 nm with an excitation wavelength of 497 nm in 1 nm steps and with a bandwidth of

5 nm. The integration time was 0.1 s. For the fully associated state of CF-(PPG)$_{10}$ (i.e. homotrimeric state), the spectrum was measured at 4 °C after overnight storage at 4 °C. The temperature was increased to 47 °C and an emission spectrum was measured again to determine the intensity of the fully dissociated state (i.e. monomeric state).

For chemical denaturation measurements, a guanidinium chloride (GdmCl) solution was prepared in PBS with a concentration of 3 M. The CF-(POG)$_7$ solutions were prepared with a concentration of 0.5 μM both in 3M GdmCl/PBS solutions and in PBS as a control. The emission spectra were recorded over a wavelength range of 505-650 nm with an excitation wavelength of 497 nm in 1 nm steps and with a bandwidth of 5 nm.

To quantify the dissociation kinetics of the CMPs, the CF-CMPs were subjected to a competitive assay and the change in the fluorescence intensity was monitored with the spectrofluorometer. For CF-(PPG)$_{10}$, the peptides were prepared in PBS with a concentration of 0.5 μM. To reduce undesired disulfide bonds, TCEP was added to a concentration of 5 μM. The unlabeled (PPG)$_{10}$ solution was prepared in PBS with a concentration of 50 μM (100x excess) and mixed with the CF-(PPG)$_{10}$ solution in a 1:1 ratio (v/v). Fluorescence intensity was immediately monitored for an emission at 524 nm and an excitation at 497 nm. The integration time was 0.1 s. The data points were collected every 60 s for 86400 s (24 h).

For CF-(POG)$_7$, the peptide solution was prepared in PBS with a concentration of 0.5 μM and TCEP was added to a concentration of 5 μM. The unlabeled (PPG)$_{10}$ solution was prepared in PBS with a concentration of 5 μM (10x excess) and mixed with the CF-(POG)$_7$ solution in a 1:1 ratio (v/v). The sample was measured at an emission wavelength of 524 nm, directly after mixing the two solutions. The excitation wavelength was 497 nm. The integration time was 0.1 s. The data points were collected every 160 s for 86400 s (24 h).

To observe long-term dissociation kinetics of CMPs, CF-(POG)$_7$ solution was prepared in PBS with a concentration of 0.5 μM and TCEP was added to a concentration of 5 μM. A solution of unlabeled (POG)$_{10}$ was prepared in PBS with a concentration of 5 μM (10x excess) and mixed with the CF-(POG)$_7$ solution in a 1:1 ratio (v/v). The emission spectra were recorded over a wavelength range of 505-650 nm with an excitation wavelength of 497 nm. The integration time was 1 s. The emission spectra were measured for a week. After a week of measurement, the temperature increased to 70 °C and the emission spectrum was measured again to observe the change in fluorescence upon thermal denaturation.

To document a visual color change of the CF-(POG)$_7$ solutions, photographs were taken. The CF-(POG)$_7$ solutions were prepared in PBS with a concentration of 0.25 mM and mixed with unlabeled (POG)$_{10}$ solutions prepared in PBS with a concentration of 2.5 mM (10x excess) in a 1:1 ratio (v/v). TCEP was added to a concentration of 6 mM. As a control, the CF-(POG)$_7$

solution (0.25 mM) was mixed with PBS buffer in a 1:1 ratio (v/v). The colors of both solutions were observed at RT and both solutions were heated to 70 °C for 20 min. The change in color was observed again. After heating, the solutions were stored at 4 °C for 3 days to allow re-association of the CTH structures and the colors of the solutions were observed.

3.4 Viscoelastic and mechanical properties of CMP- and CC-crosslinked hydrogels based on the bulk shear rheology

To understand the viscoelastic and the mechanical properties of the hydrogels, conventional bulk shear rheology was used in this study. This chapter gives the theoretical background about rheology and the methods used in the hydrogel experiments.

Theoretical background

Rheology is the science about the flow behavior of fluids and the deformation behavior of solids. Most biomimetic materials have both a viscous and an elastic character and are therefore called viscoelastic. Shear rheology has been widely utilized to study the viscoelasticity of bulk materials. Viscoelasticity of materials can be described with the Maxwell model that is a serial combination of a spring and a dashpot or the Kelvin-Voigt model that is a parallel combination of a spring and a dashpot (**Figure 13**). The spring represents ideally elastic behavior that follows Hooke's law:

$$\sigma = G \cdot \gamma \tag{13}$$

where σ is the shear stress, γ is the shear strain, and G is the shear modulus.

The dashpot expresses ideally viscous behavior, according to Newton's law:

$$\sigma = \eta \cdot \dot{\gamma} \tag{14}$$

where η is the shear viscosity and $\dot{\gamma}$ is the shear rate.
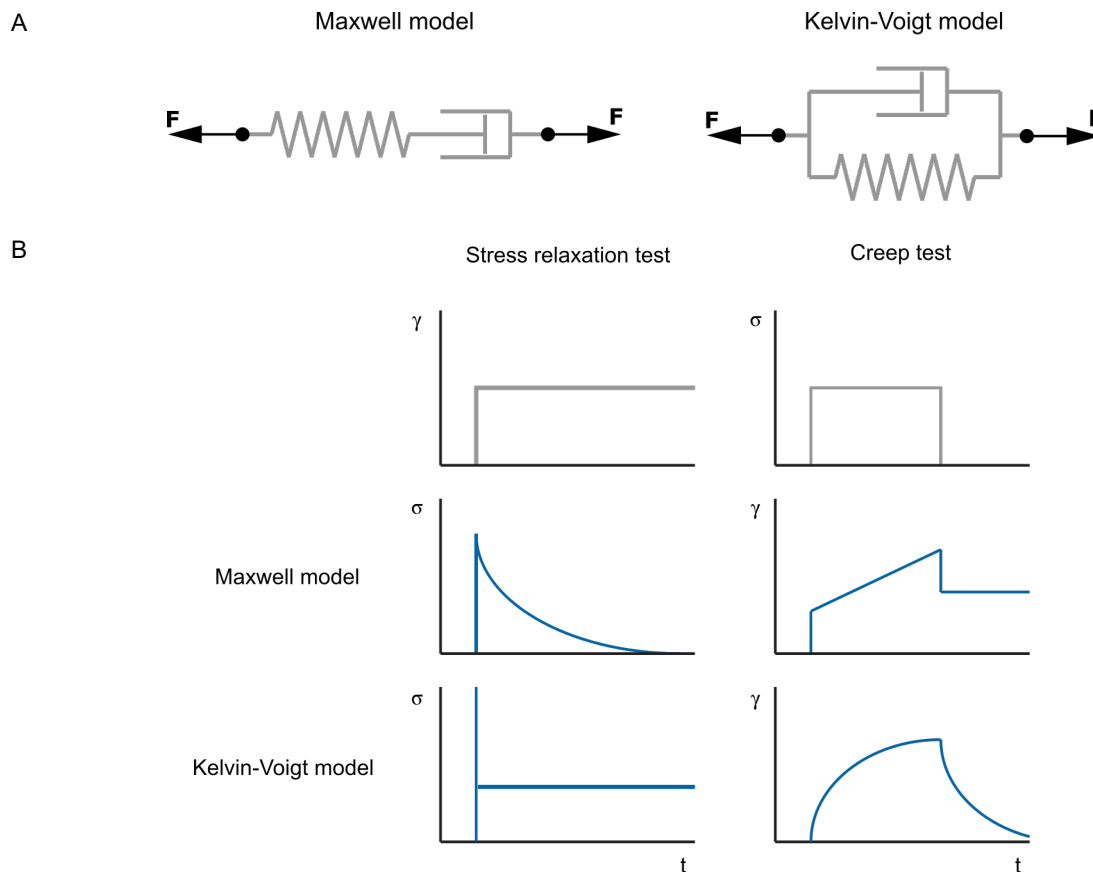
Figure 13. Maxwell and Kelvin-Voight models for viscoelastic materials. A A Maxwell element (a spring and a dashpot in serial connection) or Kelvin-Voigt element (a spring and a dashpot in parallel) can be used as the two simplest descriptions for viscoelastic materials. The spring represents the elastic portion of the viscoelastic material and the dashpot represents the viscous portion. **B** Stress response in a stress relaxation test (left column) and strain response in a creep test (right column). For the stress relaxation test, a constant strain is applied (gray) to a material and the corresponding stress responses are shown below (blue). For the creep test, a constant stress is applied (gray) and the strain responses are shown below (blue). For stress relaxation tests of viscoelastic materials, the Maxwell model can be used to obtain the relaxation time in general, whereas the Kelvin-Voigt model is used for creep tests. Often more complex combinations of springs and dashpots are required to be used to fully describe the viscoelastic responses.

Stress relaxation and creep behavior are a characteristic for viscoelastic materials. In general, stress relaxation of viscoelastic material can be described with the Maxwell model and the Kelvin-Voigt model fits better for creep behavior. In this work, stress relaxation was the method of choice because of the broad biological relevance. To describe stress relaxation of the viscoelastic materials, the Maxwell model can be used in the form of the following differential equation.

For viscoelastic materials, the total deformation was assumed as the sum of the individual strains acting on the the spring (γ_e) and the dashpot (γ_v) by the Maxwell model (**Equation 15**). The total stress equals the individual stresses ($\sigma_e = \sigma_v$) (**Equation 16**)

$$\gamma = \gamma_v + \gamma_e \tag{15}$$

$$\sigma = \sigma_v = \sigma_e \tag{16}$$

From Newton's law (**Equation 14**), the viscous element can be described as

$$\dot{\gamma}_v = \frac{\sigma_v}{\eta} \tag{17}$$

where η is the dynamic viscosity.

Hooke's law (**Equation 13**) applies to the elastic element with time derivative ($\dot{\sigma} = {d\sigma}/{dt}$):

$$\dot{\gamma}_e = \frac{\dot{\sigma}_e}{G} \tag{18}$$

where G is the shear modulus.

From the sum of the shear rates, the differential equation of the Maxwell model is obtained as

$$\dot{\gamma} = \dot{\gamma}_v + \dot{\gamma}_e = \frac{\sigma_v}{\eta} + \frac{\dot{\sigma}_e}{G} = \frac{\sigma}{\eta} + \frac{\dot{\sigma}}{G} \tag{19}$$

The relaxation time τ is the ratio of the dynamic viscosity and the shear modulus from the Maxwell model:

$$\tau = \frac{\eta}{G} \tag{20}$$

Therefore, the differential equation of the Maxwell model can be rewritten as

$$\dot{\gamma} \cdot \eta = \sigma + \tau \cdot \dot{\sigma} \tag{21}$$

The solution of the differential equation leads to the following time-dependent exponential function.

$$\sigma = \gamma \cdot G \cdot exp\left(-\frac{t}{\tau}\right) \tag{22}$$

When the time point $t = \tau$, $\sigma(\tau) = 0.368 \cdot \sigma_{max}$. In other words, the relaxation time is defined as the time at which the time-dependent shear stress value reaches 36.8 % of the initial stress after step-strain. These theoretical calculations of the Maxwell model can be applied to the Kohlrausch-Williams-Watts (KWW) equation in a stress relaxation tests to obtain the relaxation time in the following section.

A rheometer is a device that measures the various material properties based on the two-plate model (**Figure 14-A**). In this system, the sample is placed between two plates. The upper plate is in motion with velocity (v), driven by a shear force (F), while the lower plate is stationary

(v = 0). In this way, shear deformation is applied to the sample. The deformation applied by the rheometer is either rotational or oscillatory, depending on the motion of the upper plate.
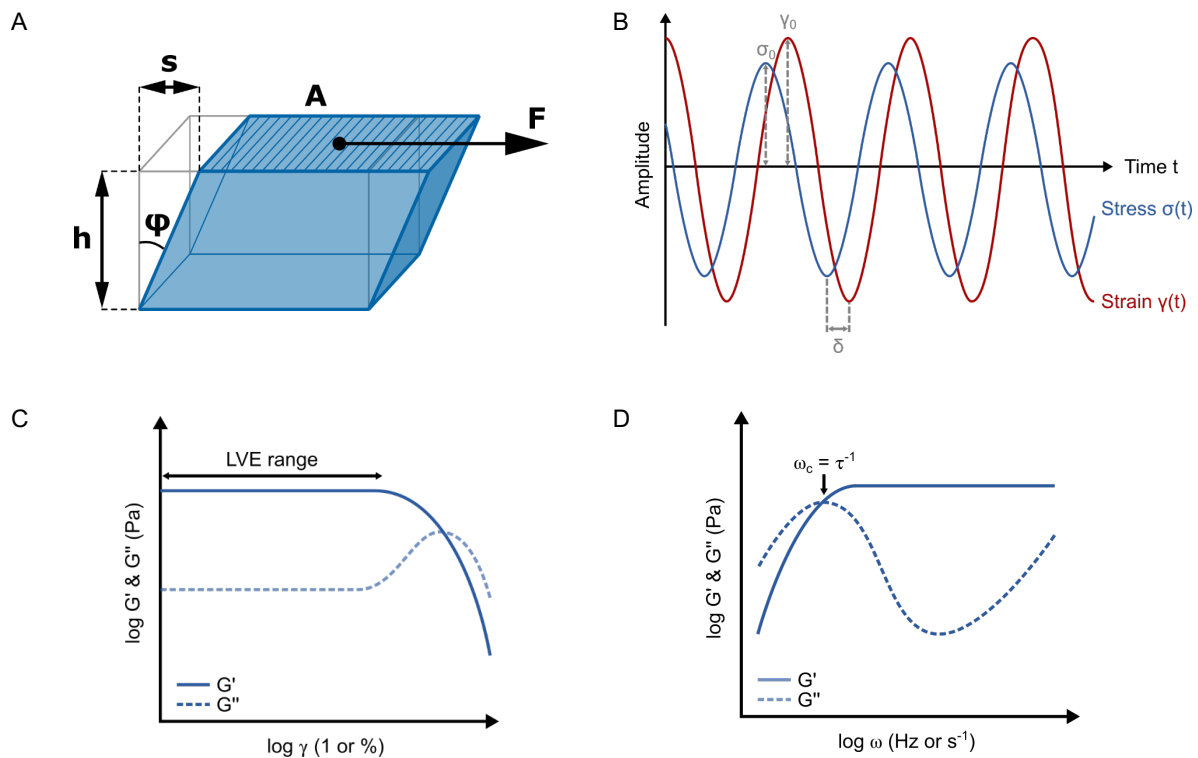
Figure 14. Basic concept of oscillatory shear rheology. A Two-plate model used for shear rheology with shear area A, gap width h, shear force F, deflection path s, and deflection angle φ. From these quantities, the shear stress ($\sigma = F / A$ in Pa), and shear strain (i.e. shear deformation, $\gamma = s / h$ with the unit 1 or %) are defined. **B** Phase shift during an oscillatory test, indicating viscoelastic behavior. Time dependent stress $\sigma(t)$ and strain $\gamma(t)$ are presented as sinusoidal functions of time. In the two curves, the amplitudes of stress σ_0 and strain γ_0 are displayed together with the phase shift δ. **C** Amplitude sweep, showing the storage modulus G' (solid line) and loss modulus G" (dotted line) as a function of strain amplitude γ. The double headed arrow shows the linear viscoelastic (LVE) region where the storage modulus is constant. When the storage modulus is higher than the loss modulus (G' > G"), the material exhibits solid-like behavior. The plateau modulus G_p is defined as the averaged values of the storage moduli in the LVE region. The strain value at the end of the LVE region can be defined as yield point of the material. The strain value at the crossover of the storage modulus and loss modulus (G'=G") is also called flow point. At higher strain, the viscous portion will dominate and the sample flows (G" > G'). **D** Frequency sweep, showing the storage modulus G' (solid line) and loss modulus G" (dotted line) as a function of angular frequency ω. The crossover frequency (ω_c) of G' and G" can represent the inverse of the relaxation time (τ) of the material ($\omega_c = \tau^{-1}$).

For the characterization of viscoelastic material properties, oscillatory shear is usually performed, either using a stress-controlled or strain-controlled protocol. The resulting strain is sinusoidal when stress is applied in a sinusoidal way. Viscoelastic materials show a phase shift (δ) between the two sinusoidal curves of stress and strain ($0\,° < \delta < 90\,°$) (**Figure 14-B**). In contrast, the strain response is immediate without phase shift ($\delta = 0\,°$) for ideal elastic behavior and the strain responses is out of phase ($\delta = 90\,°$) for ideally viscous materials. Thus,

viscoelasticity is a mixture of viscous and elastic material responses where the phase angle lies between 0° and 90°.

In shear rheology, the complex shear modulus G* [Pa] is defined as the ratio of the time-dependent sine functions of stress σ(t) and strain γ(t):

$$G^* = \frac{\sigma\,(t)}{\gamma\,(t)} = G' + iG''$$ (23)

where G' is the storage modulus, G" is the loss modulus, and i is the imaginary unit.

The complex modulus describes the combined elastic and viscous response of the material resisting against the deformation. The storage modulus G' describes the energy stored (elastic component) during the shear deformation and the loss modulus G" represents the energy dissipated due to internal friction (viscous component).

$$G' = \frac{\sigma_0}{\gamma_0}\,cos\delta = G^*\,cos\delta$$ (24)

$$G'' = \frac{\sigma_0}{\gamma_0}\,sin\delta = G^*\,sin\delta$$ (25)

When G' > G", the viscoelastic material shows solid-like behavior, whereas it acts like liquid when G" > G'. G' is directly proportional to the crosslinking density [182]. The ratio of G" and G' called loss factor (G"/G' = tanδ). It is a useful parameter to describe energy dissipation during cyclic deformation [183].

The so-called linear viscoelastic range (LVE; **Figure 14-C**) of a material can be determined in a so-called amplitude sweep (AS). The material is strained at a constant oscillation frequency while the amplitude of the strain is gradually increased. In addition to the LVE, also the plateau modulus G_p, can be obtained from the G' values in the LVE plateau region. The plateau modulus is directly related to the stiffness of the material. Once the LVE has been determined, small-amplitude oscillatory shear (SAOS) rheology is frequently utilized for studying the viscoelastic properties of biomimetic materials (e.g. hydrogel). In a frequency sweep (FS), a small oscillatory strain within the LVE region is applied to the material while the frequency of the oscillation is altered. Also from this experiment, the plateau modulus G_p can be determined from the G' values within the plateau range (**Figure 14-D**). In addition, the relaxation time τ_{FS} can be extracted from the crossover of G' and G" (ω_c; **Equation 26**).

$$\tau_{FS} = \frac{1}{\omega_c}$$ (26)

Relaxation of stress, in response to an externally applied strain, is a critical feature of viscoelastic biomaterials. Stress can be released via the rupture of non-covalent (or physical) crosslinks in the network. It has been shown that the characteristic relaxation time depends on the thermodynamics and kinetics of the crosslinks [67] but also on the topology of the network, which determines how load-bearing chains are affected by crosslink rupture [184]. In addition to a FS, the relaxation time can also be obtained with the step-strain method (**Figure 15**). Here, a constant strain is applied to the material and the relaxation of the resulting stress is measured as a function of time. Step-strain relaxation tests are favored when the relaxation time is longer than what can be measured with a FS.
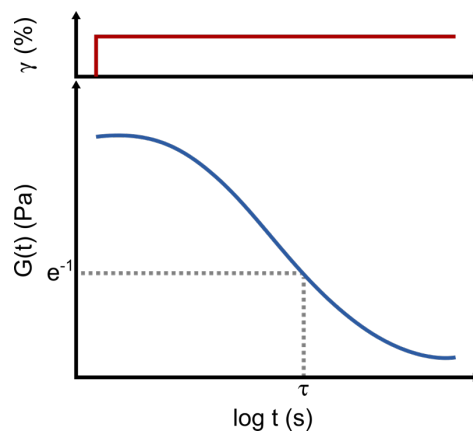
Figure 15. Stress relaxation tests using shear rheology. Shear rheometer can apply a constant strain in a stepwise manner and the relaxation of the applied stress is monitored over time, i.e. the relaxation modulus is monitored as a function of time (G(t) = σ(t) / γ). The data is usually fitted with the Kohlrausch-Williams-Watts (KWW) exponential function (**Equation 27**). The relaxation time (τ) obtained from the KWW fit corresponds to the time when the stress reaches to 36.8 % of the initial value during the relaxation.

In the stress relaxation test, the relaxation modulus G(t) is measured as a function of time. The characteristic time τ_{SR} can be calculated using the KWW exponential function [185]:

$$G(t) = G_o \, exp\left[-\left(\frac{t}{\tau_{SR}}\right)^{\alpha}\right] \tag{27}$$

where G_o is the initial plateau modulus, α is the fitting parameter or relaxation exponent. If relaxation can be described by a single exponential function $\alpha = 1$. Stretched exponential relaxation is observed when the α values are between 0 and 1 ($0 < \alpha < 1$). And for α values higher than 1 but lower than 2 ($1 < \alpha < 2$), the material relaxes with a compressed exponential.

Experimental procedure

The CMPs were dissolved in borate buffer at a peptide concentration of 6 mM. This corresponds to 2 mM of folded triple helical structures (i.e. network crosslinks). After the peptides were fully dissolved, the CMPs coupled to 4-arm star-PEG terminated with NHS ester (40k Da; Jenkem, Plano, USA). The star-PEG powder was directly added to the peptide solution for a final concentration of 1.5 mM. This results in a stoichiometric ratio (1:1) of amine groups on the peptides and NHS esters of the PEG. The mixture was incubated at RT (22-23 ˚C) for 30 min with gentle shaking at 800 rpm. Gelation was observed within this time. To allow equilibration, the measurements were performed after the hydrogels were incubated for over 12 h at 4 ˚C.

For the CC-crosslinked hydrogels, the CC-forming peptides were dissolved in coupling buffer to a peptide concentration of 6 mM. This corresponds to 3 mM of folded triple helical structures for CC-Homo2 and CC-Hetero2 and 2 mM of folded triple helical structures for CC-Homo3 and 1.5 mM of folded triple helical structures for CC-Homo4. After the peptides were fully dissolved, they were coupled to 4-arm star-PEG terminated with maleimide groups (40k Da; Jenkem, Plano, USA). The star-PEG powder was directly added to the peptide solution to gain a final concentration of 1.5 mM. This results in a stoichiometric ratio (1:1) of amine groups on the peptides and maleimide groups of the star-PEG. CC-Homo4 was also coupled to linear PEG terminated with maleimide groups (20k Da; Jenkem, Plano, USA). The linear PEG powder was added to the peptide solution in the same way but the final concentration was 3 mM to obtain a stoichiometric ratio (1:1) of cysteine groups on the peptides and maleimide groups of the linear PEG. The mixture was incubated at RT for 30 min with gentle shaking at 800 rpm. Gelation was observed immediately. To allow equilibration, the measurements were performed after the hydrogels were incubated for over 12 h at 4 ˚C.

A shear rheometer (MCR301 or MCR302, Anton Paar, Ostfildern-Scharnhausen, Germany) was used to characterize all hydrogels. The measurement was performed with cone-plate geometry, using a diameter of 12 mm (CP-12, 0.02 mm gap, 1° cone angle; Anton Paar, Ostfildern-Scharnhausen, Germany). The measurement temperature was 25 °C unless stated otherwise. Water was filled in a trough around the sample table and a temperature-controlled hood was used. In this way, a humid atmosphere is produced that slows down evaporation of the sample.

To determine the LVE region of the hydrogels, amplitude sweeps were performed. Strain amplitudes were varied from 0.1 % to 1000 % while applying a constant angular frequency of 10 rad s^{-1}. An amplitude sweep with an ascending strain amplitude was followed by another amplitude sweep with descending strain amplitude (1000 % to 0.1 %) at the same constant

angular frequency were conducted two times. The flow strain of the hydrogel was determined at the crossover of G' (storage modulus) and G'' (loss modulus).

Frequency sweeps were subsequently conducted to study the frequency-dependent mechanical behavior of the network. The angular frequency was varied from 100 to 0.001 rad s^{-1} while applying a constant strain amplitude of 1 or 10 % (both values are in the LVE region). The characteristic relaxation time can generally be obtained from the inverse of the crossover frequency, ω_c in units of Hertz (Hz = s^{-1}) (**Equation 26**). For the CMP hydrogels, no crossover was observed in the frequency range tested, suggesting that the relaxation of the obtained networks is slower than what can be measured in a typical frequency sweep.

To investigate the self-healing behavior of the hydrogels, a series of step-strain measurements was carried out, where low and high amplitudes of oscillatory shear strains were alternated. After loading a sample, a constant strain amplitude of 0.1 % with a constant angular frequency of 10 rad s^{-1} were applied for 30 min with data collection every 10 s. Subsequently, a high strain amplitude of 1000 % was applied for 10 min, using the same angular frequency of 10 rad s^{-1}. During this interval, the hydrogel network is perturbed or may rupture. Recovery of G' was subsequently followed by applying oscillations with an amplitude of 0.1 % for 60 min. This cycle was repeated one more time. In the third cycle, a strain amplitude of 0.1 % was applied for 10 h after the high strain interval to follow the evolution of G' over an extended period of time.

Stress relaxation tests were performed as an alternative method to determine the relaxation behavior of the CMP-crosslinked hydrogels. Before each stress relaxation experiment, two amplitude sweeps with ascending and descending strain amplitude were conducted as described above. These amplitude sweeps allowed for applying pre-stress to the material, using a defined protocol. After the second amplitude sweep, the position of the measuring system was reset so that the sample experienced 0 % strain (reset γ) and kept at this position for a pre-determined time between 1-120 min. During this waiting time, the evolution of the stress was recorded every 10 s. After again re-setting the strain to 0 %, a strain of 5 % was applied in a stepwise manner and the relaxation modulus was subsequently monitored. The obtained relaxation curves were normalized with the initial plateau value (G$_0$) and fitted with the KWW equation to obtain the relaxation times and the relaxation exponents (**Equation 27**).

Stress relaxation experiments were also performed at different temperatures to investigate the effect of temperature on τ_{SR} and the fitting exponent α. Two different series of experiments were performed. In the first series, all CMP-crosslinked hydrogels were measured at identical temperatures of 5 °C and 25 °C. In the second series, different temperatures were used such

that the fraction folded was 0.99 for each CMP. In detail, temperatures of 15 °C, 20 °C and 47 °C were used for the CMPs $(POG)_7$, $(PPG)_{10}$ and $(POG)_{10}$, respectively.

As a control to test if the mechanical history of the sample affects stress relaxation, two alternative protocols were utilized for applying pre-stress (**Figure 16**). Instead of resetting the strain after the amplitude sweeps, the stress was set to 0 Pa during the waiting time. Further, the amplitude sweep, which finishes with a low strain amplitude, was replaced with a large immediate step strain (e.g. 1000 %). This large strain was then held constant during the waiting time and an additional step-strain of 5 % was applied for the following stress relaxation measurement.
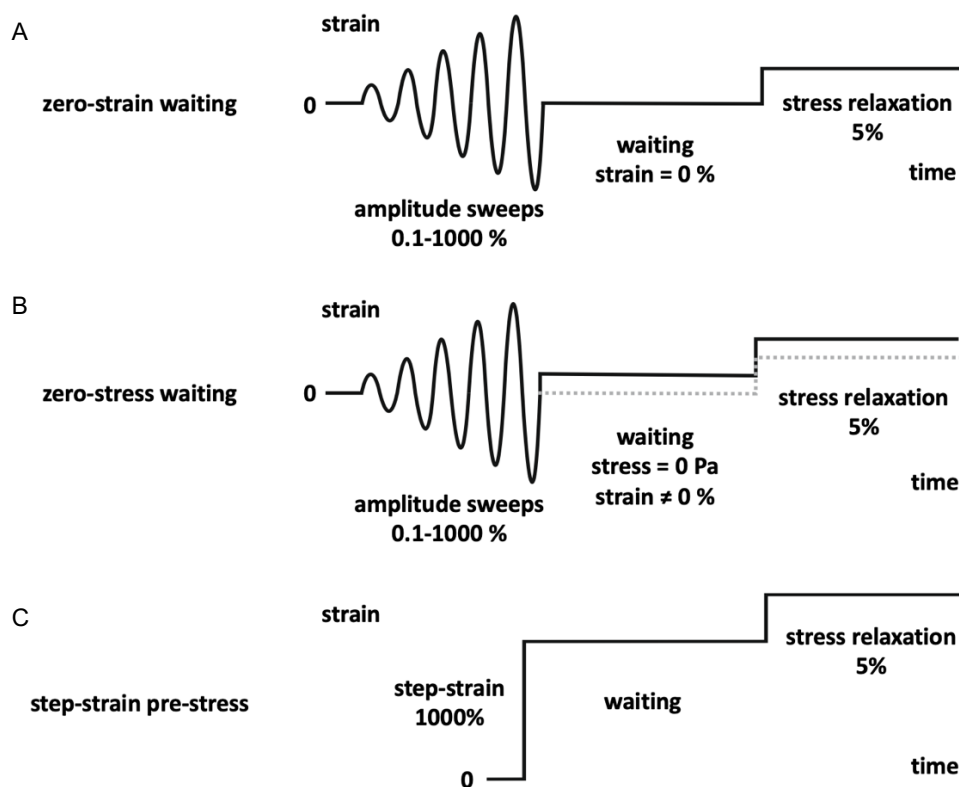
Figure 16. Scheme of the three different experimental protocols used for the stress relaxation tests. A Zero-strain waiting protocol. After the amplitude sweep (AS) is done, the rheometer remains at zero strain which was set as the initial starting point before AS. **B** Zero-stress waiting protocol. Due to the remained stress, the rheometer needs to apply additional strain right after AS to maintain the stress to 0 Pa during the waiting time. An additional strain of 5 % needs to be applied on the top of the strain applied for the waiting to perform the following stress relaxation test. **C** Step-strain-based protocol for applying pre-stress. A constant step-strain of 1000 % is applied once and the relaxation of the applied stress is monitored during the waiting time. An additional strain of 5 % is applied for the following stress relaxation test.

4 Results

4.1 Experimental design

CTHs and α-helical CCs are fundamental building blocks of protein-based biological materials and are ubiquitously found in the ECM and cytoskeleton. At a molecular level, amino acid sequence is related to their characteristic supramolecular structure. The thermodynamic and kinetic properties of the folded structures are also affected by the sequence and length of the CTH- and CC-forming peptides. CTHs are known to possess uniquely slow association and dissociation kinetics. In this work, I employed well-characterized and commonly used simplified CTH model peptides. Choosing $(PPG)_{10}$, $(POG)_7$ and $(POG)_{10}$ provided sequence and length control of the CTH structures. CCs are also prevalent protein association motifs in the cytoskeleton and the ECM. In this work, they have been used as a model system for studying the effect of the crosslink functionality and thus network connectivity (see **Aims of this Thesis**).

In order to elucidate how the molecular properties of the model peptides translate into the mechanical and viscoelastic properties of ECM-inspired polymer hybrid hydrogels, I designed a series of simple CMP and CC sequences and utilized them as physical and dynamic crosslinks in PEG polymeric networks. This is expected to fill an important gap in knowledge and will answer the question which molecular properties are key design parameters for the bottom-up design of viscoelastic hydrogels. In order to achieve this goal, I used the CMPs and CCs to dynamically crosslink biocompatible star-PEG polymers to obtain structurally well-defined hydrogel networks. I further performed biophysical and physicochemical analysis of the peptide building blocks and correlated the results obtained for the peptide molecules with the bulk rheological behavior of the hydrogels.

In the following, I will introduce the experimental design implemented to answer the following 3 questions (see also **Aims of this Thesis**):

1) How do the thermodynamic and kinetic properties of CMP-based crosslinks affect the viscoelastic properties of the collagen-inspired hydrogels?

In order to study how the thermodynamic and kinetic properties of CMPs determine their function as dynamic crosslinks, I designed a CMP-crosslinked hydrogel system based on a 4-arm star-PEG polymeric backbone (**Figure 17**).
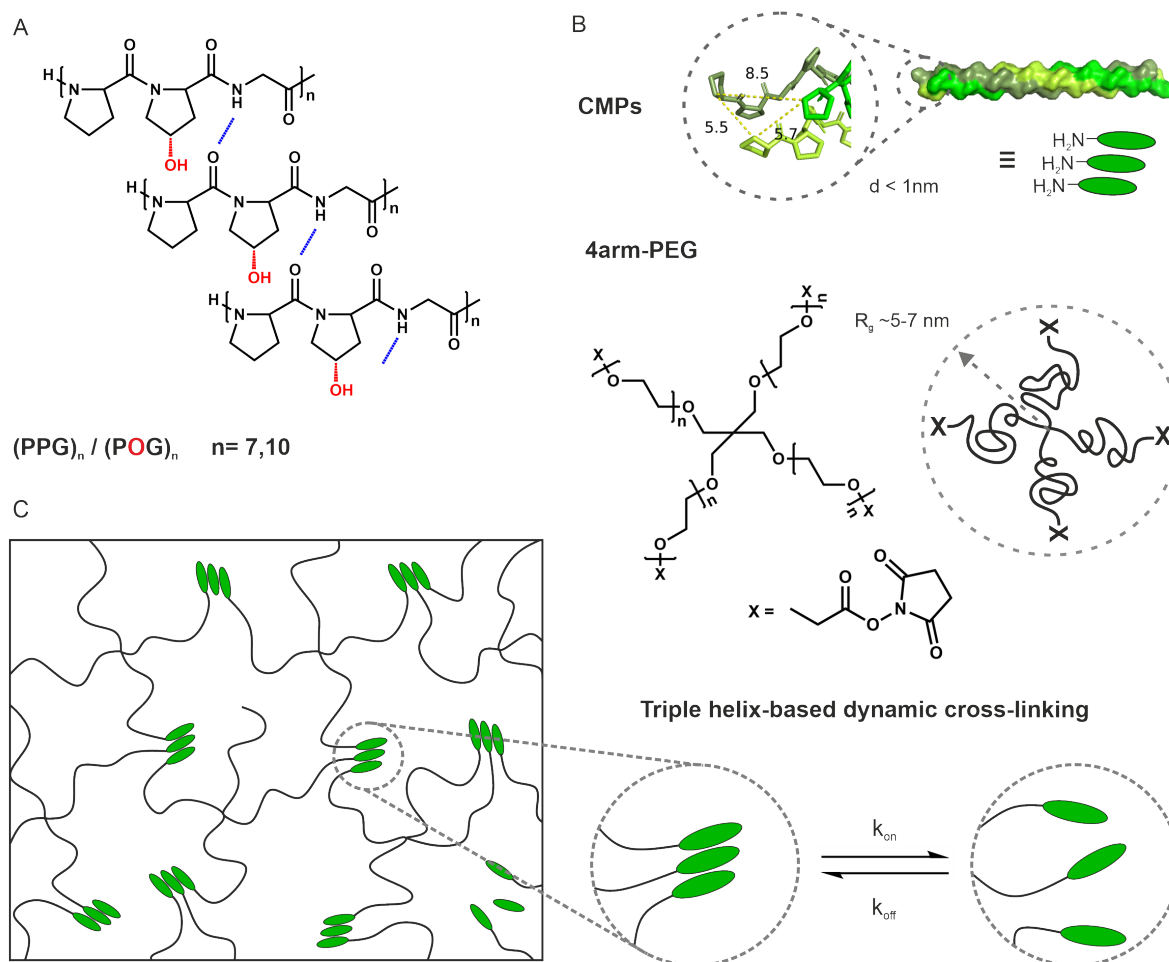
Figure 17. Collagen-inspired hydrogels. A CMPs with the sequence of $(PPG)_{10}$, $(POG)_7$ and $(POG)_{10}$ were used for self-assembled triple helical motifs. The chosen CMPs allow to compare the effects of peptide sequence and length. In the folded structure, three individual chains are staggered by one amino acid to facilitate interchain hydrogen bond formation (blue dotted lines). **B** The CMPs were utilized as dynamical crosslinks in the star-PEG (4-arm PEG, MW = 40kDa, x = NHS ester functional group) polymeric network. The N-terminal amine of the CMPs is coupled with the NHS ester-terminated PEG. The representative $(PPG)_{10}$ structure was drawn and the end-to-end distances between nitrogen atoms in the Pro rings at the N-termini were calculated with PyMOL Molecular Graphics System, Version 2.5.1 (Schrödinger, LCC, PDB ID of $(PPG)_{10}$: IK6F). As a result of the small distance between the N-termini of the triple helical structure (calculated average distance: 6.6 Å) and the radius of gyration (R_g) of the star-PEG (5-7 nm), the reaction of all 3 N-terminal amines could be sterically hindered, the resulting network thus is expected to be heterogeneous due to unideal coupling reactions. **C** Scheme of the anticipated hydrogel network. The formed network is expected to contain intrinsic topological defects, such as dangling ends, primary loops, etc. The CMP-crosslinks can be dissociated with external stimuli, e.g. force or temperature change. The dissociated crosslinks can be reassociated through CMP self-assembly. At thermodynamic equilibrium, the CMP-crosslinks dissociate and re-associate with rate constants k_{on} and k_{off}, respectively.

The peptides $(PPG)_{10}$, $(POG)_7$ and $(POG)_{10}$ were used. Their different sequence and length, and thus thermodynamic and kinetic properties (see **Aims of this thesis**), allow for a systematic analysis of the role of their molecular properties on the viscoelastic behavior of the bulk hydrogel network. Besides peptide length, the key difference is the presence of a hydroxyl group (-OH) on the Pro ring in the Y position (**Figure 17-A**). As a first step, the thermodynamic stabilities were validated and compared to literature values [103, 186] and the dissociation rates of the CMPs were determined using temperature-jump CD experiments. Apparent dissociation rates at different temperatures were further used to determine the activation energy from Arrhenius plots. The CMPs were subsequently used to dynamically crosslink 4-arm star-PEG (40k Da) and the bulk material properties were analyzed (**Figure 17-B and C**). The $(POG)_7$-, $(POG)_{10}$-, and $(PPG)_{10}$-crosslinked hydrogels are expected to possess similar network structures, considering that they all form trifunctional crosslinks and that the same coupling chemistry was used. These networks are thus an ideal starting point to investigate the effect of crosslink thermodynamics and kinetics on the network properties. Using shear rheology, first the linear viscoelastic regime of the network and the self-healing behavior were analyzed. More importantly, stress relaxation was investigated, which is expected to reflect the slow dynamics of CTH association and dissociation. Stress relaxation was tested using the step-strain method and different pre-stress protocols were implemented to test possible out-of-equilibrium effects and aging. To prove a direct relationship between the kinetics of the CMP-crosslinks and stress relaxation of the networks, temperature-controlled stress relaxation tests were further carried out. Besides CMP length and sequence, also the temperature affects the kinetics of the crosslinks. Temperature-controlled experiments are thus an alternative strategy to investigate the relationship between crosslink kinetics and network relaxation.

2) How does crosslink functionality affect the material properties of CC-inspired hydrogels?

Because of their triple helical nature, CMPs always have a crosslink functionality of 3 (see **Chapter 1.2.3**). In order to study the effect of the crosslink functionality in the bulk hydrogel network, α-helical CCs were introduced into the peptide-polymer hybrid hydrogels. CCs provide a great model platform for designing crosslink with different oligomerization states. Depending on the hydrophobic residues, located at *a* and *d*

positions in CC heptad, dimeric, trimeric and tetrameric superhelices can be obtained (**Figure 18-A**).
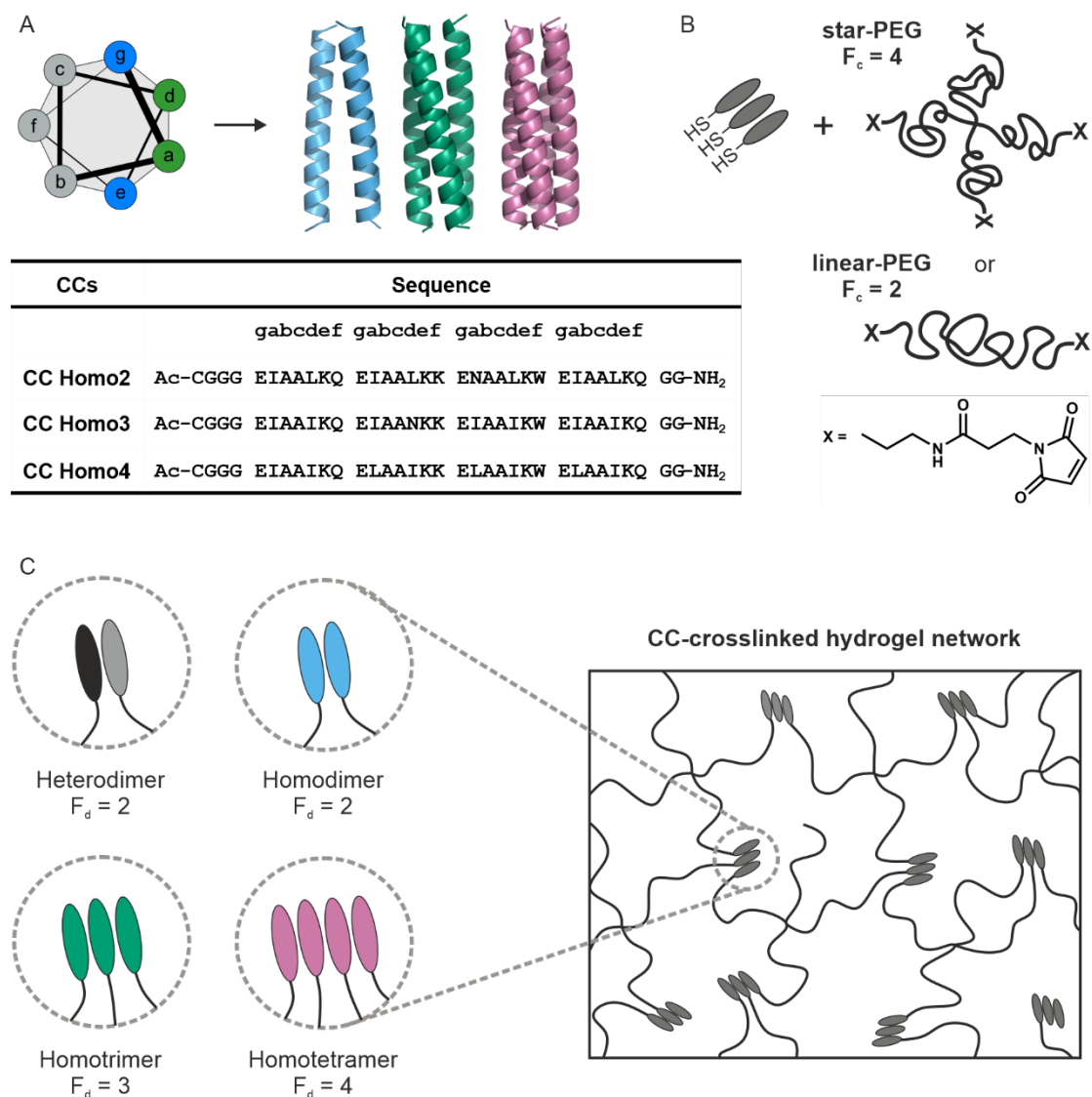
Figure 18. CC-crosslinked hydrogels. A Series of different CC oligomerization states. Hydrophobic residues in *a* and *d* positions of the CC heptad determine oligomerization states of the CC superhelical formation [85]. The structures were predicted using CCBuilder 2.0 and produced using PyMOL Molecular Graphics System, Version 2.5.1 Schrödinger, LLC. **B** Scheme of a trimeric CC and PEGs to describe the coupling reaction. Each peptide of CCs is coupled with 4-arm star-PEG ($F_c = 4$, MW = 40k Da, x = maleimide functional group) and/or linear-PEG (2-arm, $F_c = 2$, MW = 20k Da, x = maleimide functional group). Cysteines (-SH) are located at the N-termini of the peptides to facilitate coupling to the maleimide groups at the PEG arms. **C** The anticipated CC-crosslinked network based on the star-PEG polymeric backbone with trimeric CC crosslink. In addition to homooligomeric CCs, a previously characterized CC-heterodimer (Hetero2, A_4B_4 **Table S1** [113]) was also used as a reference system.

The different CC oligomerization states were utilized to control the functionality of the dynamic crosslinks in the hydrogel network. The CC homodimer served as divalent crosslink ($F_d = 2$) while the CC homotrimer became a trivalent crosslink ($F_d = 3$) and

the CC homotetramer a tetravalent crosslink (F_d = 4) (**Figure 18-A, C**). Additionally, a previously investigated CC A4B4 heterodimer (F_d = 2) [70, 131] was used as a reference system. In addition to the CC oligomerization state, also the number of PEG arms provides an additional design parameter. It introduces a second, but covalent-crosslink junction. While 4-arm star-PEG shows a functionality of 4 (F_c = 4), linear-PEG can be considered to possess 2 arms and thus a functionality of 2 (F_c = 2) (**Figure 18-B**). Using the combinations F_c:F_d = 2:4, 4:2 and 4:4, it was investigated if the thermodynamic properties of the crosslinks or their functionality are more important for controlling the bulk characteristics of the resulting hydrogels.

The bulk network properties were again studied with shear rheology. The linear viscoelastic properties were investigated using amplitude sweeps and frequency sweeps. Again, also stress relaxation tests were performed, using the same experimental procedures as described for the CMP-crosslinked hydrogels. Also the stiffness and yield stress of the networks were determined while applying a large continuous shear strain. These measurements in the non-linear rheological regime are analogous to the typical stress-strain curves obtained in conventional tensile tests, i.e. the stiffness and strength of the material can be obtained from the initial slope in the linear region and the maximum stress at rupture.

3) Can fluorescently labeled CMPs or CCs be designed to serve as molecular probes to monitor crosslink assembly state in the network?

Shear rheology is a simple but robust method to provide a variety of bulk material properties. Using the molecularly controlled approach described above, it also allows for establishing indirect correlations between the molecular crosslink parameters and the bulk viscoelastic properties; however, direct strategies to visualize the molecular state of individual crosslinks are urgently desired. In order to analyze association and dissociation events of CMP- or CC-crosslinks within the network, a fluorescence reporter system was tested in this work. The system is based on the FSQ effect of conventional fluorophores. 5(6)-carboxyfluorescein (CF) was coupled to the N-terminus of the CMPs and FSQ is expected to be present in the folded CTH (**Figure 19-A**) [146].
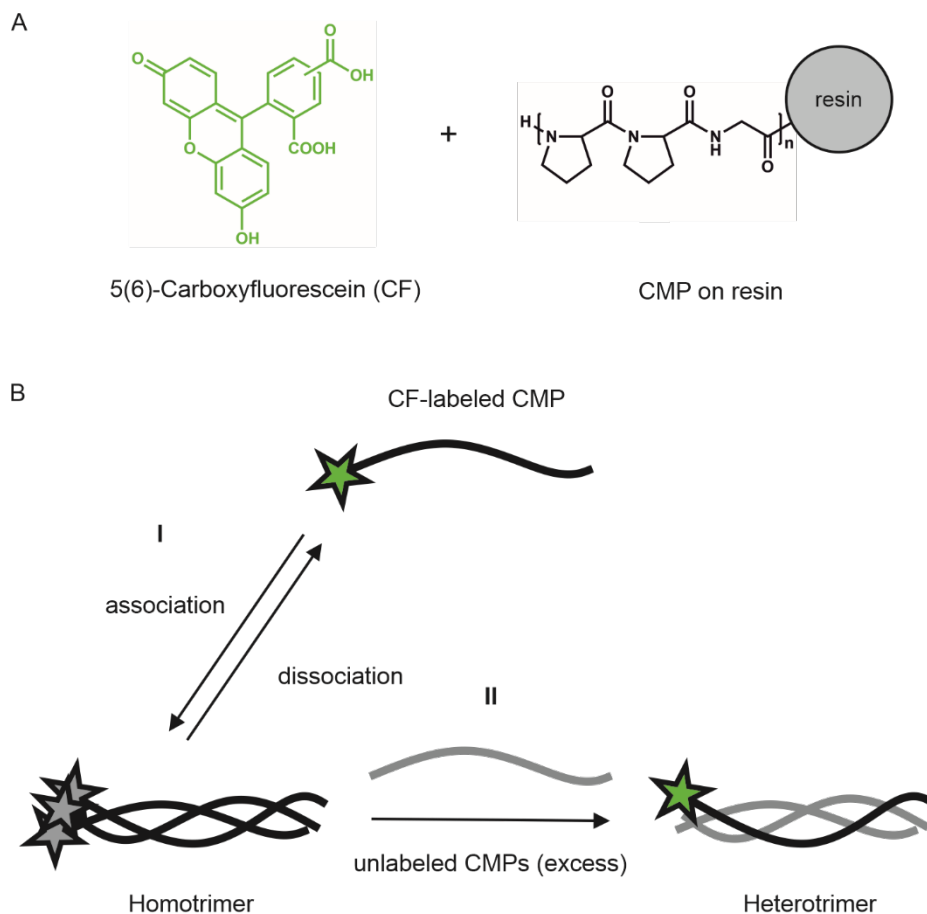
Figure 19. Fluorescence reporter system for monitoring folded or unfolded states of CMPs. A Synthesis and structure of the fluorescently labeled CMP. 5(6)-carboxyfluorescein (CF) molecules were coupled to the N-termini of the CMPs while the peptide chains were still on the resin. **B** The CF molecule (represented as green star), coupled to the CMP, shows fluorescence with the maximum emission at 524 nm. When the CF-labeled CMPs form a homotrimeric triple helical structure, the fluorescence intensity decreases due to the FSQ effect. The fluorescence can be recovered when the CF-labeled CMP homotrimers are dissociated (i.e. monomer state) (**I**). When an excess amount of the unlabeled CMP is added, the CF-labeled peptides can be exchanged with unlabeled peptides at equilibrium and form heterotrimers. The heterotrimeric state can show higher fluorescence intensity similar like the monomer state (**II**) [146].

First, I confirmed that the CF-CMPs synthesized in house indeed showed FSQ. The fluorescence was measured for the associated, folded CF-CMP and for the dissociated CMP, following thermal or chemical denaturation (**Figure 19-B, I**). As FSQ of CF-CMPs was expected to be used for measuring CMP dissociation, it was further tested if the FSQ reporter system allows for measuring the dissociation rates of CF-CMPs. If possible, this would provide a powerful strategy for following crosslink dissociation and re-association in the hydrogel network. Toward this goal, I used a competitive assay, adding unlabeled CMPs at room temperature. When adding unlabeled CMPs to an equilibrated solution of CF-CMPs, an exchange of labeled and unlabeled chains will gradually occur and an increase in the fluorescence intensity is expected (**Figure 19-B, II**). Similar experiments could be performed in the hydrogel network, using a mixture

of labeled and unlabeled crosslinks. The evolution of the fluorescence intensity would then provide information about dynamic processes in the network.

4.2 Aging effect and compressed exponential stress relaxation of the CMP-crosslinked hydrogels

The CMP-crosslinked hydrogels with a series of CMPs, $(PPG)_{10}$, $(POG)_7$, and $(POG)_{10}$, showed the viscoelastic properties from many rheological measurements. In the stress relaxation, they all exhibited aging behavior depending on the waiting time between the amplitude sweeps and the stress relaxation test in the standard measurement protocol. Particularly, the $(POG)_{10}$-crosslinked hydrogel displayed unique compressed exponential relaxation with short waiting time (10 min), whereas the other crosslinks did show the stretched exponential stress relaxation in the measurements at RT. The dissociation kinetics of the CMPs as peptide in solution were measured using CD spectroscopy based on the temperature-jump experiments and temperature-controlled hydrogel measurements were performed at the specific temperatures according to the kinetics measurements.

4.2.1 Thermodynamic and kinetic properties of the collagen mimetic peptides

The thermal stabilities of the three peptides used in this work are already well studied in previous researches [92, 99, 103], but the thermal transitions of the three peptides were confirmed in specific buffer condition again for the direct comparison with the hydrogel condition (i.e. borate buffer pH 8.9) (**Figure 20, Figure S3**).
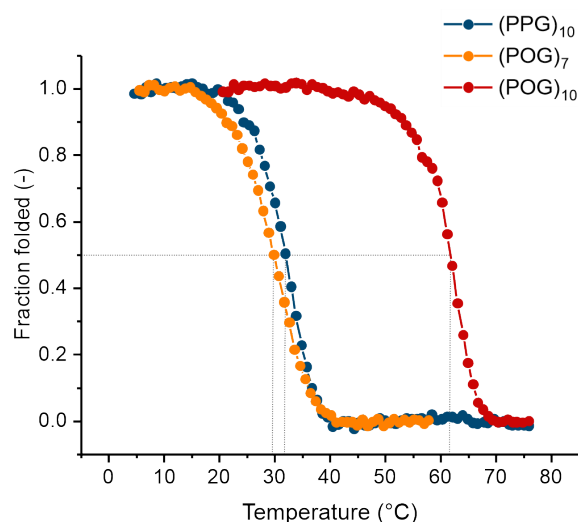
Figure 20. Fraction folded (F) curves and melting temperatures (T_m) of the CMPs obtained from thermal denaturation measurements using CD spectroscopy. Fraction folded curves were obtained from the thermal denaturation curves using CD spectroscopy. Detailed information about the thermal denaturation measurements was described in **Methods**. Melting temperatures of the CMPs were obtained by interpolation of the fraction folded curves at which the fraction folded is 0.5. The calculated values are shown in **Table 3**.

Table 3. Calculated parameters from the thermal denaturation measurements of the CMPs using CD spectroscopy. Melting temperatures of the CMPs were obtained from the fraction folded curves (**Figure 20**) at which the fraction folded 0.5. The fraction folded at 25 °C of each peptide was calculated by interpolating the fraction folded curves within the linear region. The temperatures at which the fraction folded values were about 0.99 were represented for showing the limit of the linear range before the transition started.

CMPs	Melting temperature, T_m (Fraction folded=0.5)	Fraction folded, f at 25 °C	Temperature with f=0.99
$(PPG)_{10}$	31.7 °C	0.89	20.6 °C
$(POG)_7$	29.7 °C	0.78	15.6 °C
$(POG)_{10}$	61.7 °C	1.00	44.2 °C

The $(POG)_{10}$ peptide has much higher thermodynamic stability (T_m~62 °C) than the $(POG)_7$ (T_m~30 °C), whereas the $(PPG)_{10}$ (T_m~32 °C) has similar melting temperature with $(POG)_7$ (**Table 3**). In addition to the stereoelectronic effect based on the Hyp group in the $(POG)_n$ sequence [92], the length of the peptide chains has an important role on the thermodynamic stability of the CMPs resulting from the number of the intermolecular interactions within the triple helical structure, for example $(POG)_{10}$ peptide has a higher T_m than $(POG)_7$ peptide. These T_m values that were measured using CD thermal denaturation measurements reasonably correspond to the values reported in the literatures (**Table S2**).

The fraction folded values around 25 °C were obtained from the fraction folded curves (**Figure 20, Table 3**) because 25 °C was the standard temperature for the hydrogel measurements. At 25 °C, $(PPG)_{10}$ peptide shows a fraction folded around 90 % in borate buffer (pH 8.9) and $(POG)_7$ peptide exhibits lower fraction folded below 80 %, whereas $(POG)_{10}$ peptide presents fully folded state (f = 1.0). The fraction folded values of $(PPG)_{10}$ and $(POG)_7$ are already in the transition region at 25 °C although $(POG)_{10}$ peptide stays in a fully folded stated. The temperature ranges in which each CMP has fully folded fraction (f > 0.99) were calculated in **Table 3**. These temperatures should be considered for the temperature-controlled hydrogel experiments with fully folded state of the CMP-crosslink.

Along with the thermal stabilities of the CMPs, dissociation kinetics of the CMPs was quantified using the CD temperature-jump dissociation kinetics experiments (**Figure 21, Table 4**). To observe clear transition from temperature-jump, the temperature range was chosen below the melting temperatures of each CMP. The apparent dissociation rates (k_{off}^{app}) of the three peptides were extracted from the initial slope of the plots of the fraction folded (in log scale) versus time (in linear scale) (**Figure S4**) from which the first-order reaction rates were obtained. All the apparent dissociation rates of the CMPs that were repeated 3 times of measurements and their average values were calculated in the **Table S3**. At 25 °C, the k_{off}^{app} of $(POG)_7$ was almost 4-folds faster than that of $(PPG)_{10}$, although they are in the same order of magnitude ($\sim 10^{-5}$ s^{-1}). On the other hand, $(POG)_{10}$ peptides showed the apparent dissociation rates of 7.32×10^{-8} s^{-1} at 25 °C, which is remarkably slower rates more than three orders of magnitudes compared to the other CMPs. Due to the high thermodynamic stability of $(POG)_{10}$ peptide, the apparent dissociation rate at 25 °C should be extrapolated from the Arrhenius plot in **Table 4**.

The similar trend was observed in the activation energies of the dissociation of the CMPs. Arrhenius plots of the dissociation rates in natural log scale versus the inverse temperatures used in CD temperature-jump experiments were plotted in **Figure 21**. The activation energies for the dissociation events were calculated from the slopes of Arrhenius plots for each peptide. The highest activation energy indicates the highest energy barrier for the dissociation of the triple helical structure such as $(POG)_{10}$ peptide. The $(POG)_7$ peptide has slightly lower activation energy than $(PPG)_{10}$ peptide that was similar trend in melting temperatures and the apparent dissociation rate of the CMPs, although the differences in the activation energies were smaller than the other properties. The overall trends in thermal and kinetic properties were clear. The $(POG)_7$ peptide had slightly lower melting temperature, faster dissociation kinetics and lower activation energy than $(PPG)_{10}$ peptides, while $(POG)_{10}$ peptide showed much higher thermodynamic stability and the slowest dissociation rates and the highest activation energy.
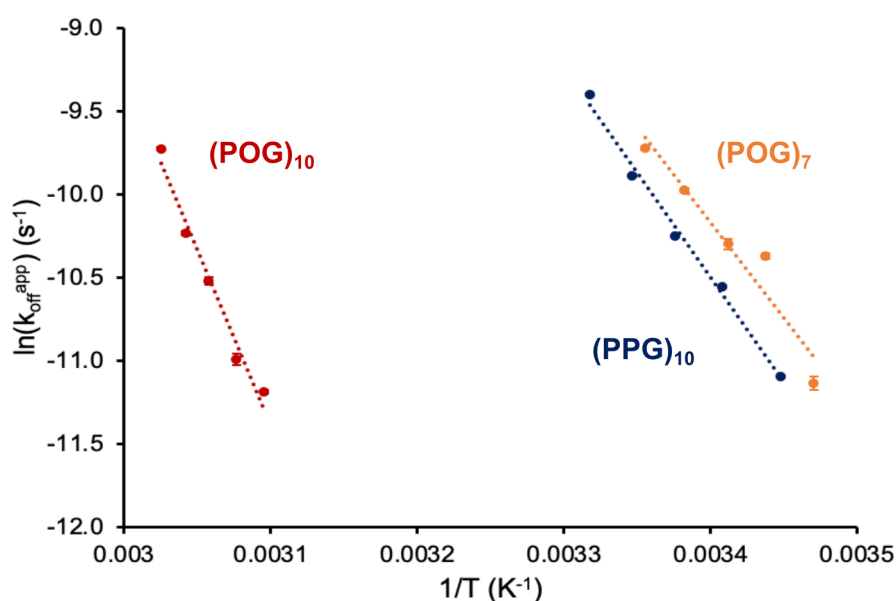
Figure 21. Arrhenius plots of the CMPs. Arrhenius plots with natural log of the apparent dissociation rates vs inversed temperatures for each CMPs were obtained from the CD temperature-jump experiments. Linear regression for each CMP was obtained and shown with dotted lines and the activation energies were calculated from the slopes of the linear regression. The measurements were repeated 3 times for each peptide and the apparent dissociation rates (**Table S3**) were obtained from the initial linear region in the dissociation dominant regions of the log(fraction folded) vs. lin(t) plots (**Figure S4**). The temperatures were not identical for each measurement, thus the average temperature of three measurements was used. Error bars were displayed for the standard errors of three individual k_{off}^{app} values from the different measurements, but the error was too small to be shown distinctively on the plots. The individual Arrhenius plots with the fitting parameters for each CMP were shown in **Figure S5**.

Table 4. Apparent dissociation rates and the activation energies of the CMPs. Apparent dissociation rates (k_{off}^{app}) were extrapolated or interpolated from the Arrhenius plots of the CMPs (**Figure 21, Figure S5**). The activation energies (E_a) of the CMPs were obtained from the slopes of the Arrhenius plots.

CMPs	k_{off}^{app} (s^{-1}) at 25 °C	E_a (kJ mol^{-1})
(PPG)$_{10}$	3.87 x 10^{-5}	104.4
(POG)$_7$	5.49 x 10^{-5}	94.7
(POG)$_{10}$	7.32 x 10^{-8}	173.8

4.2.2 Viscoelastic properties of the CMP-crosslinked hydrogels

The triple helical structure of the CMPs is served as a transient crosslink in 4-arm star-PEG network providing viscoelastic properties to the network via dissociation/re-association of the

CTHs. Conventional rheology was performed to understand the bulk materials properties of the hydrogels through applying shear deformation.

In order to identify the linear viscoelastic (LVE) region of the hydrogels under the shear deformations, amplitude sweeps were performed with oscillatory strain amplitudes in a range of 0.1-1000 % (**Figure 22-A**). Collagen-inspired hydrogels show the LVE region until around 30 to 200 % of the strain when the limit of the linear viscoelastic range can be determined from the end point of the plateau of the storage modulus. The individual values from different sample batches have a small variation but in general the $(PPG)_{10}$ hydrogels exhibit shorter linear viscoelastic range than the $(POG)_7$ and $(POG)_{10}$ hydrogels. Through the crossover points of the storage and loss moduli in the AS, the materials can be estimated whether they response as more solid-like or liquid-like under the given shear strain amplitude. The collagen-inspired hydrogels showed the crossover points around 50 to 300 % that is relatively the similar range of difference compared to the LVE region discussed above.

The stiffness of the materials can be estimated from the plateau modulus (G_p) that is defined as the average storage modulus in the LVE region. The G_p of the $(PPG)_{10}$ and $(POG)_{10}$ hydrogels were around 1000~3000 Pa when the $(POG)_7$ hydrogels showed lower stiffness with G_p of 800-900 Pa in their representative AS curves. In principle, it is known that the plateau modulus depends on the crosslink density in the network [187]. Low G_p value of $(POG)_7$-crosslinked hydrogels might be related to the fraction folded (~ 78 %) of $(POG)_7$ peptide at 25 °C. Due to the low thermodynamic stability, the $(POG)_7$ crosslink has lower fraction folded in the network which can directly affect to the elastically active crosslink density at certain temperature near or higher than melting temperature (T_m of $(POG)_7$ ~ 30 °C). However, the high G_p of the $(PPG)_{10}$ hydrogels cannot be matched with this explanation. Hydrogel preparation can also contribute the variation of the viscoelastic parameters. Depending on the sample batches, the G_p, LVE region, flow point (crossover of G' and G") showed relatively large variation (**Table S4**).

The plateau modulus also can be measured by the frequency sweep tests (**Figure 22-B**). Except slight increases near the highest frequency of the measurement range, G' of all hydrogels show the stable plateau values through the overall frequency range, being consistent with the G_p values obtained from the amplitude sweeps in the linear viscoelastic range. In order to investigate the relaxation times of the networks, the crossover frequency (ω_c) at which the G' has the same value with G" in low frequency regime can be used for the calculation as the inverse of the relaxation times (τ_{FS}). Due to the extremely slow kinetics of the collagen molecules, however, the crossover points couldn't be measured in the measurable range in the frequency sweep test. At frequency lower than 0.005 rad s^{-1}, the

measurement time became too long so that the gels dried during the measurement showing weird noises for both G' and G'' in the current rheometer setup.
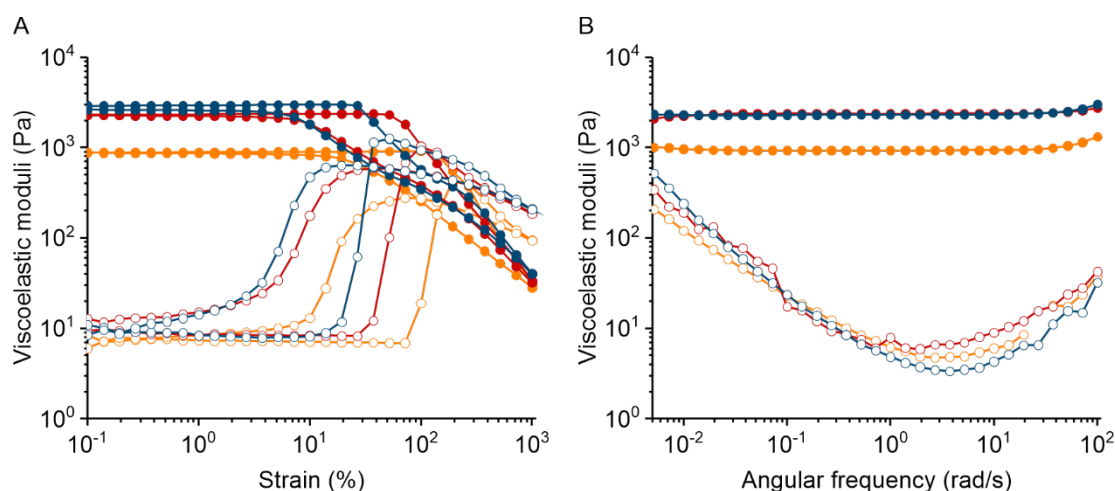
Figure 22. Viscoelastic properties of the CMP-crosslinked hydrogels. A Representative amplitude sweeps (storage modulus G': solid lines, filled dots / loss modulus G'': solid lines, empty dots) of the $(POG)_7$-crosslinked hydrogel (orange), the $(POG)_{10}$-crosslinked hydrogel (dark red), and the $(PPG)_{10}$-crosslinked hydrogel (dark blue) measured with oscillatory shear rheometer. Strain amplitudes were varied from 0.1 % to 1000 % with a constant angular frequency of 10 rad s^{-1}. The descending strain amplitude sweep from 1000 % to 0.1 % was also performed. **B** Representative frequency sweeps of the CMP-crosslinked hydrogels. Oscillatory frequency was varied from 100 rad s^{-1} to 0.005 rad s^{-1} with a constant strain amplitude of 1 % were performed.

The collagen triple helix employed as the dynamic crosslink of the networks can be re-associated again after it is broken with any external stimuli (e.g. force, deformation, temperature, pH) through the self-assembly of the CTHs, therefore, the hydrogels based on the collagen triple helical crosslinks show the self-healing behaviors after they are ruptured with large deformations (or load). The repetitive recovery of the gel elasticity from several cycles of breaking are shown in **Figure 23**. The $(POG)_7$ and $(POG)_{10}$ hydrogels exhibit relatively faster G' recovery after coming back to the small strain (0.1 %) from large oscillatory deformations with 1000 % than the $(PPG)_{10}$ hydrogels. Due to the additional hydroxyl group at pyrrolidine ring of hydroxyproline, the $(POG)_n$ sequence-based peptides are preorganized in polyproline II helices, which enhances the formation of the triple helical structure [91, 92]. In the previous work of S. Boudko and J. Engel, the $(POG)_{10}$ peptide shows 1000-fold higher re-association rates than the $(PPG)_{10}$ peptide with the stabilizing effect of 4-hydroxyproine in the peptide sequence [93]. The recovery of the elasticity of the collagen-inspired hydrogels are not simply dominated by the re-association of the CMP triple helix, but more complex network behaivor. However, faster re-association rates of the $(POG)_n$ peptides seem to be a

main reason of the faster recovery of material stiffness (represented by the storage modulus, G') in the (POG)$_7$ and (POG)$_{10}$ crosslinked hydrogels.
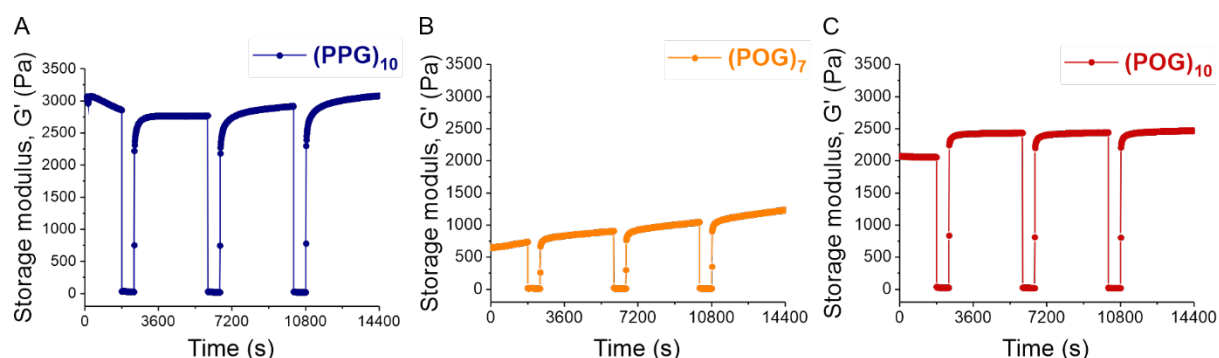
Figure 23. Representative self-healing tests of the CMP-crosslinked hydrogels. The measurements were performed based on the step-strain methods using oscillatory shear rheometer. Oscillatory strain amplitude of 0.1 % was applied for 1800 s to obtain the initial plateau modulus. Large oscillatory strain amplitude of 1000 % was applied for 600 s to break the crosslinks mechanically followed by small oscillatory stain amplitude of 0.1 % was applied for 3600 s to observe the self-healing behavior of the transient crosslinks. The breaking-recovery cycle was repeated 3 times. Only storage moduli (G') of the (PPG)$_{10}$- (**A**, dark blue), (POG)$_7$- (**B**, orange), and (POG)$_{10}$- (**C**, dark red) based hydrogels were plotted over time.

4.2.3   Stress relaxation of the CMP-crosslinked hydrogels: Effect of pre-stress and aging

Investigation of the characteristic relaxation time of the CMP-crosslinked hydrogels with frequency sweep tests was restricted by the intrinsic slow kinetics of the CMPs. Stress relaxation tests were performed to investigate the stress relaxation behavior of the hydrogels with shorter measurement time than that of FS.

From the standard measurement protocol for the stress relaxation test (**Figure 24-A**), an AS with ascending strain range of 0.1 - 1000 % were performed. The rejuvenation effect was expected to reset the mechanical history of the materials before performing the stress relaxation test. The material behaviors from AS were similar with those in **Figure 22** but only ascending strain sweep was performed without descending strain sweep in the standard procedure of the stress relaxation tests. However, from the large mechanical perturbation by AS (~ 1000 %), pre-stress was imposed to the hydrogels, which was relaxed slowly staying within the network for certain time, which was the opposite result from the estimation with the rejuvenation effect (**Figure 24-B, C, D**). The internal stress was monitored during the waiting time at zero strain. In general, the pre-stress applied during the amplitude sweeps to the (POG)$_7$ and (PPG)$_{10}$ hydrogels started to decrease immediately and almost fully relaxed within

66

3600 s (60 min) at zero strain. On the other hand, the (POG)$_{10}$ hydrogels did not relax the pre-stress immediately at the beginning but held the stress longer, showing the plateau, then started to relax with the time scale from 300 s to 1800 s. The pre-stresses of the (POG)$_{10}$ hydrogels were not fully relaxed within the longest waiting time: Even after 60 min of waiting time, the (POG)$_{10}$ hydrogels released only about 12 % of the initial stress.
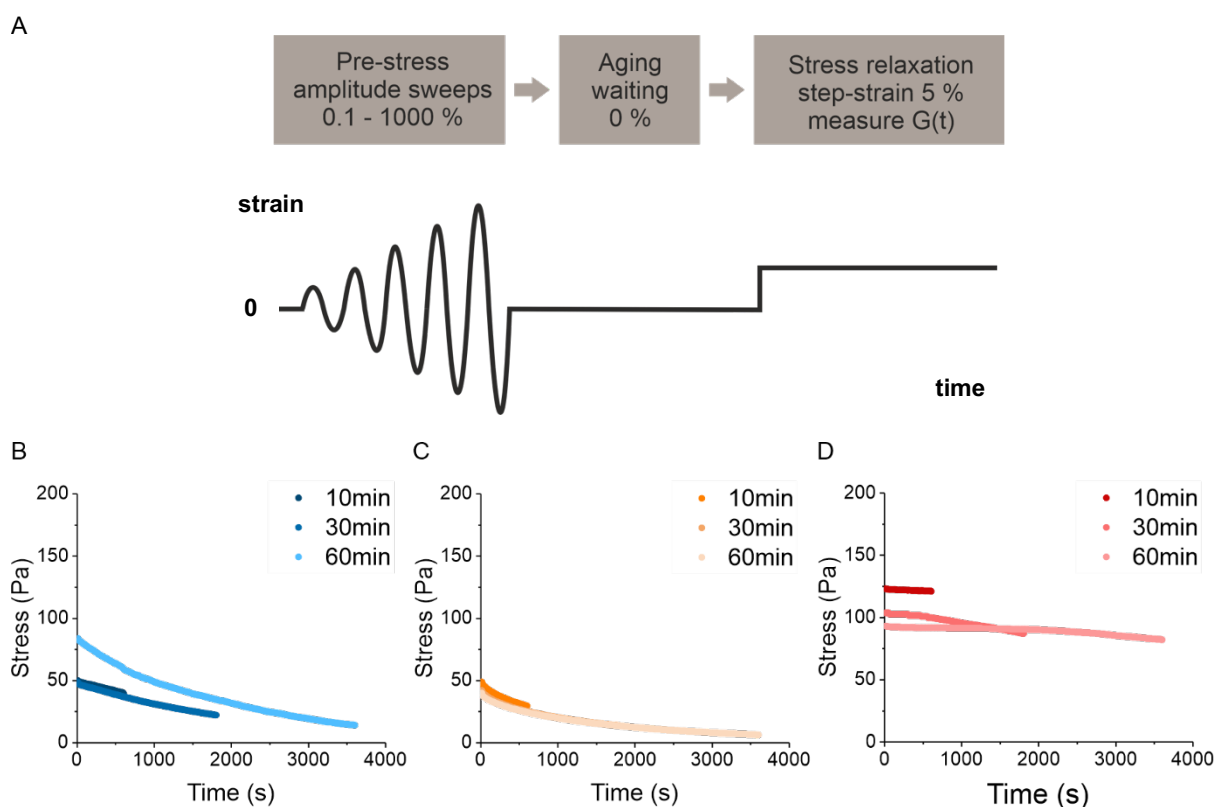
Figure 24. Relaxation of the applied stress during the waiting time of the stress relaxation test. A Experimental protocol of the stress relaxation test with zero-strain waiting method. Amplitude sweeps only with ascending strain amplitudes from 0.1 % to 1000 % at a constant angular frequency of 10 rad s^{-1} were performed to confirm the viscoelastic behavior of the CMPs. Pre-stresses were applied to the network from the mechanical perturbation during the amplitude sweeps. The samples were at rest where the strain was set to 0 % (zero-strain method) during the waiting time. For the actual stress relaxation test, the strain of 5 % was applied once in a stepwise manner and the relaxation modulus was monitored over time. The relaxation of the stress, which was applied during the amplitude sweeps for (PPG)$_{10}$- (**B**, blue), (POG)$_7$- (**C**, orange), and (POG)$_{10}$- (**D**, red) crosslinked hydrogels, were monitored during the waiting time (i.e. after the amplitude sweeps finished and before the stress relaxation test started).

After certain waiting time, an additional strain of 5 % was applied in a stepwise manner to the hydrogels for observing the relaxation of the applied stress. Due to the dynamic characteristic of the CMP-crosslinks, the network can relax the stress with dissociation of the crosslink. The relaxation parameters such as the relaxation times (τ) and relaxation exponents (α) were obtained through the fitting with KWW equation (See **Methods**). The (POG)$_{10}$-crosslinked

hydrogels have significantly longer relaxation times about an order of magnitude than those of the other CMP-crosslinked networks with all sample ages (**Figure 25, Table 5**), whereas the (POG)$_7$- and (PPG)$_{10}$- crosslinked hydrogels have the relaxation times within almost the same range of time scale. Also, the (POG)$_7$- and (PPG)$_{10}$-crosslinked hydrogels showed the relaxation exponents with a range roughly around from 0.7 to 0.9, which are stretched exponential stress relaxation (when α is between 0 to 1) that is well known for the usual behavior of many soft materials including soft biological tissues [6, 188]. However, very interestingly, the (POG)$_{10}$-crosslinked hydrogel showed the relaxation exponents higher than 1 with short waiting time of 10 min, which is uncommon relaxation behavior known as compressed exponential relaxation. This uncommon phenomenon has been observed in a few soft glassy materials such as colloidal fractal gels, concentrated emulsions and lamellar gels [30]. Most of the soft glassy materials exhibit the effect of pre-stress and the aging process in many scattering experiments. However, the origin of the compressed exponential relaxation and the physical description of this phenomenon has still poorly understood.

The relaxation behaviors of all CMP-crosslinked hydrogels showed an identical trend particularly in the relaxation exponents depending on the waiting times regardless of compressed or stretched exponential relaxation. This aging process after applying the pre-stress seem to have a huge effect on the relaxation behavior of the material. In all hydrogel systems, the relaxation times and fitting parameters show the decreasing trends with the sample ages. Even the (POG)$_{10}$-crosslinked hydrogels that showed compressed exponential relaxation with $\alpha > 1$ with the waiting time of 10 min, showed a transition from compressed exponential to stretched exponential stress relaxation with α around 0.8. The α with waiting time of 30 min is slightly lower than that of waiting time of 60 min that is not exactly matched with the general trend of α, however, from comparison with the value of 10 min waiting time, the overall trend from 5 repeats of stress relaxation tests of the (POG)$_{10}$-crosslinked hydrogels with individual batch of the hydrogels seems to be a decrease of the relaxation exponents with increasing the waiting times (**Figure S6, Table S5**).
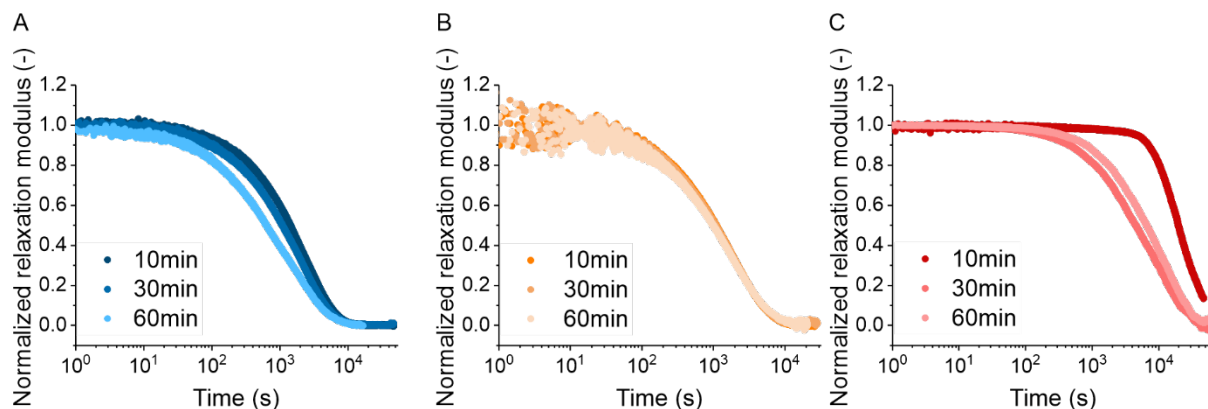
Figure 25. Representative stress relaxation curves of the CMP-crosslinked hydrogels. The relaxation curves of the (PPG)$_{10}$- (**A**, blue), the (POG)$_7$- (**B**, orange), and the (POG)$_{10}$- (**C**, red) crosslinked hydrogels were shown. The relaxation times and the relaxation exponents were obtained with fitting using the KWW equation (see **Methods**), and the parameters were shown in **Tables 5**. As the standard protocol, the amplitude sweeps with a strain amplitude range from 0.1 % to 1000 % was used. After waiting time (**Figure 24**), the step-strain based (5 %) stress relaxation tests were performed for each CMP-crosslinked hydrogel. The measurements were performed with different waiting times of 10, 30, and 60 min with the same batch of the hydrogels at 25 °C.

Table 5. Relaxation parameters obtained from the representative stress relaxation curves of the CMP-crosslinked hydrogels (Figure 25). Relaxation times (τ) and relaxation exponents (α) were obtained using the KWW equation.

CMPs	Relaxation parameters	Sample age (waiting time)		
		10 min	30 min	60 min
(PPG)$_{10}$	Relaxation time, τ	2138	1713	1127
	Relaxation exponent, α	0.87	0.79	0.67
(POG)$_7$	Relaxation time, τ	1719	1694	1629
	Relaxation exponent, α	0.80	0.77	0.73
(POG)$_{10}$	Relaxation time, τ	26379	7281	10012
	Relaxation exponent, α	1.55	0.78	0.85

On the other hand, the relaxation times also showed a decreasing trend with increasing the sample ages in all CMP-crosslinked hydrogels. However, this trend is controversial because the different waiting times should be considered for the relaxation times. Depending on the adding of the waiting time, the trend might be seen like the opposite way, but also the relatively large variation of the relaxation parameters (**Table S5**) depending on the sample baches or the mechanical history of the samples should be carefully considered for further discussion.

4.2.4   Stress relaxations under the controlled dissociation kinetics

For the stress relaxation tests of the CMP-crosslinked hydrogels performed at 25 ˚C, the apparent dissociation rates and the fraction folded of the CMPs were different depending on the thermodynamic and kinetic properties of the CMPs. To understand the origin and the molecular mechanism of the stress relaxation behavior of the CMP-crosslinked hydrogels, the stress relaxation tests were performed at controlled temperatures at which the fraction folded, and the dissociation rates of each CMP are controlled systematically.

The temperatures at which the CMPs have the same fraction folded values as ~0.99 were obtained from the CD thermal denaturation curves (**Figure 20, Table 3**). The end point of the plateau before starting the thermal transition were chosen for the temperature-controlled stress relaxation tests with the same fraction folded of the CMP-crosslinks (**Figure S7**). The general trend in the relaxation times and the relaxation exponents depending on the waiting times have not changed, but it showed the increased values in both parameters (i.e. longer relaxation times and higher exponents) in the $(PPG)_{10}$- and $(POG)_7$-crosslinked hydrogels compared to the values at 25 °C, whereas the $(POG)_{10}$-crosslinked hydrogels showed the opposite trend due to the higher measurement temperature. At 47 °C, the relaxation times of the $(POG)_{10}$-crosslinked hydrogels decreased around an order of magnitude than those at 25 °C and even lower than the relaxation times of the $(POG)_7$ and $(PPG)_{10}$ at 15 ˚C and 20 ˚C, respectively. It seems like the measurement temperature was too high for the stress relaxation test with relatively long measurement time (~ 10 h) because the samples might get dried and thus it causes lower accuracy on the fitting. However, the large changes in relaxation times and the exponents of the $(POG)_{10}$-crosslinked hydrogels at the fraction folded of 0.99 might mean that there is more critical factor that determines the stress relaxation behavior of the CMP-crosslinked hydrogels because the fraction folded of the (POG) at 25 °C (f = 1.00) and at 47 °C (f = 0.99) were almost identical and thus the difference in the relaxation parameters should not be largely affected by the fraction folded in principle. On the other hand, the dissociation rates of the CMP are also strongly affected by the temperature, which might have more critical effect on the relaxation behavior of the CMP-crosslinked hydrogels.

Interestingly, the $(PPG)_{10}$-crosslinked hydrogels reached to the compressed exponential region with the waiting time of 10 min. Higher fraction folded contributes to increase the number of elastically active crosslinking in the $(PPG)_{10}$-crosslinked hydrogels; however, same like the $(POG)_{10}$ case, the fraction folded cannot be the main reason for the transition to the compressed exponential stress relaxation of $(PPG)_{10}$ system because the $(POG)_7$-crosslinked hydrogels also increased in fraction folded (f = 0.99 at 15 °C) but it did not show the clear

transition to the compressed exponential region, although both the relaxation times and exponents increased at lower temperature. It seems obvious that the dissociation kinetics of the CMPs plays more important role in the relaxation behaviors of the networks rather than the fraction folded itself.

For further investigation on the effect of the dissociation kinetics of the CMPs on the relaxation behavior of the CMP-crosslinked hydrogels, the lower measurement temperature was tested (**Figure 26**). Through reducing the measurement temperature to 5 °C, the both $(PPG)_{10}$- and $(POG)_7$-crosslinked hydrogels exhibited the increased relaxation times than those at 25 °C about 3- or 4-folds longer, but also the relaxation of the pre-stress during the waiting times also became slower compared to those at 25 °C (**Figure S8**). Interestingly, both hydrogels reached to the compressed exponential region with waiting time of 10 min and the relaxation times increased. The fraction folded did not changed largely from 20 °C to 5 °C ($f = 0.99\sim1.00$), but the dissociation rates of the CMPs became lower at 5 °C, which played more important role for showing the compressed exponential stress relaxation with short sample ages. From the Arrhenius plots that obtained from the CD temperature-jump experiments (**Figure 21, Table 4**), the apparent dissociation rates of each CMP were extrapolated and shown together with the stress relaxation curves (**Figure 26, Table 6**). The apparent dissociation rates (k_{off}^{app}) of the $(PPG)_{10}$ and $(POG)_7$ at 5 °C become an order of magnitude slower than those at 25 °C. These rates are still faster than that of $(POG)_{10}$ at 25 °C about two orders of magnitudes but the dissociation kinetics was slow enough to reach to the compressed exponential region with α = 1.32 for $(PPG)_{10}$ and 1.19 for $(POG)_7$ when the waiting time was 10 min. These compressed exponents were shifted to the stretched exponents to 0.87 and 0.91 with increasing the waiting time (i.e. 60 min) in $(PPG)_{10}$- and $(POG)_7$-crosslinked hydrogel, respectively, which was the same behavior that the $(POG)_{10}$-crosslinked hydrogel showed at 25 °C. Also, the relaxation exponents of the $(POG)_{10}$-crosslinked hydrogels at 5 °C increased and even after 60 min waiting time, the α value stayed in the compressed region.
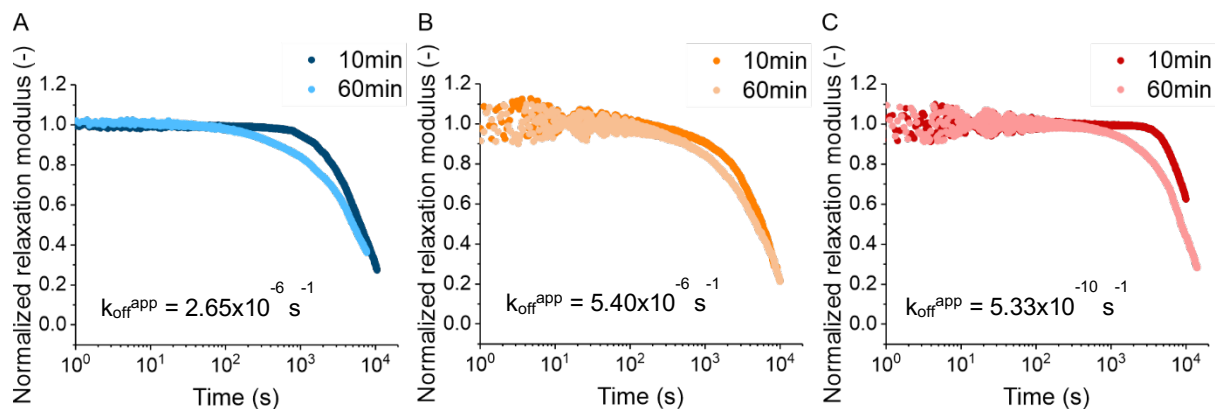
Figure 26. Stress relaxation tests of the CMP-crosslinked hydrogels measured at 5 °C. The standard protocol was used with zero-strain waiting time. The (PPG)$_{10}$- (**A**, blue), the (POG)$_7$- (**B**, orange) and the (POG)$_{10}$-crosslinked hydrogels (**C**, red) were measured at 5 °C to slow down the dissociation rates. Apparent dissociation rates at each temperature were calculated from the Arrhenius plots obtained from the CD T-jump dissociation kinetics experiments through interpolation or extrapolation depending (**Figure 21**). The relaxation times and the relaxation exponents were obtained using the KWW equation (**Table 6**).

Table 6. Relaxation parameters obtained from the temperature-controlled stress relaxation tests of the CMP-controlled hydrogels (Figure 26) measured at 5 °C. Relaxation times (τ) and relaxation exponents (α) were obtained using the KWW equation.

CMPs	Relaxation parameters	Sample age (waiting time)	
		10 min	**60 min**
(PPG)$_{10}$	Relaxation time, τ	8432	7705
	Relaxation exponent, α	1.32	0.87
(POG)$_7$	Relaxation time, τ	7636	7087
	Relaxation exponent, α	1.19	0.91
(POG)$_{10}$	Relaxation time, τ	15483	11793
	Relaxation exponent, α	1.92	1.29

After the pre-stress is imposed to the network, the aging behavior are highly affected to this dissociation kinetics of the CMP crosslinks. For all the CMP crosslinks, the slow dissociation rates at low temperature leaded to increase of the relaxation times and exponents both due to the slow kinetics of the crosslink dissociation, which is directly related to the relaxation of the stress imposed within the network and the unique compressed exponential stress relaxation seems to occur with the slow dynamics of the crosslink and the short sample aging in which the pre-stress does not start to be relaxed (i.e. frozen state) or only partially relaxed.

4.2.5 Other strategies for applying pre-stress and way of waiting time

As standard protocol for the stress relaxation test, the amplitude sweeps and waiting time at zero-strain (γ = 0 %, i.e. the initial starting point) have been employed. The initial idea was to reset the mechanical history of the materials with applying controlled pre-stress before the stress relaxation measurement; however, due to the intrinsic slow kinetics of the CMPs, the AS was considered as mechanical perturbation and the waiting time was also controlled to observe the aging behavior. Therefore, it was worth to try the other strategies for applying the pre-stress and the way of aging to confirm the generality of the stress relaxation behavior of the CMP-crosslinked hydrogels with different experimental protocols.

Firstly, the preset of the rheometer during the waiting times was replaced from zero-strain to zero-stress protocol as described in **Figure 27-A** and **Table 7**. To make the material feel zero-stress (σ = 0 Pa) during the waiting time, additional strain should be applied, but the direction and magnitude of the strain applied were arbitrary depending on the sample history. Although the additional strain was applied for zero-stress waiting strategy, the relaxation properties of the CMP-crosslinked hydrogels were similar with those of zero-strain protocol. The relaxation times were in the same time scale ($\sim 10^4$ s) and decreased with increasing the waiting time while the relaxation exponents were slightly higher staying in compressed region with longer waiting time (i.e. 30 min of sample aging).

Second, a large amplitude of step-strain (1000 %) was applied to the CMP-crosslinked hydrogels for the mechanical perturbation instead of amplitude sweeps in previous protocol (**Figure 27-B, Table 7**). The relaxation times were in the same time scale of 10^4 s and decreased with increasing waiting time like the protocol with AS. Surprisingly, the fitting parameters could be larger than 2, although the boundary of α value for compressed exponential relaxation is generally defined between 1 and 2 ($1 < \alpha \leq 2$). The α was decreased with increasing the waiting time but the value still remained in the compressed exponential region even with the waiting time of 60 min. The explanation for the extremely high compressed exponents is still missing in the scope of this work; however, the overall trend in the evolution of the relaxation parameters in the step-strain-based mechanical perturbation protocol might be considered as similar behavior with those of the standard protocol with AS.
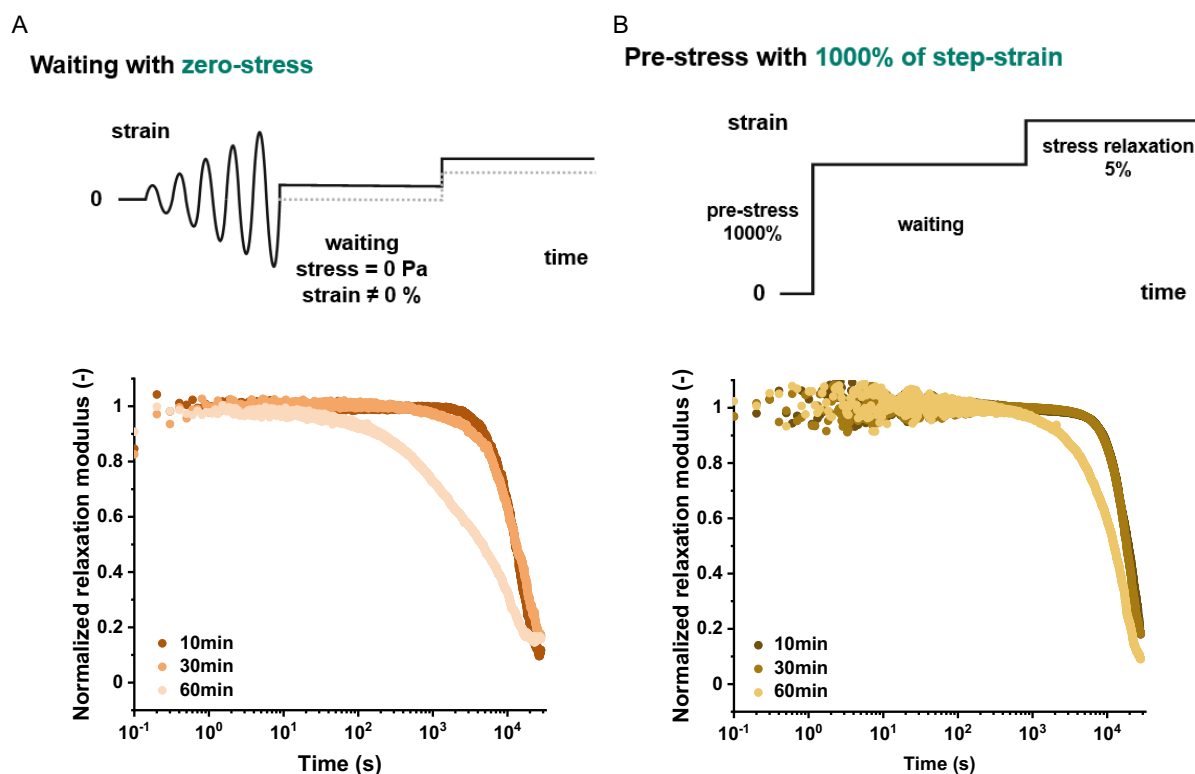
Figure 27. Stress relaxation tests of the (POG)$_{10}$-crosslinked hydrogels with different waiting time and pre-stress strategies. A The tress relaxation tests using the measurement protocol with zero-stress waiting method. After AS, an additional strain should be applied to set the stress as 0 Pa during the waiting time. For the following stress relaxation test, additional 5 % strain was applied on the top of the previous strain applied for the zero-stress waiting time. **B** The stress relaxation test using step-strain-based method for applying the pre-stress. A strain of 1000 % was applied once in a stepwise manner instead of performing the amplitude sweeps while the stresses were recorded during the waiting time. For the following stress relaxation test, additional strain of 5 % was applied on the top of the applied strain of 1000 %. The measurement temperature was 25 °C and the relaxation parameters were obtained with using KWW equation (**Table 7**).

Table 7. Relaxation parameters obtained from the stress relaxation tests of the (POG)$_{10}$-crosslinked hydrogels (Figure 27) with the zero-stress waiting time protocol and the step-strain pre-stress protocol. Relaxation times (τ) and relaxation exponents (α) were obtained using the KWW equation.

Methods	Relaxation parameters	Sample age (waiting time)		
		10 min	**30 min**	**60 min**
Waiting with zero-stress	Relaxation time, τ	15854	17529	7865
	Relaxation exponent, α	1.86	1.40	0.59
Pre-stress with 1000 % step-strain	Relaxation time, τ	22572	21518	15438
	Relaxation exponent, α	2.29	2.39	1.32

4.3 The effect of crosslinking functionality on the material properties of the CC-crosslinked hydrogels

Using CC-forming peptides (**Figure 18**) with the different oligomerization states (e.g. homodimer, homotrimer, and homotetramer) as the physical crosslinks in the PEG-based polymeric hydrogel network can be a decent strategy to study the correlation between the crosslinking functionality and the resulting network properties. Particularly, the CC homotrimer can be a reference system for the CTHs used in the previous chapters for the trivalent crosslink nature as well as the similar thermodynamic properties (i.e. T_m). For the other crosslink geometries, CC homodimer gives simpler physical crosslinking junction, whereas CC homotetramer is expected to form more complex structure in the star-PEG network. Therefore, the connectivity of the network particularly around the crosslinking points is determined in principle with the crosslinking functionality based on the oligomerization states of the CC peptides.

4-arm star-PEG polymer can be also considered as a crosslinking junction not as a physical interaction but as a covalently linkage at the molecular center of the PEG. as described in the **Experimental design** (**Figure 18**). With CC-homo4 as a physical crosslink, 4-arm star-PEG and linear PEG (i.e. 2-arm PEG) were employed to study the effect of the covalent crosslink-functionality associated with the molecular geometry of the PEG on the viscoelastic behavior of the resulting hydrogels.

The purification results through preparative HPLC and MALDI-TOF spectra of the CC peptides synthesized using the SPPS were presented in the appendix (**Figure S1**).

4.3.1 Thermodynamic stability of the CC-forming peptides

To confirm the secondary structures as well as the melting temperature of the chemically synthesized CC-forming peptides, CD spectra were obtained in specific buffer condition. The peptides stored in 4 °C more than 48 h are expected to be fully associated with stable CC superhelical structures. CD spectra of the coiled coil peptides have distinctive minima at the wavelengths of 208 nm and 222 nm, which are associated with α-helical structure. Particularly, the ratio of two minima ($ME_{222/208}$) is usually used to confirm the stability of the α helical structure when the ratio is close to or higher than 1 (**Figure 28-A**). The synthesized CC peptides showed stable α helical structure with $ME_{222/208}$ values higher than or close to 1. The

intensities at ME_{222} were also used for the intensity of the fully associated state (θ_F) before the thermal denaturation measurements. The thermodynamic stabilities of three CC peptides were shown with the thermal denaturation curves (**Figure 28-B**). CD signal at a wavelength of 222 nm were monitored when the temperature increased from 4 °C to above 90 °C. CC Homo2 and homo3 showed the clear transition curves at around 68 °C and 53 °C, respectively. The values were obtained from the maximum points of the first derivative of each thermal denaturation curves (**Figure S9**), while the CC-Homo4 did not show a full transition curve in the temperature range used in CD measurement. It refers that the melting temperature of CC-Homo4 is higher than the temperature range of CD thermal denaturation measurement ($T_m >$ 90 °C). The melting temperatures of CC-Homo2 and CC-Homo3 were obtained from the first derivative method showed the similar T_m values with those obtained from Global 3 software fitting based on the double baseline correction **(Figure S9, Table S6, see Methods)**. These measured melting temperatures of the CC peptides were lower than the those from the literatures about 3-10 °C [85]. The N- and C-terminal modifications (i.e. additional glycine spacer, cysteine residue at N-terminal and removal of tyrosine residue from C-terminal compared to the sequences from the literature) might affect the thermodynamic stability of the peptides.
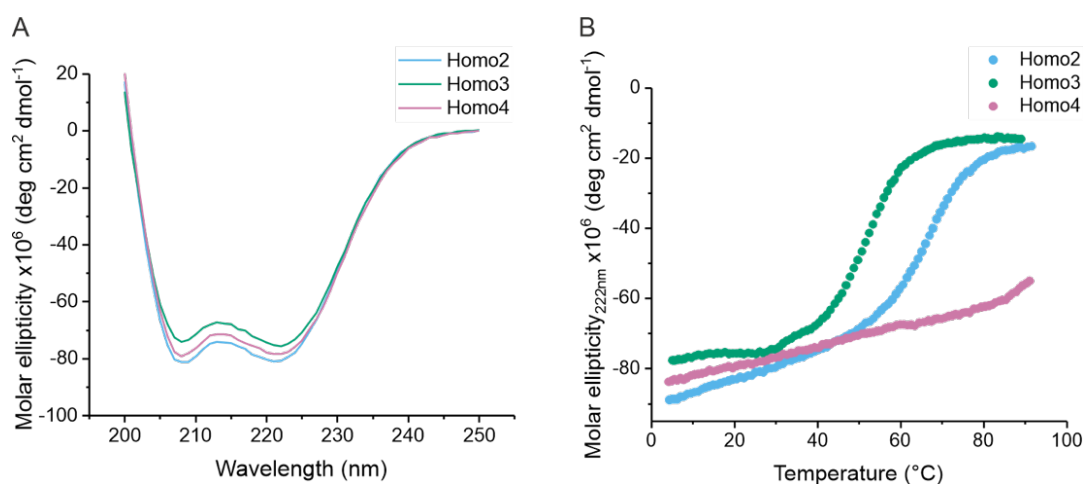
Figure 28. CD spectra (A) and thermal denaturation curves (B) of the CC homopeptides. A CC homodimer (Homo2: sky blue), homotrimer (Homo3: bluish green), and homotetramer (Homo4: reddish pink) were measured at 4 °C at which all CC peptides formed the stable α-helical structures in principle. It was confirmed with the ratio of $ME_{222/208}$ with 1.04, 1.06, and 1.04 for CC-Homo2, CC-Homo3, and CC-Homo4, respectively. All the CC peptides were prepared in PBS or coupling buffers for the CD measurements in a presence of TCEP (10 times excess). **B** Thermal denaturation curves of the CC peptides. Temperature range was 4-90 °C and the rate of heating was 1 °C/min with a step of 1 °C for the thermal denaturation. The melting temperatures were obtained by reading the maximum point of the first derivative of each thermal denaturation curve (**Figure S9**).

4.3.2 The Effect of the dynamic crosslink functionality on the mechanical properties of the CC-crosslinked hydrogels

Various mechanical properties of the CC-crosslinked hydrogels were investigated with using a shear rheology. Amplitude sweeps gave useful information about the linear and non-linear behavior of the material with the response to the certain range of the oscillatory shear deformation (**Figure 29**). The CC Hetero2- and Homo2-crosslinked hydrogels exhibited the similar strain limits for the LVE region (about 200 %), while Homo3- and Homo4-crosslinked hydrogels have shorter LVE region like 70 % and 20 %, respectively. The strain values at flow point (i.e. crossover of G' and G") also showed the decreasing trend with the higher oligomerization states of the CC peptides. The plateau modulus ($G_{p,AS}$) can be averaged from the storage moduli in the LVE region. CC Homo2- and Homo3-crosslinked hydrogels have the $G_{p,AS}$ around 1000~2000 Pa, whereas Homo4-crosslinked hydrogels show higher plateau moduli like 4000~5000 Pa. The overall trend in the viscoelastic properties from AS measurements were that the LVE regions and flow points were reduced and $G_{p,AS}$ values increased with increasing the oligomerization states of the CC peptides.
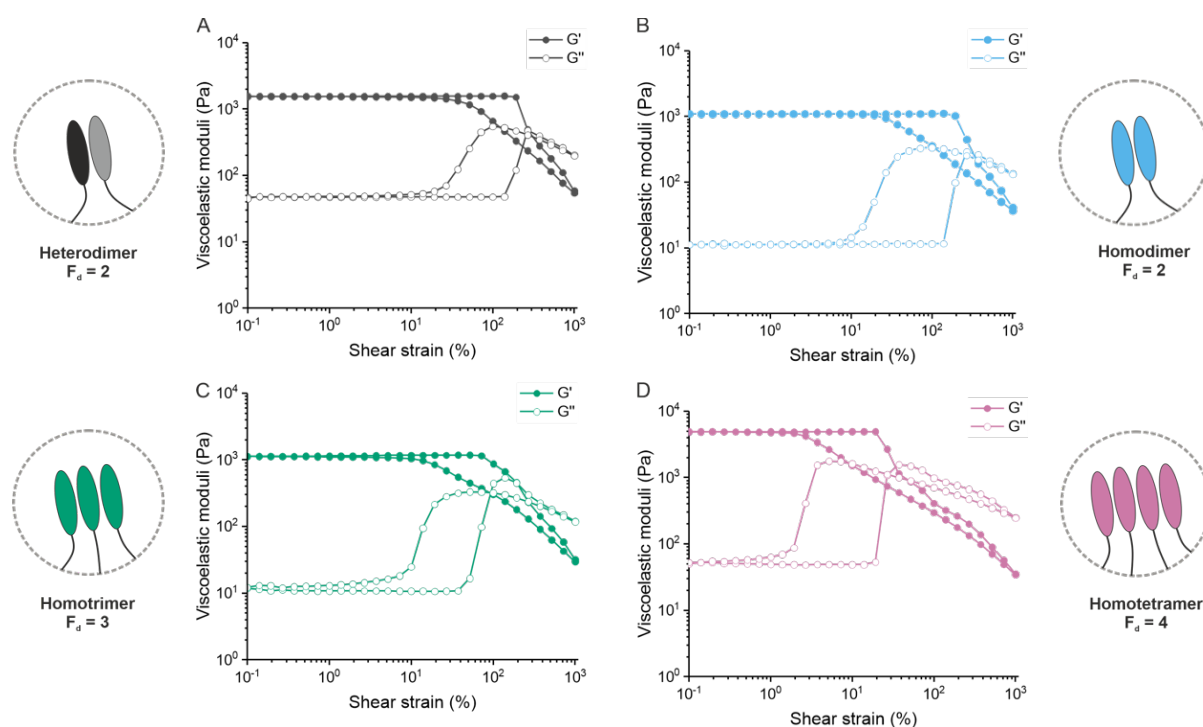
Figure 29. Representative amplitude sweeps of the CC-crosslinked hydrogels. CC Homo2, Homo3, Homo4 and Hetero2 were presented with different colors (Hetero2: F_d = 2, dark gray / Homo2: F_d = 2, sky blue / Homo3: F_d = 3, bluish green / Homo4: F_d = 4, reddish pink). The F_d represents a functionality of the dynamic crosslink (i.e. oligomerization state of the CC peptides). The oscillatory strain sweeps were performed with strain amplitudes from 0.1 % to 1000 % at a constant angular frequency of 10 rad s^{-1}.

In order to investigate dynamic properties of the CC-crosslinked hydrogels, frequency sweeps measurements were performed (**Figure S10, Table S7**). The plateau moduli from the plateau region in certain frequency range ($G_{p,FS}$) were reasonably matched with the plateau moduli from the AS measurements ($G_{o,AS}$). In general, the crossover frequency (ω_c), at which G' and G" come to meet each other at lower frequency range below the plateau region, is inversely related to the relaxation time (τ_{FS}) of the material ($\omega_c = 1/\tau_{FS}$). The relaxation times of the Hetero2- and Homo2-crosslinked hydrogels were around 230 s and 870 s, respectively (**Table S7**). However, the Homo3-crosslinked hydrogels have not shown any crossover in the measurable frequency range ($5*10^{-3} \leq \omega \leq 10^2$ rad s^{-1}). It means that the trivalent CC-crosslink systems have much longer relaxation times than the divalent crosslink systems.

Longer measurement time in FS might cause the sample drying. Thus, I have performed the stress relaxation tests based on the step-strain (**Figure 30, Table 8**) with the same measurement protocol used in the previous CMP-crosslinked hydrogels, but the waiting time was fixed with 10 min at zero-strain point. During the waiting time, two dimeric-crosslinked hydrogels (i.e. both Homo2 and Hetero2) have released almost all the pre-stress imposed from the strong mechanical perturbation during the AS; however, the trimeric and tetrameric systems could not release the stress within the waiting time of 600 s (10 min). In the SR tests, the Homo4-crosslinked hydrogel displayed the longer relaxation times compared to those of the dimeric crosslinking systems, which is almost an order of magnitude longer, while their α values were in the same range with 0.8~0.9 (**Table 8**). On the other hand, Homo3-crosslinked hydrogel showed unexpected behavior with extremely stretched exponential relaxation with the α value of 0.61, whereas the relaxation time was in the similar range with those of the dimeric crosslinks. Although It is unlike to find the systematic trend between these relaxation parameters and the oligomerization states of the CCs; however, it was obvious to observe that the relaxation behavior of the CC-crosslinked hydrogels with the divalent crosslinking systems were distinctively different from those of the trimeric and tetrameric CC-crosslinked network.
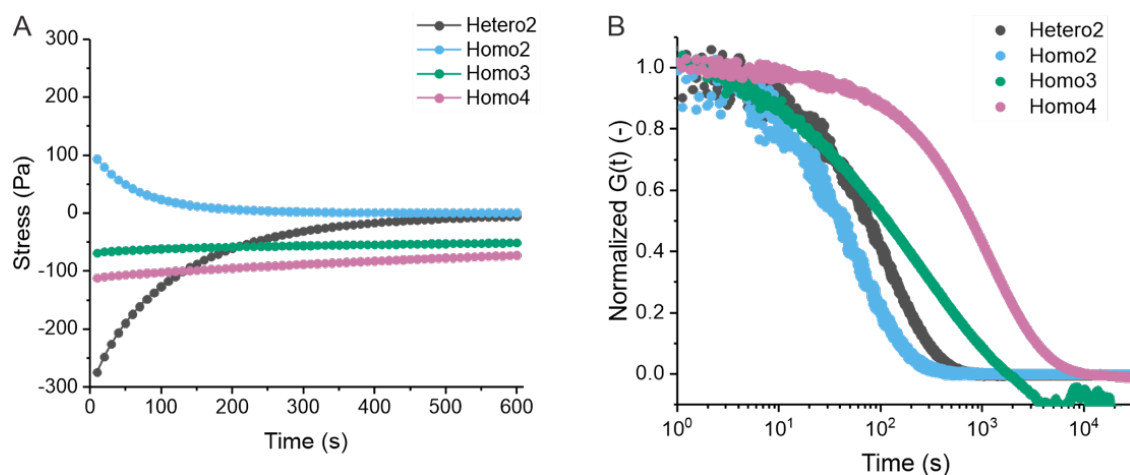
Figure 30. Stress relaxation tests of the CC-crosslinked hydrogels. The standard measurement protocol with zero-strain waiting method was used as described in the **Methods**. The amplitude sweeps with ascending strain amplitudes from 0.1 % to 1000 % was performed and the waiting time was 10 min for all the measurements. A strain of 5 % was applied in a stepwise manner for the following stress relaxation test. The relaxation of the pre-stress during the waiting time were shown in **A** (Hetero2: F_d = 2, dark gray / Homo2: F_d = 2, sky blue / Homo3: F_d = 3, bluish green / Homo4: F_d = 4, reddish purple) and the relaxation moduli during the SR tests were shown in **B** with the same color indication for each peptide. The relaxation parameters were shown in **Table 8**.

Table 8. Relaxation parameters obtained from the stress relaxation tests of the CC-crosslinked hydrogels. Relaxation times (τ) and relaxation exponents (α) of the CC-crosslinked hydrogels (**Figure 30**) were obtained using the KWW equation.

Relation parameters	CCs Hetero2	Homo2	Homo3	Homo4
Relaxation times, τ	114	61	218	1228
Relaxation exponents, α	0.89	0.87	0.61	0.82

Rotatory sweeps (RS) tests were performed to study the mechanical breaking of the CC-crosslinked hydrogels in response to the continuous rotational deformation beyond the yield point (bot stress and strain) of the material (**Figure 31**). Before reaching yield point, all the hydrogels showed the linear response with constant slopes, which are related to the stiffness of the materials as an analogue of Young's modulus in tensile test. With all the CC crosslinks, the hydrogels exhibited the shear rate dependence on the yield points: With increasing shear rates, the yield points got increased as well. Interestingly, the Homo3- and Homo4-crosslinked hydrogels exhibited remarkably higher stiffness (i.e. steeper slopes before yield points) but much lower yield points in both stress and strain compared to those of the dimeric-crosslinked hydrogels. Although the Homo3 crosslink was broken at incomparably lower stress, the strain values at the yield points were more reliable to be compared for the four crosslinking systems. Both dimeric crosslinks were broken around 300~400 % with the fastest shear rate (7 s^{-1}) but

79

the trimeric and tetrameric crosslinks showed the yield strains below 100 % at the same shear rate.

Beyond the yield points, the CC-crosslinked hydrogels showed the post-yield plateau with relatively high moduli, which seem to be proportional to the yield point of the material. In some case, the second bumps were observed (e.g. Homo2-crosslinked hydrogel); however, it could be hardly explained with the current understanding on the hydrogel network.
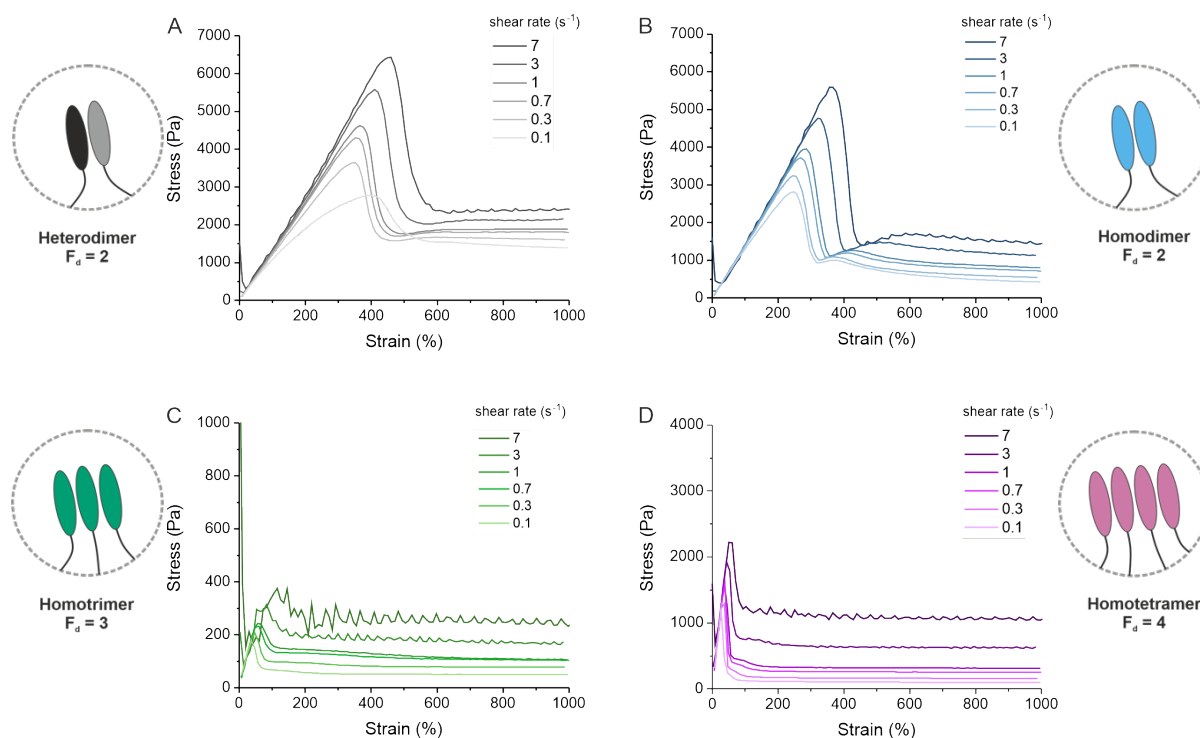
Figure 31. Stress-strain curves of the CC-crosslinked hydrogels measured with rotatory sweeps. The continuous rotational strain was applied until 1000 % with different shear rates from 7 to 0.1 s^{-1} as shown in the legend. The stress-strain curves of the Hetero2 (F_d = 2, dark gray) and the Homo2- (F_d = 2, sky blue) crosslinked hydrogels are shown in **A** and **B** respectively and the Homo3- (F_d = 3, bluish green) and the Homo4- (F_d = 4, reddish purple) crosslinked hydrogels were exhibited in **C** and **D**, respectively.

The overall mechanical properties of the CC-crosslinked hydrogels were highly affected to the dynamic crosslinking functionality. Interestingly, the dimeric crosslinks, whether it is Hetero2 or Homo2, have distinctive mechanical and viscoelastic behavior in linear and non-linear rheological properties compared to the higher oligomerization crosslinks that have more complex crosslink geometry in the network. Although I have not performed any structural properties of the network, shear rheology has proven the bulk material properties depending on the microscopic geometry of the crosslinks that associated with the crosslink functionality in terms of the LVE region as the linear rheological property but also the mechanical rupturing as the non-linear rheological behavior.

80

4.3.3 The Effect of the covalent crosslink functionality on the mechanical properties of the CC-crosslinked hydrogels

In the peptide-PEG hybrid hydrogel systems, there is additional feature that has to be considered as a crosslink point at the PEG polymers in terms of the molecular geometry (**Figure 18**). Here, F_c is defined as a crosslink functionality based on the covalent junction at the center of the PEG molecule and thus the F_c has a direct relationship with the number of PEG arms. To investigate the effect of the covalent crosslink functionality (F_c) on the bulk material properties of the CC-crosslinked hydrogels, I have utilized the 4-arm star-PEG polymer (F_c = 4) and the linear PEG (i.e. 2-arm, F_c = 2) polymer that crosslinked with CC Homo4 as the dynamic crosslink (fixed with F_d = 4). The lower oligomerization states of the CC peptides (Homo2 or Homo3) did not show proper gel formation with enough stiffness (i.e. plateau modulus) at the concentration used in the standard preparation (peptide conc. = 6 mM). For the CC Homo3 crosslink, the minimum concentration to form the hydrogels with measurable stiffness (G_p) on the rheometer was over the peptide concentration 10 or 12 mM which was about double amount of the standard concentration used in the star-PEG system, but the behavior of the gels was not reliable (**Figure S11**).

On the other hand, Homo4/linear-PEG hydrogels formed mechanically stable hydrogels with the peptide concentration of 6 mM. In the AS tests (**Figure 32-A, B**), the Homo4/star-PEG hydrogel had the G_p around 4880 Pa in the LVE region, which was more than ten times higher than that of the Homo4/linear-PEG that was about 440 Pa. It indicates that the Homo4/star-PEG (F_d/F_c = 4/4) network were remarkably stiffer than Homo4/linear-PEG network (F_d/F_c = 4/2), although the identical crosslink molecular (i.e. CC Homo4) was used with the same concentration. The stiffness of the hydrogels can be more specifically shown with the ratio between G'' to G' in the LVE region (i.e. loss factor, tanδ) from the AS tests (**Table 9**). Homo4/star-PEG network had the tanδ of 0.01, whereas Homo4/linear-PEG network showed the value of 0.06, which indicates the linear-PEG network are more viscous than the star-PEG network in general. Since a loss factor represents a ratio of a viscous portion over an elastic portion of viscoelasticity from its definition (tanδ = G''/G'), Homo4/star-PEG network exhibited about 6 times larger elastic response than Homo4/linear-PEG network under the small-amplitude oscillatory strain (SAOS) deformation.
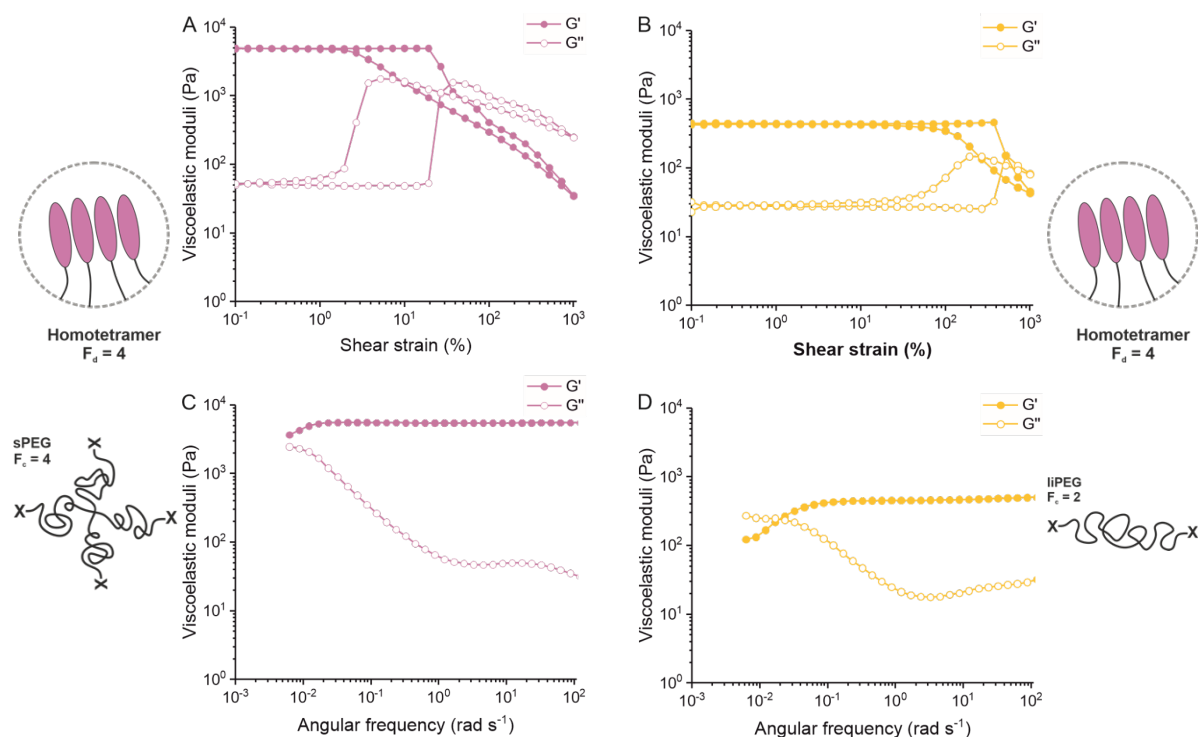
Figure 32. Viscoelastic properties of the CC Homo4-crosslinked hydrogels with the star-PEG (reddish pink) and the linear-PEG (yellow). Amplitude sweeps of the Homo4/star-PEG combination (**A**) and the Homo4/linear-PEG combination (**B**) were performed with stain amplitude range from 0.1 % to 1000 % at a constant angular frequency of 10 rad s^{-1}. Frequency sweeps of the Homo4/star-PEG combination (**C**) and the Homo4/linear-PEG combination (**D**) were performed with frequency range from 100 rad s^{-1} to 0.005 rad s^{-1} at a constant strain amplitude of 1 %. The viscoelastic parameters were shown in **Table 9**.

Table 9. Viscoelastic parameters of the CC-crosslink hydrogels with different combinations of the crosslink functionalities. Plateau moduli ($G_{o,AS}$) were obtained from the average values of the storage moduli in the LVERs. LVER was defined with the strain range until the G' values deviates more than 10 % of $G_{o,AS}$. Critical frequencies (ω_c) were obtained from the angular frequencies at the crossover points of the storage and loss moduli (G' = G").

	Homo4 + star-PEG	Homo4 + linear-PEG	Hetero2 + star-PEG
F_d/F_c	4/4	4/2	2/4
$G_{o,AS}$	4881 Pa	436 Pa	1552 Pa
tanδ (G"/G' in LVER)	0.01	0.06	0.03
LVER	19 %	373 %	139 %
ω_c	< 0.005 rad s^{-1}	0.017~0.023 rad s^{-1}	0.027 rad s^{-1}

The LVE regions showed more significant difference between two star- and linear-PEG systems. LVE region of the Homo4/star-PEG was about 19 % whereas Homo4/linear-PEG showed the linear response until 373 %, which is almost 20-fold longer LVE region. In other word, the Homo4/star-PEG network had much higher stiffness but far shorter extensibility than the Homo4/linear-PEG hydrogel.

The difference in the viscoelastic properties based on the covalent crosslink functionalities showed the similar aspects with those of the dynamic crosslinking functionality. In both cases, the LVE regions of the network were inversely proportional to the crosslinking functionalities, although it is still controversial to discuss about the stiffness of the material that is represented with plateau moduli and tanδ. However, in terms of the linear rheological behavior, which was represented with the LVE region in AS tests as well as the yield strain in RS tests, the Homo4/linear-PEG (F_d = 4/F_c = 2) network was more likely to be comparable with the Hetero2/star-PEG combination (F_d = 2/F_c = 4) (**Table 9, Figure S12**) although the identical dynamic crosslink (Homo4, F_d = 4) was used in both the star-PEG and the linear-PEG network.

Also, the crossover frequency (ω_c) from the FS tests of the Homo4/linear-PEG network looked more similar to that of the Hetero2/star-PEG combination (**Figure S12-C, D**). The network of Homo4/linear-PEG behaved in more similar way with Hetero2/the star-PEG hydrogels, which has comparable combination of the crosslinking functionalities (F_d/F_c = 4/2 and 2/4, respectively). It seems that the network connectivity based on the combination of the crosslink functionalities (F_d/F_c) has more critical effect on the viscoelastic behavior of the bulk materials than the molecular properties (e.g. thermodynamic properties) of the crosslinks.

Stress relaxation behaviors of the CC-crosslinked hydrogels also exhibited the supportive results (**Figure 33**). During the waiting time after AS, the Homo4/linear-PEG (F_d/F_c = 4/2) and Hetero2/star-PEG (F_d/F_c = 2/4) networks released the pre-stress significantly about 87.7 % and 98.1 %, respectively. On the other hand, Homo4/star-PEG hydrogel (F_d/F_c = 4/4) could not release the pre-stress like the other systems but showed only partial relaxation of 35.1 % of the initial stress within 10 min. The relaxation times (τ_{SR}) of the Homo4/linear-PEG hydrogel was about 285 s which is in the same order of magnitude with that of the Hetero2/star-PEG network (114 s), whereas the Homo4/star-PEG system exhibited an order of magnitude longer relaxation time (1228 s). Interestingly, the relaxation exponents extracted from the KWW equation were almost identical in the three systems (**Table 10**), but only the relaxation times showed the difference depending on the systems that has different functionalities of the dynamic or covalent crosslink.
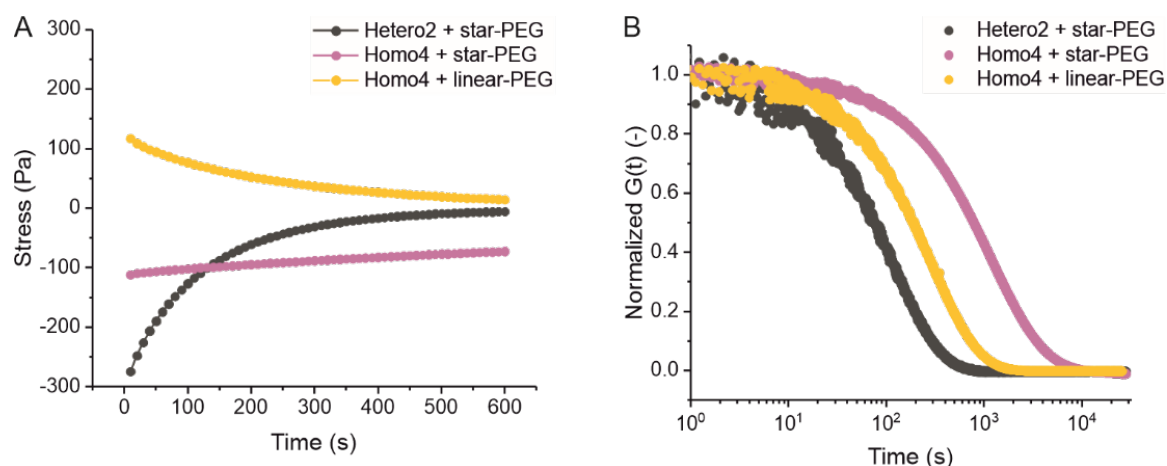
Figure 33. Stress relaxation tests of the Homo4-crosslinked star-PEG hydrogel (reddish pink), the Homo4-crosslinked linear-PEG hydrogel (yellow) and the Hetero2-crosslinked star-PEG hydrogel (dark gray). The measurements were performed with the standard measurement protocol for the stress relaxation tests with the zero-strain waiting time methods for 10 min after the amplitude sweeps were performed. Relaxation of the stresses during the waiting time were displayed in **A.** Stress relaxation curves after applying a strain of 5 % in a stepwise manner were shown in **B** and the relaxation parameters were obtained using the KWW equation (**Table 10**).

Table 10. Relaxation parameters of the CC-crosslinked hydrogels with different combinations of the crosslink functionalities. The amount of the relaxed stress during the waiting time were calculated from the ratio of the stress values at the end of waiting time (10 min) and the initial stress value right after AS. The relaxation parameters were obtained using the KWW equation.

parameters	Peptide/PEG Homo4/star-PEG	Homo4/linear-PEG	Hetero2/star-PEG
F_d/F_c	4/4	4/2	2/4
Stress relaxed during waiting time	35.1 %	87.7 %	98.1 %
Relaxation times, τ	1228	285	114
Relaxation exponents, α	0.82	0.89	0.89

Mechanical yielding of the hydrogels with RS tests were performed to study the further effect of the covalent crosslinking functionality on the network (**Figure 34**). The mechanical behavior of the Homo4/star-PEG hydrogels (**Figure 34-A**, reddish pink) upon the yielding of the crosslinks showed also significant difference from the Homo4/linear-PEG network (**Figure 34-B**, yellow). The linear-PEG-based hydrogels exhibited much lower stiffness (i.e. lower slopes in the linear range before material yielding) as well as the large yield strains in a range from around 300 % to 600 % at the strain rates from 0.1 s^{-1} to 7 s^{-1}, respectively. It was almost 6 times larger yield strains than those of the Homo4/star-PEG networks. Interestingly, the yield

stresses of both linear-PEG and star-PEG hydrogels were in the similar range between 1000 to 3000 Pa also with shear rate dependency. In comparison with the dimeric CC crosslinks, the yield strains of Homo4/linear-PEG network were observed in the similar range with the Hetero2/star-PEG. It gave the supporting evidence that the mechanical properties based on the material breaking were also affected more by the combination of the dynamic and covalent crosslinks rather than molecular properties of the crosslinks themselves.
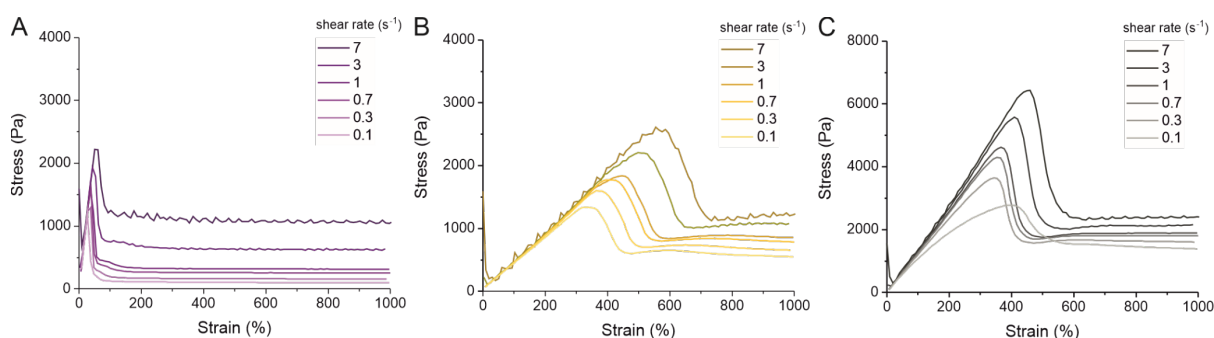
Figure 34. Mechanical yielding behavior of the Homo4/star-PEG hydrogel (A, reddish pink), the Homo4/ linear-PEG hydrogel (B, yellow), and the Hetero2/star-PEG hydrogel (C, dark gray) measured with rotatory sweeps. The rotatory sweeps were performed with applying the continuous rotational strain to 1000 % with different shear rates from 7 to 0.1 s^{-1} as written in the legends. The stiffness of the hydrogels can be estimated with the slopes of the initial linear region and the yield points are associated with the peaks at the end of the linear regions. The toughness of the hydrogel is related to the area under the curves.

The covalent crosslink functionality designed from the molecular geometry of the PEG polymers has a huge effect on various mechanical behaviors of the CC-crosslinked hydrogels such as linear viscoelastic range, plateau modulus, relaxation time, and mechanical yield. From various mechanical and viscoelastic properties of the Homo4/star-PEG combination (F_d/F_c = 4/4) generally showed stiffer and more brittle mechanical behaviors as well as more complex stress relaxation behavior than those of the Homo4/linear-PEG network (F_d/F_c = 2/4). For the summary, the mechanical and viscoelastic behaviors of the CC-crosslinked hydrogels were strongly affected with the network connectivity based on the combination of the crosslink functionalities and thus it can be strong evidence that the crosslink functionality should be considered as the critical design parameter for the peptide-based bioimimetic crosslink in the peptide-polymer hybrid hydrogels.

4.4   Self-reporting biomimetic peptides based on the fluorescence self-quenching effect

Fluorescence-labeled CMPs were prepared with in house synthesis using SPPS. 5(6)-carboxyfluorescein was coupled with the free N-terminal amine on the resin and cleaved together with the pre-synthesized peptides for the better purification; however, the peptide purification done with using preparative HPLC showed that the purifications were not done completely even after the second runs of the preparative or analytical HPLC (**Figure S2**). Although the incomplete purification of the CF-CMPs, the purest fractions were used for the following fluorescence experiments, but also the main impurities in the fraction seemed to be non-coupled peptides and/or one cysteine group missed CMPs which were expected not to critically affect the fluorescence measurements.

4.4.1   Self-reporting systems based on the fluorescence self-quenching of the CF-labeled CMPs

Fluorescence profiles of the CF-labeled $(PPG)_{10}$ peptides in solution (PBS) were measured (**Figure 35**). The peptide solution was incubated at 4 °C for more than 48 h to allow the formation of stable triple helical structures and measured the emission spectra at the same temperature in the spectrofluorometer. The emission spectrum showed the peak at 524 nm with around 0.83×10^6 cps/microamps of intensity in the homotrimeric helix of a $CF-(PPG)_{10}$. When the temperature increased to 47 °C where the thermal denaturation of the $(PPG)_{10}$ occurs, the peak position was slightly shifted to 521 nm with the increased intensity of 2.57×10^6 cps/microamps. It indicates that the triple helical structures of $CF-(PPG)_{10}$ were denatured, resulting in the increase of the fluorescence intensity about 3 times in a monomer state where the FSQ effect was absent. This can be the clear confirmation of the FSQ of the $CF-(PPG)_{10}$ at the homotrimeric state due to the close proximity between dyes in CTHs. It was the consistent result from the literature [146] which showed about 3-4 times increase of the fluorescence with thermal denaturation of the $CF-(PRGPOG)_5$ peptide. Consistent with the fluorescence intensity change, the CF- CMP systems showed also the visual color change from dark orange to green color when the $CF-(POG)_7$ was dissociated, indicating the CF-CMPs showed the darker color at a homotrimer sate due to the FSQ effect, whereas the fluorescence showed brighter green color at a monomer state (**Figure S13**).

86
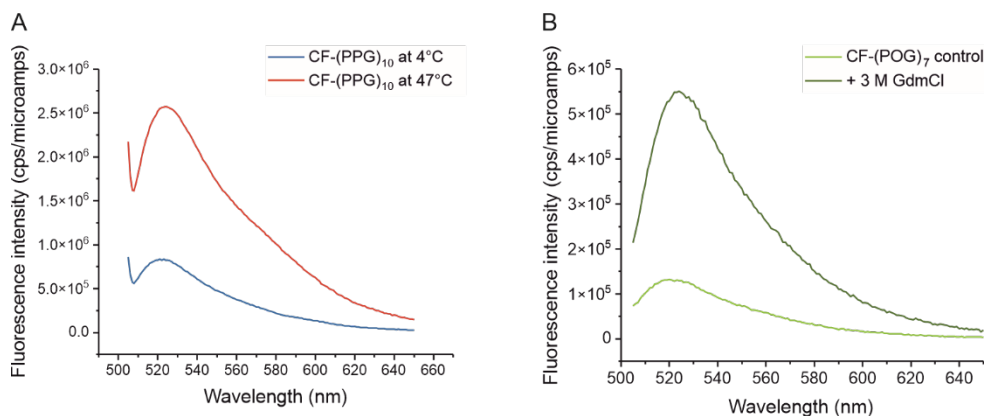
Figure 35. Fluorescence profiles of the CF-(PPG)$_{10}$ peptide measured for the thermal denaturation (A) and the CF-(POG)$_7$ peptide measured for the chemical denaturation in a presence of guanidinium chloride (B). A The fluorescence spectra of the CF-(PPG)$_{10}$ peptide solution with a concentration of 0.1 µM in PBS (pH 7.4) were measured with an excitation wavelength at 497 nm and an emission wavelength range from 500 to 650 nm. The emission peaks were shown around 524 nm. The peptide solution was stored at 4 °C for over 48 h to form a stable triple helical structures and measured at the same temperature (blue). Temperature was increased to 47 °C that is higher than the melting temperature of (PPG)$_{10}$ peptide (T$_m$~30 °C) and the spectrum was measured after waiting 15 min (red). **B** The spectra of the CF-(POG)$_7$ peptides with a concentration of 0.5 µM in PBS buffer (pH 7.4) with 3 M guanidinium chloride were measured with the identical measurement setup as described in **A**.

In a presence of the chemical denaturant such as guanidinium chloride with the CF-(POG)$_7$ peptide in solution, the change in the fluorescence intensity of the CF-(POG)$_7$ was clearly observed (**Figure 35-B**). Fluorescence intensity increased clearly about 4 times with 3 M guanidinium chloride in CF-(POG)$_7$ peptide solutions. The peak positions were also slightly shifted with a trimeric state around 520~521 nm and a monomer state at 524 nm. As consistent results, both CF-(PPG)$_{10}$ and (POG)$_7$ showed the FSQ effect when they form the CTHs that were proved using the different denaturation methods (i.e. thermal and chemical ways) with monitoring the increase of the fluorescence intensity when the triple helix is dissociated.

4.4.2 Dissociation kinetics measurement via competitive assay of the CF-CMPs

FSQ effect based on the CF-CMPs can be utilized to study for peptides/proteins dissociation or re-association kinetics via competitive assay. Any external stimulus (e.g. heating or adding chemical denaturants) was excluded to measure the dissociation rates of the CF-CMPs at room temperature. CF-CMPs, such as (PPG)$_{10}$ and (POG)$_7$, pre-equilibrated at lower temperature were mixed with excess amount of unlabeled CMPs as the competitors to form a heterotrimer and the fluorescence intensity was monitored over time at RT (**Figure 36**).
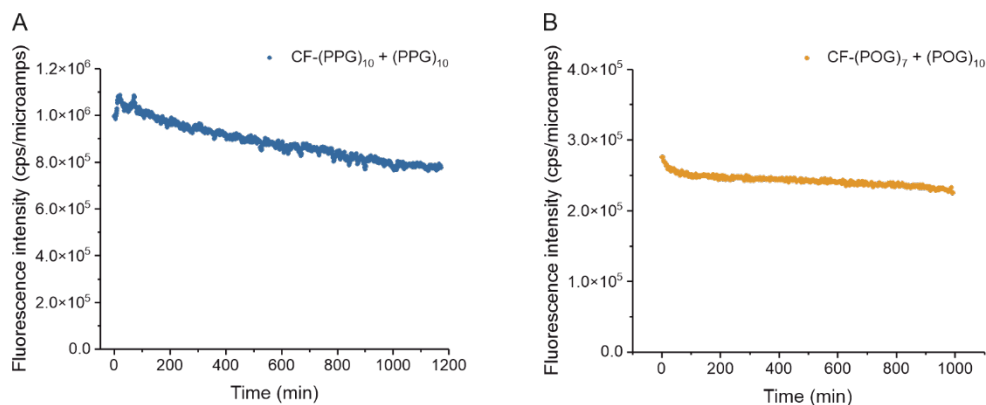
Figure 36. Competitive assays of the CF-(PPG)$_{10}$ peptide with the unlabeled (PPG)$_{10}$ peptide as a competitor (A) and of the CF-(POG)$_7$ peptide with the unlabeled (POG)$_{10}$ peptide (B). A CF-(PPG)$_{10}$ peptide solution (0.5 µM conc. in PBS buffer pH 7.4) was mixed with 100x excess amount of the unlabeled (PPG)$_{10}$ peptide (50 µM conc. in PBS buffer pH 7.4) as a competitor. The fluorescence emission intensity at 524 nm was monitored for 1200 min (20 h) with an excitation wavelength was 497 nm at room temperature (~ 23°C). **B** CF-(POG)$_7$ peptide solution (0.5 µM conc. in PBS buffer pH 7.4) was mixed with 10x excess of the unlabeled (POG)$_{10}$ peptide (5 µM conc. in PBS buffer pH 7.4) as a competitor. The fluorescence emission intensity at 524 nm was monitored for about 990 min (~17 h) with an excitation wavelength was 497 nm at room temperature (~ 23°C).

Interestingly, both CF-(PPG)$_{10}$ and CF-(POG)$_7$ showed the gradual declines after mixing with excess amount of the unlabeled competitors, which was the opposite results to the initial prediction, although the visual color change experiment, which was an analogous competitive assay but with thermal denaturation, showed a clear indication of the formation of the heterotrimer species showing higher fluorescence (**Figure S13**). Right after mixing of the CF-labeled CMPs were mixed with unlabeled CMPs, the solutions had a color of dark orange due to the FSQ, indicating the CTHs in the solution were still homotrimeric state of the CF-CMPs at the beginning. When the solutions were heated above the melting temperature, the color of the solution dramatically turned to the bright green resulting from the recovery of the fluorescence because of the denaturation of the homotrimeric state of CF- CMPs to the monomer sate. After certain time with re-equilibration at low temperature (3 days), the CF-(POG)$_7$ solution with excess amount of the unlabeled (POG)$_{10}$ still showed the bright green color, whereas the control solution mixed with buffer without competitor turned back to the dark orange color forming homotrimeric structure again. This result can be a clear prediction that the competitive assay should show the increase of the fluorescence with dissociation of the homotrimers and re-association to the heterotrimers due to the excess amount of the competitors in the solution.

Due to the extremely slow kinetics of the collagen molecules, the long-term measurement of the competitive assay was also performed. In the long-term measurement, the trend seems more complex (**Figure 37**). After mixing with unlabeled CMPs, the fluorescence decreased for initial 20~30 h at the beginning following by the gradual increase for almost 4 days. When the identical mixture was heated at 70 ˚C after the long-term kinetics measurement, the

fluorescence intensity increased about 2 times (**Figure S16**). It can be evidence that the self-quenched CMPs still existed in the solution even after a week of measurement. It seems that there are two dominant processes exist in the long-term kinetics. Some possible explanations will be discussed in the following discussion chapter.
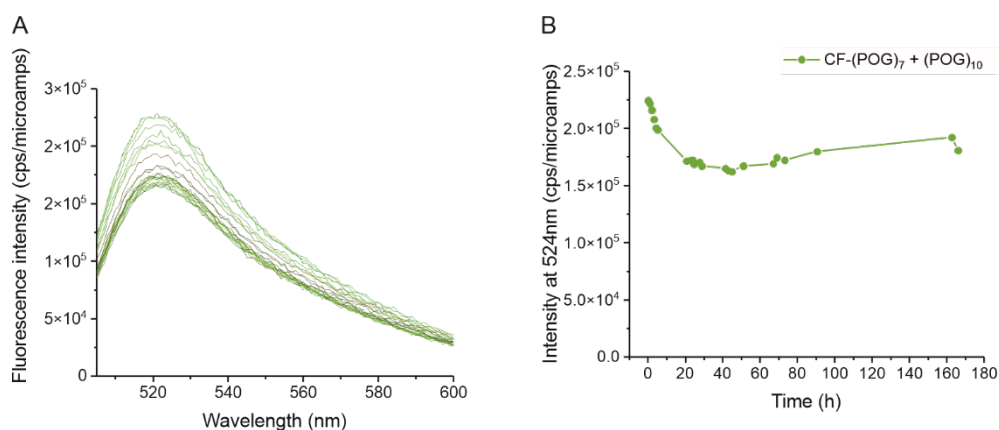
Figure 37. Competitive assay of the (POG)$_7$ peptide with the unlabeled (POG)$_{10}$ peptide measured for a week. A The fluorescence spectra of the CF-(POG)$_7$ peptide solution (0.5 µM conc. in PBS buffer pH 7.4) mixed with the unlabeled (POG)$_{10}$ peptide solution (5 µM conc. in PBS buffer pH 7.4) were measured for a week. An excitation wavelength was 497 nm and an emission wavelength range was from 505 to 600 nm every 1 nm step. The data points during the measurements were arbitrary obtained for the long-term measurements within a week. The measurements were performed at room temperature (~23 °C). **B** Fluorescence intensities at the peak positions (524 nm) were plotted as a function of time from the fluorescence spectra in **A.**

5   Discussion

Proteins that form a complex fibrous network architecture play an important role in the extracellular matrix for its structure as well as mechanical stability. As a biological soft materials, extracellular protein-based networks show viscoelasticity, which directly affects cellular behavior [6]. A variety of protein structural motifs have been investigated with the goal of understanding the biophysical and biochemical properties of the ECM on the molecular level. Inspired by structural motifs of the ECM proteins, collagen triple helix structures and coiled coils superhelices have been used as physical crosslinks within well-characterized polymeric backbones for many biological applications, including two-dimensional or three-dimensional scaffolds for cell culture and tissue engineering [82, 158, 189-193]. The CTH- and CC-based crosslinks associate through self-assembly. At the same time, they respond to changes in pH, temperature, or mechanical force. In combination, this introduces dynamic and stimuli-responsive characteristics into the network.

In this work, I have investigated two types of protein-inspired dynamic crosslinks. Specifically, I utilized CTH and CC structural motifs as crosslinks in PEG-based polymeric networks. Using synthetic peptides, provides molecular control over the crosslink properties. For example, to control the thermodynamic and kinetic properties of CMPs, I utilized different amino acid sequences, i.e. $(PPG)_{10}$ vs. $(POG)_{10}$, and different peptide length, i.e. $(POG)_7$ vs. $(POG)_{10}$. This allowed me to investigate how these crosslink parameters determine the bulk hydrogel properties, in particular stress relaxation. The distinctive relaxation behavior of the resulting collagen-inspired hydrogels was closely related to the physicochemical properties of the CMP-crosslinks. In this chapter, I will discuss the possible molecular origin of the unique compressed exponential stress relaxation of the CMP-crosslinked hydrogels with an emphasis on crosslinking kinetics.

Presumably, the trivalent nature of CMP crosslinks critically determines the network behavior in addition to the physicochemical properties of the CMPs themselves. To investigate the effect of crosslink functionality, CCs with different oligomeric states were employed as dynamic crosslinks instead of CMPs. Depending on the CC crosslink functionality, the resulting hydrogels exhibited different linear viscoelastic properties as well as different yield points. Also, varying the number of arms on the PEG polymers showed that the crosslink functionality is a key determinant of the linear and non-linear hydrogel properties.

In the last section, I aimed to investigate the possibility of using a self-reporting strategy for monitoring the assembly state of CMP crosslinks. Specifically, I used fluorescently labeled

CMPs to visualize the molecular picture of the crosslinks with a real-time optical read-out. This approach can potentially become a powerful method for observing the dissociation and re-association of dynamic crosslinks, caused by an external load or deformation. Even though the functionalization of the CMPs with the fluorophores was successful, the purification of dye labeled CMPs turned out to be a major bottleneck and further optimization is necessary. It also remains an open question on the intensity difference between the associated CTHs and the dissociated peptide chains is sufficient to provide the desired real-time read-out.

5.1   Aging and compressed exponential relaxation of the collagen-inspired hydrogels

Stress relaxation is a vital feature of the ECM, which is key for its mechanobiochemical function. Inspired by collagen molecules, which are the fundamental building blocks of collagen fibers in the ECM, self-assembled and dynamic peptide-crosslinks have been utilized in peptide-PEG hybrid hydrogels. These collagen-inspired hydrogels exhibited slow dynamics and aging in stress relaxation experiments. The relaxation times and the relaxation exponents were highly affected by the sample age. The sample age was defined by the waiting time between a large mechanical perturbation, exerted via an amplitude sweep, and the starting point of the stress relaxation test. This aging phenomenon is reminiscent of the behavior of soft glassy materials that generally show heterogeneous and out-of-equilibrium states that change very slowly but continuously towards equilibrium [30].

Most probably, the amplitude sweep generates internal pre-stress during this large mechanical perturbation. Remaining stresses within the network were relaxed relatively quickly in the $(POG)_7$- and $(PPG)_{10}$-crosslinked hydrogels. But the stress relaxed much slower in the $(POG)_{10}$-crosslinked hydrogel (**Figure 24-B, C, D**). When the step-strain was applied for the stress relaxation test (γ = 5 %), the relaxation times and the relaxation exponents depended on the waiting times. In general, the relaxation times and exponents decreased with increasing waiting time (**Table 5, Figure 25**). This suggests that stress relaxation is highly affected by the pre-stress remaining in the network at the end of the waiting time. The faster relaxation times in the $(PPG)_{10}$- and $(POG)_7$-crosslinked hydrogels and the absence of compressed exponents suggests that the hydrogels are less affected by the pre-stress and that the networks reach a close-to-equilibrium state at the of each respective waiting time. On the other hand, the $(POG)_{10}$-crosslinked networks presented much longer relaxation times. Also,

relaxation exponents in the compressed exponential region show that the pre-stress within the (POG)$_{10}$-crosslinked hydrogels was not relaxed after a short waiting time of 10 min. The relaxation exponent reduced towards the stretched exponential regime with increasing waiting time until 60 min, suggesting that the network may reach equilibrium within this time window. The observation of compressed exponential relaxation after a waiting time of 10 min, in which the pre-stress stayed in a plateau, is reminiscent of the jammed state of other soft glassy materials, which also show compressed exponential relaxation [194-197]. For many soft glassy materials, the origin of compressed exponential relaxation is often not fully understood. Here, the stress relaxation behavior of the collagen-inspired hydrogels can be related to the crosslink dynamics.

Regarding the origin of the aging behavior and the unique compressed exponential stress relaxation of the collagen-inspired hydrogels, the amplitude sweep performed before the stress relaxation tests has a critical effect on the following stress relaxation behaviors of the material. Applying large oscillatory strain amplitudes (maximum with 1000 % of strain) cause strong mechanical perturbation, resulting in a disordered state that can be estimated when monitoring the pre-stress within the network during the waiting time. However, the re-association rates of the CMP-crosslinks observed from the hydrogel self-healing test (**Table 11**) were much faster than the association rates of the CMPs in solution that were reported in the literature [93]. The higher local concentration of the CMPs in the network could enhance the nucleation process of the association reaction of the CMP-crosslinks compared to free CMPs in solutions.

Table 11. Recovery of the storage modulus (G') from the self-healing tests of the CMP-crosslinked hydrogels (Figure 23). The values in () are the relative amounts of the recovered G' values in comparison to the G' values at 1200 s.

Storage modulus G'	(PPG)$_{10}$	(POG)$_7$	(POG)$_{10}$
G' at 10 s [Pa]	755 (0.27)	592 (0.51)	838 (0.35)
G' at 20 s [Pa]	2222 (0.80)	996 (0.86)	2245 (0.93)
G' at 600 s [Pa]	2740 (0.99)	1138 (0.98)	2411 (0.99)
G' at 1200 s [Pa]	2764 (1.00)	1164 (1.00)	2424 (1.00)

It could be shown that the amplitude sweeps performed before the stress relaxation tests have a critical effect on the subsequent stress relaxation behavior. Applying large oscillatory strain amplitudes (maximum at 1000 % strain) causes a strong mechanical perturbation, which most probably breaks bonds that may partially re-associate in the strained state (Figure 39). To fully understand how this may be related to the network topology, the rate of crosslink re-association needs to be considered. After applying 1000 % of oscillatory strain, all CMP-crosslinked hydrogels recovered more than 80 % of their plateau modulus within 20 s. After 600 s, the G' values were almost fully recovered although they kept increasing slowly. In a study by Engel et al. [93], the apparent rate constants of triple helix nucleation were reported to be as 800 and 875,000 $M^{-2} s^{-1}$ for $(PPG)_{10}$ and $(POG)_{10}$, respectively. This might mean that only a small fraction of crosslinks were broken during the amplitude sweep although the strain amplitude ($\gamma_{max.}$ = 1000 %) was larger than the yield strain of the hydrogels (**Figure 22-A**). Considering a heterogeneous network as a starting point, rupture of a few crosslinks may be enough to cause the network to flow (G'' > G') as a result of the mechanical perturbation. The fast G' recovery rates can then be explained when only small number of broken crosslinks need to re-associate. With this hypothesis, some features of the network can be more clearly postulated. Firstly, the other crosslinks that were not broken might remain as intact clusters in the network. Thus, the overall network could become even more heterogeneous and disordered after the amplitude sweep, which is an important characteristic of soft glassy materials. Secondly, the PEG chains with broken crosslinks can re-associate in the strained state. Once the strain is removed, the re-associated crosslinks may become extended and experience pre-stress. As a result, the network structure after the amplitude sweeps may consist of intact clusters and newly formed crosslinks that connect the clusters and reside in extended network chains (**Figure 38**).
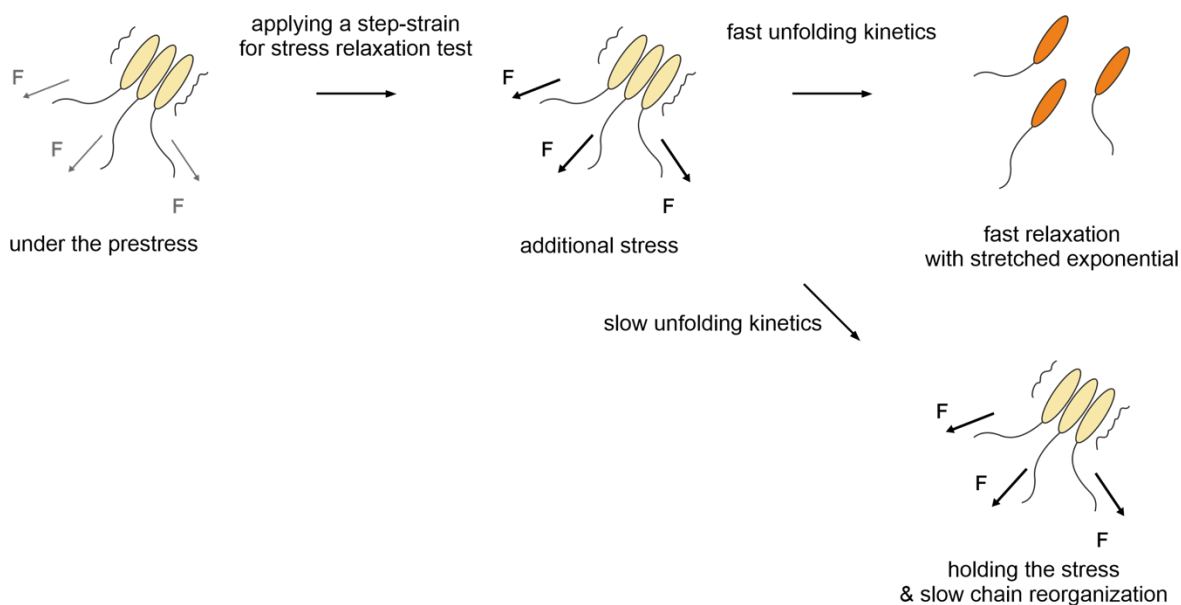
Figure 38. Molecular picture of the CMP-crosslinks in the network during the stress relaxation tests. During the waiting time after the amplitude sweep, the CMP crosslinks are under pre-stress, which might be not large enough to break the crosslinks mechanically but this pre-stress on the crosslinks could affect to the dissociation of the CMP-crosslinks when the additional step-strain was applied for the actual stress relaxation test in the protocol. If the crosslink has fast dissociation kinetics, the resulting network can relax the stress quickly with fast relaxation times and the relaxation exponents show stretched exponential. When the crosslink has extremely slow dissociation kinetics, the resulting network can hold the stress for a longer time. As a result, the chain reorganization might get slower as well without relaxation of the applied stress in a short time. In this case, the hydrogel shows much longer relaxation time, and the compressed exponential relaxation is observed.

In addition to this postulated increase in network heterogeneity, topological defects such as elastically inactive crosslinks, originating from primary loop formation or dangling ends, should be considered as intrinsic heterogeneity [198]. These may form as a result of an incomplete coupling reaction, as described in the illustration of the network (**Figure 17-C**) in the experimental design section. Heterogeneous networks and slow dynamics are both key characteristics of natural soft glassy materials such as the ECM and the cytoskeleton. The actin cytoskeleton, which governs the mechanical behavior of living cells, exhibits unexpectedly slow stress relaxation of internal stresses via transient crosslinking, similar to the dynamics of soft glassy materials [24, 199, 200].

To determine possible effects of the strain protocol (i.e. amplitude sweep) as well as the sample preparation (e.g. sample manipulation during loading on rheometer), the hydrogels were "gelled" directly on the rheometer. After mixing the peptide solution with 4-arm star-PEG powder, the sample was directly loaded onto the rheometer. After gelation for 2-3 h, the stress relaxation test was performed without external mechanical history (**Figure S14**). Interestingly, the (POG)$_{10}$-crosslinked hydrogels exhibited stretched exponential stress relaxation, combined with a shorter relaxation time, although the fitting with the KWW equation was poor.

With the standard measurement procedure (i.e. strain protocol with AS), the $(POG)_{10}$-crosslinked hydrogels prepared on the rheometer again showed compressed exponential stress relaxation with a longer relaxation times (**Figure S15**). This can be considered as strong evidence that the large mechanical deformation caused by the amplitude sweep leads to the observed compressed exponential stress relaxation. It is still not fully understood why the relaxation time was shorter. But the effect of the mechanical perturbation and the resulting pre-stress on the stress relaxation behavior of the collagen-inspired hydrogels seems to be clear, particularly for the $(POG)_{10}$-crosslinked hydrogels. With a different strain protocol based on a step-strain of 1000 % (**Figure 27-B**), the relaxation behavior of the $(POG)_{10}$-crosslinked hydrogels was similar, i.e. long relaxation times and large compressed exponents were observed. But both values were larger than those from the AS-based protocol, particularly the α values were even larger than 2 after short sample aging and stayed in compressed region even with a waiting time of 60 min. The physical explanation is still missing but it seems obvious that the degree or the way of applying mechanical perturbation with the different strain protocols has a detectable effect on the resulting relaxation behavior.

Once the strain is released, the remaining internal pre-stress can only be released via dissociation of the CMPs. The $(PPG)_{10}$ and $(POG)_7$ crosslinks, which have the fastest dissociation rates (**Table 4**), can relax the stress within a relatively short time. As a result, stretched exponential stress relaxation is observed at 25 °C. In contrast, the $(POG)_{10}$ crosslinks possess much slower dissociation kinetics at 25 ° and can withstand the stress for an extended period of time. $(POG)_{10}$ crosslinked networks show an initial plateau in G(t) and start to relax the stress slowly as it was observed for the 30 min or 60 min waiting times (**Figure 24-B, C, D**). The relaxation of the pre-stress during the waiting time determines the aging behavior of these collagen-inspired hydrogels. If the peptides have fast association and dissociation kinetics, the peptide-crosslinked hydrogels could reach their equilibrium state within the waiting time. However, collagen is generally known to display slow kinetics [103]. The dissociation kinetics of the CMPs is thus the key to understand the observed slow stress relaxation and aging behavior of the CMP-crosslinked hydrogels as well as the unique compressed exponential relaxation in the $(POG)_{10}$ crosslinked network.

The relaxation times and fitting parameters were highly affected by the CMPs used in the hydrogels. Only the $(POG)_{10}$ hydrogels showed extremely slow relaxation times and uncommon compressed exponential stress relaxation at 25 °C, while the $(POG)_7$ and $(PPG)_{10}$ crosslinked hydrogels exhibited relatively faster relaxation times with stretched exponents. To validate this result and to exclude that the thermal stabilities of the CMPs affect the observed stress relaxation behavior, measurements at different temperatures were also performed. It should be noted that the melting temperatures of $(POG)_7$ and $(PPG)_{10}$ are relatively close to

25 °C where the stress relaxation test was performed. This may mean that the fraction folded and thus the number of active crosslinks formed is not identical when comparing $(POG)_7$ and $(PPG)_{10}$ with $(POG)_{10}$ (**Figure 20**, **Table 3**). At 25 °C, all $(POG)_{10}$ crosslinks should be fully folded at equilibrium. In contrast, the $(POG)_7$ network may only possess 78 % of active crosslinks while the $(PPG)_{10}$ contains 89 % at the same temperature of 25 °C. Therefore, the network structure should not be considered as identical. The measurement temperature was thus decreased to 20 °C for $(PPG)_{10}$ and to 15 °C for $(POG)_7$. At these temperatures, the fraction of folded crosslinks should approximate F~0.99. Under these conditions, both hydrogels showed remarkably increased relaxation times and exponent values. Particularly, the $(PPG)_{10}$ crosslinked hydrogels exhibited compressed exponential stress relaxation, similar to the $(POG)_{10}$ crosslinked hydrogels at 25 °C.

Dissociation kinetics of the CMPs are highly affected by the temperature as estimated from the Arrhenius plots of the CD temperature-jump experiments. The extrapolated apparent dissociation rates give a good explain regarding the overall trend of the stress relaxation behavior. At 47 °C, $(POG)_{10}$ showed a similar apparent dissociation rate (**Figure S7**) as the other CMPs at 5 °C (**Figure 26**). Under these conditions, the hydrogels showed similar relaxation times ($\sim 10^{-6}$ s^{-1}) and exponents (1.1~1.3). Also, these temperature-controlled stress relaxation tests indicate that the dissociation kinetics of the dynamic CMP crosslinks has a huge impact on stress relaxation of the bulk network.

Interestingly, a few other soft glassy materials also showed compressed exponential relaxation, such as colloidal fractal gels, concentrated emulsions, and lamellar gels [30]. Also, these materials show slow dynamics and an evolution of their properties with sample age. Clearly, the $(POG)_{10}$ hydrogel at room temperature and the $(POG)_7$ and $(PPG)_{10}$ hydrogels at 5 °C display exactly these two properties as a result of slow crosslink dissociation kinetics. Slow crosslink dissociation can also lead to jamming, which has served as another physical explanation for compressed exponential stress relaxation. Similar to the reduced mobility of particles in a colloidal gel system, also the CMP-crosslinked hydrogels can be temporarily frozen in a glassy state because of the slow dissociation kinetics of the CMPs. In general, the physical meaning of compressed exponential relaxation has not been fully uncovered. In this work, compressed exponential relaxation can clearly be related to molecular features of the crosslinks (i.e. kinetics of CMP dissociation) and, for the first time, tuning crosslink properties has allowed for controlling the transition between stretched and compressed exponential relaxation.

5.2 Effect of crosslinking functionality on coiled coil-inspired hydrogels

Collagen-inspired hydrogels showed a distinctive stress relaxation behavior, originating from the dissociation kinetics of the CMP-crosslinks. At the start of this work, it was largely unexplored if and how the crosslink functionality and thus network topology affects stress relaxation. Unlike heterodimeric crosslinks, which have been utilized for the formation of homogenous networks based on 4-arm star-shaped PEG backbones [201], homotrimeric crosslinks might lead to a less homogeneous network structure. Homooligomeric crosslinks may cause a higher number of topological defect (e.g. primary loops) that are not elastically active and do not contribute to network connectivity. In addition, more different types of nodes are possible for homotrimeric than for homodimeric crosslinks. These include nodes where the three crosslink components are linked to different star-PEG molecules (elastically active trivalent crosslink), nodes where two crosslink components are linked to the same PEG molecule and the third component connects to another PEG molecule (elastically active divalent crosslink) and nodes where the three components are all attached to the same PEG molecule (elastically inactive crosslink). In addition, the efficiency of the coupling reaction contributes to the heterogeneity of the network, possibly causing dangling ends (inactive PEG arm) and freely diffusing peptides that may participate in triple helix formation without being coupled to a PEG arm (elastically active divalent crosslink or elastically inactive crosslink).

The importance of the crosslink functionality and its role in increasing network heterogeneity has been poorly studied so far. As CMPs are intrinsically trimeric, coiled coil (CC)-forming peptides are an excellent substitution. CC structural motifs are abundant in natural protein-based materials such as the ECM and the cytoskeleton. The sequence-structure-mechanics relationship of CC structural motifs has drawn significant attention in recent times [106, 113, 202]. In addition, CC motifs have been utilized as self-assembling and dynamic crosslinks for bioinspired and biomimetic hydrogels [70, 131]. Particularly, CC motifs can be engineered to obtain well-defined oligomeric states such as homodimers, homotrimers and homotetramers [85]. And even higher order oligomeric states up to homononamers have been obtained [86] (**Figure 8**).

In this study, CCs were thus used to investigate the effect of crosslink functionality, which is defined as the number of PEG arms at the crosslinking junction. When using terminally functionalized star-PEG, the PEG introduces an additional crosslink junction with a functionality of 4. This means that two different types of crosslinks and their functionalities need to be considered in the CC peptide-PEG hybrid networks. Firstly, the CC oligomerization state determines the functionality of the dynamic crosslinks (F_d) and the crosslinks used were

homodimeric (Homo2, F_d = 2), homotrimeric (Homo3, F_d = 3), and homotetrmeric (Homo4, F_d = 4). In addition, a heterodimer (Hetero2, F_d = 2) was used as a reference system. Secondly, the 4-arm star-PEG introduces a covalent crosslink with a functionality of F_c = 4. Complemented with a linear PEG, which can be considered to possess two arms (F_c = 2), also the role of covalent network junctions could be investigated. All combinations of the dynamic and covalent crosslinks used are shown in the **Table 12**.

Table 12. Combinations of the crosslinking functionalities with the dynamic crosslinks defined with the CC oligomerization states and with the covalent crosslinks defined with the number of the arms of the PEGs. In addition to CC homooligomers, CC heterodimer (Hetero2) was used as a reference system (**Table S1**). CC Homo2, Homo3, Homo4, and Hetero2 were implemented to investigate the effect of the crosslinking functionality of the dynamic crosslinks (F_d, highlighted in blue). The 4-arm star-PEG and 2-arm linear-PEG were used to study the effect of the crosslinking functionality of the covalent crosslinks (F_c, highlighted in red).

Oligomerization state of CCs	star-PEG	linear-PEG
Homo2	F_d = 2 F_c = 4	-
Homo3	F_d = 3 F_c = 4	-
Homo4	F_d = 4 F_c = 4	F_d = 4 F_c = 2
Hetero2	F_d = 2 F_c = 4	-

The sequences of the CC-peptides were based on research from Woolfson et al. [85]. Using a series of CCs with the same basic sequence, only residues in the hydrophobic core were exchanged to alter the oligomeric state of the CC superhelical structure. The thermodynamic properties of the CC peptides had been published [85, 113, 131] and were confirmed in this work (**Figure 28**). CC Homo3 has the lowest melting temperature of around 52 °C ($T_{m.lit.}$ ~ 56 °C). This T_m is comparable to $(POG)_{10}$ (T_m ~ 61 °C). The other CC peptides have higher melting temperatures (Homo2 ~69 °C; Homo4 > 90 °C). It is important to point out that the thermal stabilities of the CC peptides showed no clear relationship with the viscoelastic properties of the corresponding CC-crosslinked hydrogels. This may be a first indication that the viscoelastic properties of the materials may rely more strongly on the CC crosslink functionality than on its thermodynamic properties.

One of the most distinctive differences in the viscoelastic properties of the CC-crosslinked hydrogels is the LVE region, obtained from amplitude sweeps (**Figure 29**). Hydrogels with dimeric CC crosslinks (Homo2 and Hetero2), exhibited the largest LVE region up to 200-300 % strain. For the networks containing the homotrimeric crosslink (70 %) or the tetrameric crosslink (20 %) the LVE region is significantly lower and seems to decrease with increasing crosslink functionality. This reduction of the LVE region with increasing oligomeric state can be explained with the formation of additional chain entanglements that contribute additional physical crosslinks.

According to this hypothesis, however, it may be expected that the plateau moduli (G_p) of the CC-crosslinked hydrogels increase proportional to the contribution of the chain entanglements. It would thus be expected that the Homo4-crosslinked hydrogel should have a higher G_p than the Homo3-crosslinked hydrogel and the hydrogels crosslinked with the dimeric CCs. Indeed, the Homo4-crosslinked hydrogel exhibited the highest G_p about 4900 Pa, which was outstandingly high compared to the networks with dimeric crosslinks that showed only 1100 Pa and 1550 Pa for Homo2- and Hetero2-crosslinked hydrogels, respectively. However, the Homo3-crosslinked hydrogel did not show any clear difference in the plateau modulus (G_p ~ 1150 Pa) compared to the dimeric systems. The reason might be that the crosslink concentration is lower for Homo3 than for the dimeric systems. All CC-crosslinked hydrogels were prepared with 6 mM of the peptide concentration (see Methods). Thus the theoretical maximum concentration of crosslinks is 2 mM for the trimeric system and 3 mM for the network with dimeric crosslinks (**Table 13**). Thus, the reduced crosslink concentration of the Homo3 network might be compensated with the increasing number of chain entanglements. Another contributing factor may be the lower thermodynamic stability of Homo3 compared to Homo2 and Hetero2.

Table 13. Concentrations of the CC peptides used for the hydrogel preparation and calculated crosslink concentrations. The crosslink concentrations were calculated with the number of the oligomeric states, assuming 100 % coupling efficiency and an ideal network without any defect.

Concentrations	Hetero2 (mM)	Homo2 (mM)	Homo3 (mM)	Homo4 (mM)
Peptides	6 mM	6 mM	6 mM	6 mM
Crosslinks	3 mM	3 mM	2 mM	1.5 mM

Mechanical yielding of the CC-crosslinked hydrogels also showed clear differences when comparing the trimeric/tetrameric crosslinks to the dimeric crosslinks (**Figure 31**). In the stress-strain curves, the dimeric crosslinks exhibited much higher yield stresses (i.e. higher strengths) and, as a result, higher toughness (i.e. area under the curve before material yield) than the trimeric and tetrameric crosslinks. The smaller yield strains of the trimeric and tetrameric crosslinks might again be explained based on chain entanglements. With more chain entanglements, the extensibility of the PEG polymers could be highly restricted. As a result, the crosslinks feel the deformation sooner, causing smaller yield strains in Homo3- and Homo4-crosslinked networks. This result is also consistent with the shorter LVE region that was observed in the amplitude sweeps. Interestingly, the stiffness of the hydrogels (i.e. the slope in the linear regime) is higher for the Homo4-crosslinked network when compared to the Homo2- and Hetero2-crosslinked hydrogels. Again, this result is consistent with the higher plateau modulus measured in the amplitude sweep.

To compare to the CMP-crosslinked hydrogels, also the stress relaxation behavior was investigated for all CC-crosslinked networks (**Figure 30, Table 8**). For the stress relaxation test, the waiting time between the amplitude sweep and the application of the step-strain was fixed with 600 s (10 min) at zero strain. Networks with dimeric crosslinks relaxed the pre-stress almost completely during this 10 min waiting time, while the pre-stress was not fully relaxed for hydrogels with trimeric and tetrameric crosslinks. In the following stress relaxation test, the trimeric crosslink showed stretched exponential stress relaxation with a relaxation exponent of 0.61, whereas networks with dimeric crosslinks exhibited exponents around 0.87-0.89, although the relaxation times were not so different (in a range from tens to hundreds of seconds). In comparison to the CMP-crosslinked networks, this shows that compressed exponential relaxation is not a direct function of crosslink functionality. As dissociation rates of CMPs are much slower than for CCs, this experiments thus supports the earlier conclusion that compressed exponential relaxation depends on crosslink dissociation rates.

The above results also suggest that the stress relaxation behavior of the CC-crosslinked hydrogels is more strongly affected by the crosslink functionality than by the thermodynamic stabilities of the CC peptides. Considering the melting temperatures of the CC peptides no clear correlation could be observed with the relaxation time, suggesting that other effects dominate. To obtain proof that the crosslink functionality plays an important role, the covalent crosslink functionality was varied while using the same dynamic CC crosslink. PEGs with different numbers of arms have been utilized in a number of studies (e.g. 2-arm [82], 4-arm [72], and 8-arm [71]) in combination with various dynamic crosslinks (e.g. dimeric [70], trimeric [158], or even multimeric [203]. However, the effect of the covalent crosslink functionality has not been studied in a systematic way.

The hydrogel where Homo4 was combined with 4-arm star-shaped PEG (Homo4/star-PEG, F_d=4/F_c=4) showed dramatic differences when compared to the network when 2-arm linear-shaped PEG was crosslinked with Homo4 (Homo4/linear-PEG, F_d=4/F_c=2). With linear-PEG, the LVE region dramatically extended about 20 times, while the plateau modulus decreased almost 10 times (**Figure 32**). Interestingly, the viscoelastic properties of the Homo4/linear-PEG (F_d=4/F_c=2) network are similar to those of the Hetero2/star-PEG (F_d=2/F_c=4) network, particularly when considering their LVE region (from AS) and the relaxation times (from FS) (**Table 9**). The rotational stress-strain experiments showed a large yield strain and high toughness of the Homo4/linear-PEG network, similar to the 4-arm PEG networks containing dimeric CCs (**Figure 34**). Also, the Homo4/linear-PEG network showed a similar stress relaxation behavior as the Hetero2/star-PEG hydrogel (**Figure 33, Table 10**).

In short, almost all measured network properties of the CC-Homo4/linear-PEG hydrogel are more similar to those of the CC-Hetero2/star-PEG network than to those of the CC-Homo4/star-PEG hydrogel, which has the same dynamic crosslink but a different covalent crosslink functionality. The rheological behavior of the CC-inspired hydrogels thus seem to be mainly determined by the crosslink functionalities. Interestingly this does not depend on the type of crosslink (i.e. dynamic vs. covalent). The results clearly show that the network connectivity is more important for determining the viscoelastic properties as the Homo4/linear-PEG (F_d/F_c = 4/2) network showed similar material properties as the Hetero2/star-PEG (F_d/F_c = 2/4) hydrogel. This might mean that the crosslink functionality governs the bulk network properties via defining the complexity of the network.

Overall, this was the first systematic study designed to test the effect of the crosslink functionality. It could be shown that the crosslinking functionality determines the network connectivity, which primarily affects the network behavior under deformation. Depending on the requirements for the LVE region and the toughness of the hydrogels, the crosslink functionality emerges as a key design parameter. The thermodynamic and kinetic properties appear to play a subtler role and no clear rules can be derived at this moment that could be employed for tuning the relaxation time, which is critical for biological and biomedical applications. Here, heterotrimeric or heterotetrameric crosslinks would allow for testing different functionalities while using one and the same crosslink with fixed thermodynamic and kinetic properties.

5.3   Self-reporting system based on fluorescence self-quenching

In previous chapters, I focused on the bulk viscoelastic properties of collagen-inspired and coiled coil-inspired hydrogels, measured mainly using shear rheology. The molecular processes during material deformation or under stress had to be estimated based on the bulk material properties. Establishing a correlation with the molecular crosslink properties was only possible based on the parallel biophysical investigation of the dissociation kinetics using CD spectroscopy. Clearly, shear rheology is a powerful tool to study the viscoelastic behavior of materials. But it provides only indirect information about molecular processes within the network. In order to obtain a more direct picture about the assembly state of the peptide crosslinks, a self-reporting system based on fluorescence self-quenching was investigated.

Fluorescence self-quenching (FSQ) has been utilized to study CMP association/dissociation as well as helical composition [145, 146, 181, 204, 205]. Carboxyfluorescein was introduced to the CMPs through the N-terminus coupling after they were synthesized. Despite several rounds of optimization, the yield of the fluorophore coupling reaction was relatively low. Further, separation of CF-labeled and unlabeled CMPs was difficult on RP-HPLC using a C_{18}-column (**Figure S1**). The chromatogram and the MALDI-TOF data show that the dye-coupled peptides contain impurities (e.g. unlabeled peptides or CMPs missing the cysteine) in the final product. Therefore, the concentrations of CF-$(PPG)_{10}$ or CF-$(POG)_7$ used in the experiments cannot be considered to be accurate. Considering this aspect, I will only discuss about the general trends seen in the first test experiments.

The fluorescence measurements, after thermal or chemical denaturation confirm self-quenching of the CF-coupled CMPs (**Figure 35**). When the triple helical structure was denatured, the effect of FSQ disappeared, which increased the fluorescence intensity about 3 or 4 times. This value is consistent with earlier reports in the literature [146]. Even though the peptides lacked purity, it was still possible to form a heterotrimer of dye coupled CMPs. As a self-reporting system, the distinctive increase in fluorescence between the folded and unfolded states appears useful for establishing a real-time optical read-out to observe changes in the relative number of associated crosslinks in the hydrogel network. At the same time, the relatively small intensity difference between folded and unfolded states may prohibit the observation of molecular processes when only a small number of crosslinks are involved. To visualize the dissociation of a small number of crosslinks, stronger quenching may be required. This could possibly be achieved with Förster resonance energy transfer (FRET), implemented in a heterooligomeric system, such as a heterodimeric CC.

The ability to monitor kinetic processes was still investigated, focusing on the dissociation kinetics of the CMPs without any external stimulus (e.g. thermal or chemical denaturation). A competitive assay was performed where unlabeled CMPs were added to a solution of CF-CMPs. The unlabeled CMPs were added in excess so that dissociated CF-CMPs most likely re-associate with unlabeled CMPs (**Figure 36**). The expected result was that the fluorescence intensity would increase after the competitor is mixed with the sample as the formed heterotrimers of CF-CMPs and unlabeled CMPs do not display any self-quenching. Monitoring the change in fluorescence intensity after mixing is thus expected to yield the dissociation rates of the CF-CMPs. However, the competitive assay did not show the expected result for both CF-$(PPG)_{10}$ and CF-$(POG)_7$. The fluorescence decreased when adding the unlabeled competitor at least for the first 15 ~ 20 h of the measurements (**Figure 36**). It could mean that the dissociation rates of the CF-CMPs were too slow at the room temperature to be measured. When the samples were measured for one week (**Figure 37**), the intensity slowly increased after 24 h until the end of the measurement (for about 6 days, 144 h). It is currently not clear what causes the decrease in fluorescence during the first hours of the measurement. It suggests stronger self-quenching in the initial stages of the measurement. It cannot be excluded that this is related to the exchange of one CF-labeled chain with an unlabeled chain, resulting in a species that contains two fluorophores attached to the triple helical structure (**Figure 39**). The interaction and orientation between the fluorophores could be different and the magnitude of FSQ could be affected. After 24 h, the dominant species becomes the heterotrimer with two unlabeled CMPs and one CF-CMP where FSQ is absent. Clearly, the quenching mechanism and the molecular features of the CF-labeled CMPs are not yet completely understood.
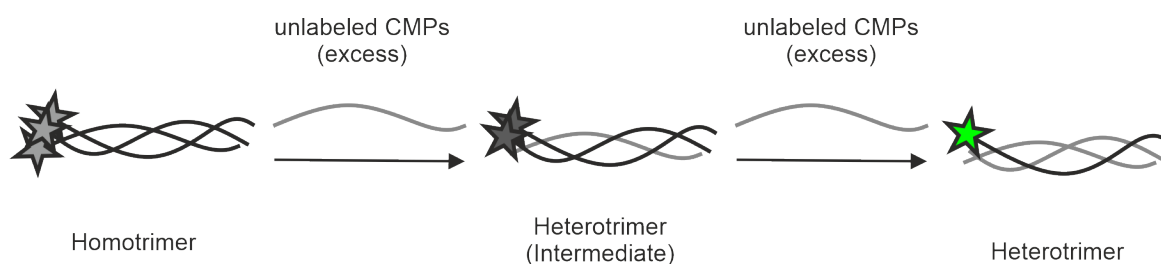
Figure 39. Schematic explanation of the chain exchange during the competitive assay. In the homotrimeric state of the CF-labeled CMPs, the fluorescence intensity is lower than the monomer state due to the FSQ effect. After adding the unlabeled CMPs as competitors in excess amount, one CF-CMP chain in the homotrimer can be exchanged with an unlabeled CMP chain at thermal equilibrium, forming the intermediate heterotrimer with two CF-CMP chains and one unlabeled CMP chain. This intermediate heterotrimer might show stronger FSQ effect than the homotrimer of the CF-labeled CMPs due to the change in the molecular interactions between CF molecules. The fluorescence intensity thus decreases with increasing the number of intermediate species until the dominant species becomes the heterotrimer which has only one CF-CMP chain in the helix and the others are unlabeled CMP chains. The fluorescence intensity can increase with increasing the number of the final heterotrimeric species.

Independent of a possible intermediate, the obtained results also suggest that the dissociation kinetics of the CMPs is extremely slow at room temperature. This is clearly consistent with the general knowledge about the dissociation kinetics of collagen [103, 206]. Since the dissociation kinetics of the CMPs were successfully measured with CD temperature-jump experiments, the kinetics measurement based on FSQ was not optimized further. Considering the slow kinetics, self-reporting CMPs may not be a good model system for investigating dissociation events in hydrogel networks under equilibrium conditions; however, the CF-labelled CMPs are promising reporters when the dye-coupled crosslinks are ruptured and/or re-associated under loading and/or deformation. A more general strategy may be implemented with coiled coils, where strand exchange has already been monitored with a FRET reporter system [147]. Considering the half-life of coiled coils, which us in the range from seconds to hours, these systems may serve as a more valuable reporter to monitor network reorganization in real-time.

6   Conclusions and Outlook

In this work, I demonstrate novel insights into the molecular features of hydrogels that are physically crosslinked with ECM-inspired peptides (such as CMPs and CCs). Self-assembled CMP and CC superhelices were used as physical and reversible crosslinks that can dissociate and re-associate. They thus confer viscoelasticity to the network, which is a critical design parameter for many biological hydrogel applications. CMP and CC crosslinks further respond to mechanical force or deformation as well as other external stimuli, such as changes in temperature, pH or the addition of chemical denaturants. Here, I investigated how bottom-up molecular control can be exerted to understand and tune the viscoelastic properties of peptide-polymer hybrid hydrogels. Specifically, I focused on the dissociation kinetics of the CMP-based crosslinks and on the oligomerization state of CCs. This work revealed that the extraordinarily slow kinetics of CMP dissociation has a dominant effect on the stress relaxation behavior of CMP-crosslinked hydrogels. Furthermore, using CCs of different oligomerization states, it was shown that crosslink functionality critically determines hydrogel stiffness and yield stress while no clear the relationship between crosslink stability and viscoelastic properties could be observed.

Collagen association and dissociation is known to be a slow process. Triple helical peptide model systems are thus an interesting model system for studying the effect of slow crosslink kinetics as a possible design parameter for collagen-inspired hydrogels. Using CMPs of different length and sequence, I demonstrated for the first time that the dissociation kinetics of CMP crosslinks plays an important role during the stress relaxation of the entire network. Particularly, (POG)$_{10}$ crosslinked hydrogels showed extremely slow relaxation times with uncommon compressed exponential stress relaxation. This effect was most pronounced when the (POG)$_{10}$ crosslinked hydrogel was probed shortly after a large amplitude deformation (i.e. 10 min of aging time). With increasing aging time, an evolution of the relaxation parameters was observed. Aging is a typical characteristic of soft glassy materials, which also include biological systems such the cytoskeleton [24, 207]. At short aging times, compressed exponential relaxation was observed, which had not yet been reported for hydrogels. In combination with aging, compressed exponential relaxation is more common in fractal colloidal gels, concentrated emulsions and lamellar gels where it has mostly been observed for structural relaxation processes, detected with scattering methods.

Slow kinetics and the presence of out-of-equilibrium states are critical features related to aging and compressed exponential relaxation; however, the exact mechanisms are often unresolved. In this work, I focused on the control of the dynamic crosslink properties at the molecular level

and could show that molecular control of the dissociation kinetics allows for tuning the relaxation parameters. Most interestingly, I was able to tune the temperature such that one and the same hydrogel could be switched from stretched to compressed exponential stress relaxation. Although the crosslink kinetics clearly showed a dominant role in determining stress relaxation in the network, topological effects may also play a role and may be closely related to the presence of jammed structures that need to be released before the entire network can relax. Therefore, future work should also focus on the interplay between crosslink kinetics and the mesoscale structural relaxation, e.g. using fluorescence reporter systems that allow for monitoring local network structure and reorganization.

Another important feature of CMP crosslinks is their trimeric nature, which ultimately determines the crosslinking functionality. Collagen triple helices are intrinsically restricted with respect to the number of chains. Even though biomimetic peptide crosslinks are increasingly used as hydrogel crosslinks, systematic studies targeting the role of their oligomerization states, which can directly control the connectivity of the network, have not been performed yet. Also, the molecular geometry of the PEG polymers (i.e. star-PEG vs. linear-PEG) commonly used in peptide-polymer hybrid hydrogels has not yet been systematically investigated as a design parameter to control material properties. CCs provided a powerful model system for studying the effect of crosslink functionality as they exist in different oligomerization states. Here, a homodimer, homotrimer and homotetramer were utilized as dynamic crosslinks instead of CMPs. Furthermore, a 4-arm star- PEG polymeric backbone was compared to linear PEG.

The linear viscoelastic range, stiffness and yield stress were critically affected by the crosslink functionality. Also, the molecular geometries of the PEG polymers showed a distinctive effect on these material properties. When using the homotetrameric CC to crosslink star-PEG or linear-PEG remarkably different mechanical properties were obtained, despite one and the same dynamic CC crosslink was used. Interestingly, the material properties of the tetramer-crosslinked linear-PEG (i.e. $F_d=4/F_c=2$) were remarkably similar to those of the dimer crosslinked star-PEG (i.e. $F_d=2/F_c=4$). This may indicate that the network connectivity itself is more critical than the molecular properties of the crosslinks. Despite clear correlations between crosslink functionality, linear viscoelastic range, stiffness and yield stress the relaxation time could not be clearly correlated with either the crosslink functionality or the crosslink stability, suggesting that possible relationships between these parameters may be less dominant.

In order to obtain deeper insights into the role of local crosslink assembly states, a fluorescence reporting system based on fluorescence self-quenching was implemented.

Carboxyfluorescein labeled CMPs were synthesized and tested for their potential to allow for measuring CMP kinetics in solution and within the hydrogel network. Potentially CF-CMPs could also be used as mechanosensitive reporters in hydrogel networks. I demonstrated that FSQ of CF-CMPs increases upon triple helix formation, causing a reduction in fluorescence intensity when compared to the denatured state; however, the kinetic analysis of CF-CMPs was challenging due to the extremely slow dissociation rates of CMPs. Considering also the only moderate difference in fluorescence intensity in the quenched and free state, the tested CMP-based reporter system may not be the best strategy for visualizing the assembly state of crosslinks. Once more suitable reporter systems, such as FRET-labelled coiled coils, have been developed a wide variety of fluorescence imaging techniques can be used to monitor the relative crosslink concentration as well as mechanical rupture and recovery in real-time.

In summary, this work offers valuable insights into the importance of molecular control on hydrogel crosslinks. ECM-inspired model peptides are excellent tools as their properties can be tuned in a highly controlled manner. As a result, the effect of different molecular parameters on the viscoelastic properties of bioinspired hydrogels can be systematically investigated and design principles can be deduced. Above all, using CMP-based crosslinks with slow dissociation kinetics provided new insights into relaxation processes within soft glassy materials. Furthermore, it was shown that crosslink functionality and thus network topology can be utilized as another fundamental design parameter for tuning the mechanical properties of dynamically crosslinked hydrogels. Considering the great potential of converting CMP and CC model peptides into self-reporting crosslinks, ECM-inspired peptide-polymer hybrid hydrogels serve as a great platform for the development of novel smart biomaterials for application in cell culture, tissue engineering and soft robotics.

References

1.   Aizenberg, J. and P. Fratzl, *Biological and Biomimetic Materials.* Advanced Materials, 2009. **21**(4): p. 387-388.
2.   Mason, T.O. and U. Shimanovich, *Fibrous Protein Self-Assembly in Biomimetic Materials.* Advanced Materials, 2018. **30**(41): p. 1706462.
3.   Wegst, U.G.K., et al., *Bioinspired structural materials.* Nature Materials, 2015. **14**(1): p. 23-36.
4.   Meyers, M.A., et al., *Biological materials: Structure and mechanical properties.* Progress in Materials Science, 2008. **53**(1): p. 1-206.
5.   Fletcher, D.A. and R.D. Mullins, *Cell mechanics and the cytoskeleton.* Nature, 2010. **463**(7280): p. 485-492.
6.   Chaudhuri, O., et al., *Effects of extracellular matrix viscoelasticity on cellular behaviour.* Nature, 2020. **584**(7822): p. 535-546.
7.   Caliari, S.R. and J.A. Burdick, *A practical guide to hydrogels for cell culture.* Nature Methods, 2016. **13**(5): p. 405-414.
8.   Drury, J.L. and D.J. Mooney, *Hydrogels for tissue engineering: scaffold design variables and applications.* Biomaterials, 2003. **24**(24): p. 4337-51.
9.   Li, L., et al., *A Nanostructured Conductive Hydrogels-Based Biosensor Platform for Human Metabolite Detection.* Nano Letters, 2015. **15**(2): p. 1146-1151.
10.   Kim, Y.S., et al., *Thermoresponsive actuation enabled by permittivity switching in an electrostatically anisotropic hydrogel.* Nature Materials, 2015. **14**(10): p. 1002-1007.
11.   Grove, T.Z., et al., *Stimuli-Responsive Smart Gels Realized via Modular Protein Design.* Journal of the American Chemical Society, 2010. **132**(40): p. 14024-14026.
12.   Cao, M., et al., *Reversible Thermoresponsive Peptide–PNIPAM Hydrogels for Controlled Drug Delivery.* Biomacromolecules, 2019. **20**(9): p. 3601-3610.
13.   Reddy, N.N., et al., *Magnetic and electric responsive hydrogel–magnetic nanocomposites for drug-delivery application.* Journal of Applied Polymer Science, 2011. **122**(2): p. 1364-1375.
14.   Raman, R., et al., *Light-degradable hydrogels as dynamic triggers for gastrointestinal applications.* Science Advances, 2020. **6**(3): p. eaay0065.
15.   Hoque, J., N. Sangaj, and S. Varghese, *Stimuli-Responsive Supramolecular Hydrogels and Their Applications in Regenerative Medicine.* Macromol Biosci, 2019. **19**(1): p. e1800259.
16.   Sui, Z., W.J. King, and W.L. Murphy, *Protein-Based Hydrogels with Tunable Dynamic Responses.* Advanced Functional Materials, 2008. **18**(12): p. 1824-1831.
17.   Jonker, A.M., D.W.P.M. Löwik, and J.C.M. van Hest, *Peptide- and Protein-Based Hydrogels.* Chemistry of Materials, 2012. **24**(5): p. 759-773.
18.   Theocharis, A.D., et al., *Extracellular matrix structure.* Advanced Drug Delivery Reviews, 2016. **97**: p. 4-27.
19.   Frantz, C., K.M. Stewart, and V.M. Weaver, *The extracellular matrix at a glance.* J Cell Sci, 2010. **123**(Pt 24): p. 4195-200.
20.   Malandrino, A., et al., *Complex mechanics of the heterogeneous extracellular matrix in cancer.* Extreme Mechanics Letters, 2018. **21**: p. 25-34.
21.   Nam, S., et al., *Strain-enhanced stress relaxation impacts nonlinear elasticity in collagen gels.* Proceedings of the National Academy of Sciences, 2016. **113**(20): p. 5492-5497.
22.   Winer, J.P., S. Oake, and P.A. Janmey, *Non-Linear Elasticity of Extracellular Matrices Enables Contractile Cells to Communicate Local Position and Orientation.* PLOS ONE, 2009. **4**(7): p. e6382.
23.   Storm, C., et al., *Nonlinear elasticity in biological gels.* Nature, 2005. **435**(7039): p. 191-194.
24.   Bursac, P., et al., *Cytoskeletal remodelling and slow dynamics in the living cell.* Nature Materials, 2005. **4**(7): p. 557-561.
25.   Fabry, B., et al., *Scaling the microrheology of living cells.* Phys Rev Lett, 2001. **87**(14): p. 148102.

26.	Sollich, P., et al., *Rheology of Soft Glassy Materials.* Physical Review Letters, 1997. **78**(10): p. 2020-2023.

27.	Bandyopadhyay, R., et al., *Slow dynamics, aging, and glassy rheology in soft and living matter.* Solid State Communications, 2006. **139**: p. 589-598.

28.	Mayer, P., et al., *Heterogeneous Dynamics of Coarsening Systems.* Physical Review Letters, 2004. **93**(11): p. 115701.

29.	Cipelletti, L., et al., *Universal aging features in the restructuring of fractal colloidal gels.* Phys Rev Lett, 2000. **84**(10): p. 2275-8.

30.	Cipelletti, L., et al., *Universal non-diffusive slow dynamics in aging soft matter.* Faraday Discussions, 2003. **123**(0): p. 237-251.

31.	Aamodt, J.M. and D.W. Grainger, *Extracellular matrix-based biomaterial scaffolds and the host response.* Biomaterials, 2016. **86**: p. 68-82.

32.	Karp, G.P.N.L., *Cell and molecular biology. concepts and experiments 1 1.* 2008, Hoboken, N.J.: John Wiley & Sons.

33.	Chaudhuri, O., et al., *Hydrogels with tunable stress relaxation regulate stem cell fate and activity.* Nat Mater, 2016. **15**(3): p. 326-34.

34.	Wichterle, O. and D. LÍM, *Hydrophilic Gels for Biological Use.* Nature, 1960. **185**(4706): p. 117-118.

35.	Roorda, W.E., et al., *Synthetic hydrogels as drug delivery systems.* Pharmaceutisch Weekblad, 1986. **8**(3): p. 165-189.

36.	Chen, M., et al., *Synthesis of a super-absorbent nanocomposite hydrogel based on vinyl hybrid silica nanospheres and its properties.* RSC Advances, 2020. **10**(67): p. 41022-41031.

37.	Varaprasad, K., et al., *A mini review on hydrogels classification and recent developments in miscellaneous applications.* Mater Sci Eng C Mater Biol Appl, 2017. **79**: p. 958-971.

38.	George, J., et al., *Neural tissue engineering with structured hydrogels in CNS models and therapies.* Biotechnol Adv, 2020. **42**: p. 107370.

39.	Xu, J., et al., *The role of chemical and physical crosslinking in different deformation stages of hybrid hydrogels.* European Polymer Journal, 2018. **100**: p. 86-95.

40.	Jeon, O., et al., *Highly Elastic and Tough Interpenetrating Polymer Network-Structured Hybrid Hydrogels for Cyclic Mechanical Loading-Enhanced Tissue Engineering.* Chemistry of Materials, 2017. **29**(19): p. 8425-8432.

41.	Catoira, M.C., et al., *Overview of natural hydrogels for regenerative medicine applications.* Journal of Materials Science: Materials in Medicine, 2019. **30**(10): p. 115.

42.	Kumar, A.C. and H. Erothu, *Synthetic Polymer Hydrogels*, in *Biomedical Applications of Polymeric Materials and Composites*. 2016. p. 141-162.

43.	Vasile, C., et al., *New Developments in Medical Applications of Hybrid Hydrogels Containing Natural Polymers.* Molecules (Basel, Switzerland), 2020. **25**(7): p. 1539.

44.	Xiong, X., et al., *Responsive DNA-Based Hydrogels and Their Applications.* Macromolecular Rapid Communications, 2013. **34**(16): p. 1271-1283.

45.	Wang, C., R.J. Stewart, and J. Kopecek, *Hybrid hydrogels assembled from synthetic polymers and coiled-coil protein domains.* Nature, 1999. **397**(6718): p. 417-20.

46.	Mantha, S., et al., *Smart Hydrogels in Tissue Engineering and Regenerative Medicine.* Materials, 2019. **12**(20): p. 3323.

47.	Xu, L., et al., *Biodegradable pH-responsive hydrogels for controlled dual-drug release.* Journal of Materials Chemistry B, 2018. **6**(3): p. 510-517.

48.	Ying, G., et al., *Bioprinted Injectable Hierarchically Porous Gelatin Methacryloyl Hydrogel Constructs with Shape-Memory Properties.* Advanced Functional Materials, 2020. **30**(46): p. 2003740.

49.	Gargava, A., C. Arya, and S.R. Raghavan, *Smart Hydrogel-Based Valves Inspired by the Stomata in Plants.* ACS Applied Materials & Interfaces, 2016. **8**(28): p. 18430-18438.

50.   Heo, Y.J., et al., *Long-term in vivo glucose monitoring using fluorescent hydrogel fibers.* Proceedings of the National Academy of Sciences, 2011. **108**(33): p. 13399-13403.

51.   Gresham, R.C.H., C.S. Bahney, and J.K. Leach, *Growth factor delivery using extracellular matrix-mimicking substrates for musculoskeletal tissue engineering and repair.* Bioact Mater, 2021. **6**(7): p. 1945-1956.

52.   Pepelanova, I., et al., *Gelatin-Methacryloyl (GelMA) Hydrogels with Defined Degree of Functionalization as a Versatile Toolkit for 3D Cell Culture and Extrusion Bioprinting.* Bioengineering (Basel), 2018. **5**(3).

53.   Hersel, U., C. Dahmen, and H. Kessler, *RGD modified polymers: biomaterials for stimulated cell adhesion and beyond.* Biomaterials, 2003. **24**(24): p. 4385-4415.

54.   Hall, H. and J.A. Hubbell, *Modified Fibrin Hydrogels stimulate Angiogenesis in vivo: potential Application to increase Perfusion of Ischemic Tissues.* Materialwissenschaft und Werkstofftechnik, 2005. **36**(12): p. 768-774.

55.   Discher, D.E., P. Janmey, and Y.-l. Wang, *Tissue Cells Feel and Respond to the Stiffness of Their Substrate.* Science, 2005. **310**(5751): p. 1139-1143.

56.   Zhang, Y.S. and A. Khademhosseini, *Advances in engineering hydrogels.* Science, 2017. **356**(6337).

57.   Bodugoz-Senturk, H., et al., *Poly(vinyl alcohol)–acrylamide hydrogels as load-bearing cartilage substitute.* Biomaterials, 2009. **30**(4): p. 589-596.

58.   Feinberg, A.W., *Biological Soft Robotics.* Annu Rev Biomed Eng, 2015. **17**: p. 243-65.

59.   Larson, C., et al., *Highly stretchable electroluminescent skin for optical signaling and tactile sensing.* Science, 2016. **351**(6277): p. 1071-1074.

60.   Yuan, M., et al., *Thermosensitive and photocrosslinkable hydroxypropyl chitin-based hydrogels for biomedical applications.* Carbohydrate Polymers, 2018. **192**: p. 10-18.

61.   Fan, H. and J.P. Gong, *Fabrication of Bioinspired Hydrogels: Challenges and Opportunities.* Macromolecules, 2020. **53**(8): p. 2769-2782.

62.   Chen, Y., et al., *Bioinspired Multiscale Wet Adhesive Surfaces: Structures and Controlled Adhesion.* Advanced Functional Materials, 2020. **30**(5): p. 1905287.

63.   Huang, W., et al., *Multiscale Toughening Mechanisms in Biological Materials and Bioinspired Designs.* Advanced Materials, 2019. **31**(43): p. 1901561.

64.   Liu, K. and L. Jiang, *Bio-inspired design of multiscale structures for function integration.* Nano Today, 2011. **6**(2): p. 155-175.

65.   Degtyar, E., et al., *The Mechanical Role of Metal Ions in Biogenic Protein-Based Materials.* Angewandte Chemie International Edition, 2014. **53**(45): p. 12026-12044.

66.   Grindy, S.C. and N. Holten-Andersen, *Bio-inspired metal-coordinate hydrogels with programmable viscoelastic material functions controlled by longwave UV light.* Soft Matter, 2017. **13**(22): p. 4057-4065.

67.   Grindy, S.C., et al., *Control of hierarchical polymer mechanics with bioinspired metal-coordination dynamics.* Nature Materials, 2015. **14**(12): p. 1210-1216.

68.   Harrington, M.J., et al., *Iron-Clad Fibers: A Metal-Based Biological Strategy for Hard Flexible Coatings.* Science, 2010. **328**(5975): p. 216-220.

69.   Holten-Andersen, N., et al., *pH-induced metal-ligand cross-links inspired by mussel yield self-healing polymer networks with near-covalent elastic moduli.* Proceedings of the National Academy of Sciences, 2011. **108**(7): p. 2651-2655.

70.   Tunn, I., M.J. Harrington, and K.G. Blank, *Bioinspired Histidine–Zn2+ Coordination for Tuning the Mechanical Properties of Self-Healing Coiled Coil Cross-Linked Hydrogels.* Biomimetics, 2019. **4**(1): p. 25.

71.   Pérez, C.M., A. Panitch, and J. Chmielewski, *A collagen peptide-based physical hydrogel for cell encapsulation.* Macromol Biosci, 2011. **11**(10): p. 1426-31.

72.   Stahl, P.J., et al., *PEG-Based Hydrogels with Collagen Mimetic Peptide-Mediated and Tunable Physical Cross-Links.* Biomacromolecules, 2010. **11**(9): p. 2336-2344.

73.   Radvar, E. and H.S. Azevedo, *Supramolecular Peptide/Polymer Hybrid Hydrogels for Biomedical Applications.* Macromolecular Bioscience, 2019. **19**(1): p. 1800221.

74.   Lin, C.C. and K.S. Anseth, *PEG hydrogels for the controlled release of biomolecules in regenerative medicine.* Pharm Res, 2009. **26**(3): p. 631-43.

75.   Hatakeyama, H., H. Akita, and H. Harashima, *The polyethyleneglycol dilemma: advantage and disadvantage of PEGylation of liposomes for systemic genes and nucleic acids delivery to tumors.* Biological & pharmaceutical bulletin, 2013. **36 6**: p. 892-9.

76.   Liu, G., et al., *Cytotoxicity study of polyethylene glycol derivatives.* RSC Advances, 2017. **7**(30): p. 18252-18259.

77.   Leoné, N., et al., *Improving Processing, Crystallization, and Performance of Poly-l-lactide with an Amide-Based Organic Compound as Both Plasticizer and Nucleating Agent.* ACS Omega, 2019. **4**(6): p. 10376-10387.

78.   Zacchigna, M., et al., *Multimeric, Multifunctional Derivatives of Poly(ethylene glycol).* Polymers, 2011. **3**(3): p. 1076-1090.

79.   Hamley, I.W., *PEG–Peptide Conjugates.* Biomacromolecules, 2014. **15**(5): p. 1543-1559.

80.   Hein, C.D., X.M. Liu, and D. Wang, *Click chemistry, a powerful tool for pharmaceutical sciences.* Pharm Res, 2008. **25**(10): p. 2216-30.

81.   Zhang, X., et al., *Physically and chemically dual-crosslinked hydrogels with superior mechanical properties and self-healing behavior.* New Journal of Chemistry, 2020. **44**(23): p. 9903-9911.

82.   Jing, P., et al., *Self-Assembling Peptide-Polymer Hydrogels Designed From the Coiled Coil Region of Fibrin.* Biomacromolecules, 2008. **9**(9): p. 2438-2446.

83.   Xu, Y. and M. Kirchner, *Collagen Mimetic Peptides.* Bioengineering (Basel, Switzerland), 2021. **8**(1): p. 5.

84.   Yu, S.M., Y. Li, and D. Kim, *Collagen mimetic peptides: progress towards functional applications.* Soft Matter, 2011. **7**(18): p. 7927-7938.

85.   Fletcher, J.M., et al., *A Basis Set of de Novo Coiled-Coil Peptide Oligomers for Rational Protein Design and Synthetic Biology.* ACS Synthetic Biology, 2012. **1**(6): p. 240-250.

86.   Dawson, W.M., et al., *Coiled coils 9-to-5: rational de novo design of α-helical barrels with tunable oligomeric states.* Chemical Science, 2021. **12**(20): p. 6923-6928.

87.   Gautieri, A., et al., *Hierarchical Structure and Nanomechanics of Collagen Microfibrils from the Atomistic Scale Up.* Nano Letters, 2011. **11**(2): p. 757-766.

88.   Fratzl, P., *Collagen : structure and mechanics.* 2010, New York: Springer.

89.   Brodsky, B., et al., *Triple-helical peptides: An approach to collagen conformation, stability, and self-association.* Biopolymers, 2008. **89**(5): p. 345-353.

90.   Okuyama, K., et al., *Helical twists of collagen model peptides.* Biopolymers, 2006. **84**(4): p. 421-32.

91.   Shoulders, M.D. and R.T. Raines, *Collagen structure and stability.* Annu Rev Biochem, 2009. **78**: p. 929-58.

92.   Shoulders, M.D., et al., *Stereoelectronic and steric effects in side chains preorganize a protein main chain.* Proc Natl Acad Sci U S A, 2010. **107**(2): p. 559-64.

93.   Boudko, S., et al., *Nucleation and propagation of the collagen triple helix in single-chain and trimerized peptides: transition from third to first order kinetics.* J Mol Biol, 2002. **317**(3): p. 459-70.

94.   Berisio, R., et al., *Crystal structure of the collagen triple helix model [(Pro-Pro-Gly)10]3.* Protein Science, 2002. **11**(2): p. 262-270.

95.   Bella, J., B. Brodsky, and H.M. Berman, *Hydration structure of a collagen peptide.* Structure, 1995. **3**(9): p. 893-906.

96.   Brodsky, B. and A.V. Persikov, *Molecular structure of the collagen triple helix.* Adv Protein Chem, 2005. **70**: p. 301-39.

97.   Berisio, R., et al., *Role of side chains in collagen triple helix stabilization and partner recognition.* J Pept Sci, 2009. **15**(3): p. 131-40.

98.   Persikov, A.V., et al., *Amino acid propensities for the collagen triple-helix.* Biochemistry, 2000. **39**(48): p. 14960-7.

99.   Persikov, A.V., J.A. Ramshaw, and B. Brodsky, *Prediction of collagen stability from amino acid sequence.* J Biol Chem, 2005. **280**(19): p. 19343-9.

100.   Persikov, A.V., J.A. Ramshaw, and B. Brodsky, *Collagen model peptides: Sequence dependence of triple-helix stability.* Biopolymers, 2000. **55**(6): p. 436-50.

101.   Beck, K. and B. Brodsky, *Supercoiled protein motifs: the collagen triple-helix and the alpha-helical coiled coil.* J Struct Biol, 1998. **122**(1-2): p. 17-29.

102.   Jaenicke, R. and H. Lilie, *Folding and association of oligomeric and multimeric proteins.* Adv Protein Chem, 2000. **53**: p. 329-401.

103.   Persikov, A.V., Y. Xu, and B. Brodsky, *Equilibrium thermal transitions of collagen model peptides.* Protein Sci, 2004. **13**(4): p. 893-902.

104.   Crick, F.H.C., *The packing of α-helices: simple coiled-coils.* Acta Crystallographica, 1953. **6**(8-9): p. 689-697.

105.   Pauling, L. and R.B. Corey, *Compound helical configurations of polypeptide chains: structure of proteins of the alpha-keratin type.* Nature, 1953. **171**(4341): p. 59-61.

106.   Bergues-Pupo, A.E., et al., *Trimeric coiled coils expand the range of strength, toughness and dynamics of coiled coil motifs under shear.* Physical Chemistry Chemical Physics, 2018. **20**(46): p. 29105-29115.

107.   Testa, O.D., E. Moutevelis, and D.N. Woolfson, *CC+: a relational database of coiled-coil structures.* Nucleic Acids Research, 2008. **37**(suppl_1): p. D315-D322.

108.   Wang, B., et al., *Keratin: Structure, mechanical properties, occurrence in biological organisms, and efforts at bioinspiration.* Progress in Materials Science, 2016. **76**: p. 229-318.

109.   Wasko, S., et al., *Structural Proteins from Whelk Egg Capsule with Long Range Elasticity Associated with a Solid-State Phase Transition.* Biomacromolecules, 2013. **15**.

110.   Surette, M.G. and J.B. Stock, *Role of α-Helical Coiled-coil Interactions in Receptor Dimerization, Signaling, and Adaptation during Bacterial Chemotaxis*.* Journal of Biological Chemistry, 1996. **271**(30): p. 17966-17973.

111.   Gillingham, A.K. and S. Munro, *Long coiled-coil proteins and membrane traffic.* Biochimica et biophysica acta, 2003. **1641 2-3**: p. 71-85.

112.   Petridou, N.I., Z. Spiró, and C.-P. Heisenberg, *Multiscale force sensing in development.* Nature Cell Biology, 2017. **19**(6): p. 581-588.

113.   Goktas, M., et al., *Molecular mechanics of coiled coils loaded in the shear geometry.* Chemical Science, 2018. **9**(20): p. 4610-4621.

114.   Apostolovic, B., M. Danial, and H.-A. Klok, *Coiled coils: attractive protein folding motifs for the fabrication of self-assembled, responsive and bioactive materials.* Chemical Society Reviews, 2010. **39**(9): p. 3541-3575.

115.   Moutevelis, E. and D.N. Woolfson, *A periodic table of coiled-coil protein structures.* J Mol Biol, 2009. **385**(3): p. 726-32.

116.   Fuchs, E. and K. Weber, *INTERMEDIATE FILAMENTS: Structure, Dynamics, Function and Disease.* Annual Review of Biochemistry, 1994. **63**(1): p. 345-382.

117.   Premchandar, A., et al., *Structural Dynamics of the Vimentin Coiled-coil Contact Regions Involved in Filament Assembly as Revealed by Hydrogen-Deuterium Exchange.* J Biol Chem, 2016. **291**(48): p. 24931-24950.

118.   Schliwa, M. and G. Woehlke, *Molecular motors.* Nature, 2003. **422**(6933): p. 759-765.

119.   Peckham, M., *Coiled coils and SAH domains in cytoskeletal molecular motors.* Biochem Soc Trans, 2011. **39**(5): p. 1142-8.

120.   Armony, G., et al., *Cross-linking reveals laminin coiled-coil architecture.* Proceedings of the National Academy of Sciences, 2016. **113**(47): p. 13384-13389.

121.   Pan, O.H. and K. Beck, *The C-terminal domain of matrilin-2 assembles into a three-stranded alpha-helical coiled coil.* J Biol Chem, 1998. **273**(23): p. 14205-9.

122. Kammerer, R.A., *Alpha-helical coiled-coil oligomerization domains in extracellular proteins.* Matrix Biol, 1997. **15**(8-9): p. 555-65; discussion 567-8.

123. Kammerer, R.A., et al., *Tenascin-C hexabrachion assembly is a sequential two-step process initiated by coiled-coil alpha-helices.* J Biol Chem, 1998. **273**(17): p. 10602-8.

124. Drobnak, I., et al., *Modulation of Coiled-Coil Dimer Stability through Surface Residues while Preserving Pairing Specificity.* Journal of the American Chemical Society, 2017. **139**(24): p. 8229-8236.

125. Woolfson, D.N., *The design of coiled-coil structures and assemblies.* Adv Protein Chem, 2005. **70**: p. 79-112.

126. Tunn, I., *From single molecules to bulk materials: tuning the viscoelastic properties of coiled coil cross-linked hydrogels.* 2020.

127. Mason, J.M., U.B. Hagemann, and K.M. Arndt, *Role of Hydrophobic and Electrostatic Interactions in Coiled Coil Stability and Specificity.* Biochemistry, 2009. **48**(43): p. 10380-10388.

128. Lupas, A.N. and M. Gruber, *The structure of alpha-helical coiled coils.* Adv Protein Chem, 2005. **70**: p. 37-78.

129. Pace, C.N. and J.M. Scholtz, *A helix propensity scale based on experimental studies of peptides and proteins.* Biophys J, 1998. **75**(1): p. 422-7.

130. Aronsson, C., et al., *Self-sorting heterodimeric coiled coil peptides with defined and tuneable self-assembly properties.* Scientific Reports, 2015. **5**(1): p. 14063.

131. Tunn, I., et al., *Tuning coiled coil stability with histidine-metal coordination.* Nanoscale, 2018. **10**(48): p. 22725-22729.

132. Reja, R.M., et al., *pH sensitive coiled coils: a strategy for enhanced liposomal drug delivery.* Nanoscale, 2016. **8**(9): p. 5139-5145.

133. Tang, A., et al., *The coiled coils in the design of protein-based constructs: hybrid hydrogels and epitope displays.* J Control Release, 2001. **72**(1-3): p. 57-70.

134. Morais, A.C. and S.T. Ferreira, *Folding and stability of a coiled-coil investigated using chemical and physical denaturing agents: comparative analysis of polymerized and non-polymerized forms of alpha-tropomyosin.* Int J Biochem Cell Biol, 2005. **37**(7): p. 1386-95.

135. Wood, C.W. and D.N. Woolfson, *CCBuilder 2.0: Powerful and accessible coiled-coil modeling.* Protein Sci, 2018. **27**(1): p. 103-111.

136. Xia, Y., et al., *Printable Fluorescent Hydrogels Based on Self-Assembling Peptides.* Scientific Reports, 2017. **7**(1): p. 9691.

137. Davis, D.A., et al., *Force-induced activation of covalent bonds in mechanoresponsive polymeric materials.* Nature, 2009. **459**(7243): p. 68-72.

138. Lyu, S., et al., *Optically controlled reversible protein hydrogels based on photoswitchable fluorescent protein Dronpa.* Chemical Communications, 2017. **53**(100): p. 13375-13378.

139. Matcham, S. and K. Novakovic, *Fluorescence Imaging in Genipin Crosslinked Chitosan⁻Poly(vinyl pyrrolidone) Hydrogels.* Polymers (Basel), 2016. **8**(11).

140. Bruns, N., et al., *Mechanical nanosensor based on FRET within a thermosome: damage-reporting polymeric materials.* Angew Chem Int Ed Engl, 2009. **48**(31): p. 5666-9.

141. Brantley, J.N., et al., *Mechanically modulating the photophysical properties of fluorescent protein biocomposites for ratio- and intensiometric sensors.* Angew Chem Int Ed Engl, 2014. **53**(20): p. 5088-92.

142. Merindol, R., et al., *Modular Design of Programmable Mechanofluorescent DNA Hydrogels.* Nature Communications, 2019. **10**(1): p. 528.

143. Lovell, J.F., et al., *Porphyrin-Cross-Linked Hydrogel for Fluorescence-Guided Monitoring and Surgical Resection.* Biomacromolecules, 2011. **12**(9): p. 3115-3118.

144. Wu, L., et al., *Förster resonance energy transfer (FRET)-based small-molecule sensors and imaging agents.* Chemical Society Reviews, 2020. **49**(15): p. 5110-5139.

145. Zhuang, X., et al., *Fluorescence quenching: A tool for single-molecule protein-folding study.* Proceedings of the National Academy of Sciences, 2000. **97**(26): p. 14241-14244.

146. Sun, X., et al., *Colorimetric and fluorometric monitoring of the helix composition of collagen-like peptides at the nM level.* Chemical Communications, 2016. **52**(15): p. 3107-3110.

147. Gröger, K., G. Gavins, and O. Seitz, *Strand Displacement in Coiled-Coil Structures: Controlled Induction and Reversal of Proximity.* Angewandte Chemie International Edition, 2017. **56**(45): p. 14217-14221.

148. Li, Y.-H., J.-C. Yue, and G.-P. Cai, *Fluorescence characterization of type I collagen from normal and silicotic rats and its quenching dynamics induced by hypocrellin B.* Biopolymers, 1997. **42**(2): p. 219-226.

149. Odetti, P.R., A. Borgoglio, and R. Rolandi, *Age-related increase of collagen fluorescence in human subcutaneous tissue.* Metabolism, 1992. **41**(6): p. 655-8.

150. Bennink, L.L., et al., *High Serum Stability of Collagen Hybridizing Peptides and Their Fluorophore Conjugates.* Mol Pharm, 2017. **14**(6): p. 1906-1915.

151. Nian, L., et al., *Fluorescence self-quenching assay for the detection of target collagen sequences using a short probe peptide.* Talanta, 2018. **176**: p. 492-498.

152. Wei, W., et al., *Highly specific recognition of denatured collagen by fluorescent peptide probes with the repetitive Gly-Pro-Pro and Gly-Hyp-Hyp sequences.* Journal of Materials Chemistry B, 2020. **8**(44): p. 10093-10100.

153. Aronoff, M.R., et al., *Imaging and targeting LOX-mediated tissue remodeling with a reactive collagen peptide.* Nature Chemical Biology, 2021. **17**(8): p. 865-871.

154. Sun, X., et al., *Luminescent Biofunctional Collagen Mimetic Nanofibers.* ACS Omega, 2019. **4**(15): p. 16270-16279.

155. Ma, W., et al., *A Cell Membrane-Targeting Self-Delivery Chimeric Peptide for Enhanced Photodynamic Therapy and In Situ Therapeutic Feedback.* Advanced Healthcare Materials, 2020. **9**(1): p. 1901100.

156. Skrzeszewska, P.J., et al., *Physical gels of telechelic triblock copolymers with precisely defined junction multiplicity.* Soft Matter, 2009. **5**(10): p. 2057-2062.

157. Jia, X. and K.L. Kiick, *Hybrid Multicomponent Hydrogels for Tissue Engineering.* Macromolecular Bioscience, 2009. **9**(2): p. 140-156.

158. Lee, H.J., et al., *Collagen mimetic peptide-conjugated photopolymerizable PEG hydrogel.* Biomaterials, 2006. **27**(30): p. 5268-76.

159. Wang, C., J. Kopeček, and R.J. Stewart, *Hybrid Hydrogels Cross-Linked by Genetically Engineered Coiled-Coil Block Proteins.* Biomacromolecules, 2001. **2**(3): p. 912-920.

160. Yang, J., et al., *Refolding hydrogels self-assembled from N-(2-hydroxypropyl)methacrylamide graft copolymers by antiparallel coiled-coil formation.* Biomacromolecules, 2006. **7**(4): p. 1187-1195.

161. Dušek, K., et al., *Coiled-Coil Hydrogels. Effect of Grafted Copolymer Composition and Cyclization on Gelation.* Macromolecules, 2009. **42**(6): p. 2265-2274.

162. Coin, I., M. Beyermann, and M. Bienert, *Solid-phase peptide synthesis: from standard procedures to the synthesis of difficult sequences.* Nature Protocols, 2007. **2**(12): p. 3247-3256.

163. Merrifield, R.B., *Solid Phase Peptide Synthesis. I. The Synthesis of a Tetrapeptide.* Journal of the American Chemical Society, 1963. **85**(14): p. 2149-2154.

164. Atherton, E., D.L.J. Clive, and R.C. Sheppard, *Polyamide supports for polypeptide synthesis.* Journal of the American Chemical Society, 1975. **97**(22): p. 6584-6585.

165. Bayer, E., *Towards the Chemical Synthesis of Proteins.* Angewandte Chemie International Edition in English, 1991. **30**(2): p. 113-129.

166. Carpino, L.A., *Oxidative Reactions of Hydrazines. II. Isophthalimides. New Protective Groups on Nitrogen1,2.* Journal of the American Chemical Society, 1957. **79**(1): p. 98-101.

167. Carpino, L.A. and G.Y. Han, *9-Fluorenylmethoxycarbonyl function, a new base-sensitive amino-protecting group.* Journal of the American Chemical Society, 1970. **92**(19): p. 5748-5749.

168. Amblard, M., et al., *Methods and protocols of modern solid phase Peptide synthesis.* Mol Biotechnol, 2006. **33**(3): p. 239-54.

169. STORY, S.C. and J.V. ALDRICH, *Side-product formation during cyclization with HBTU on a solid support.* International Journal of Peptide and Protein Research, 1994. **43**(3): p. 292-296.

170. Fields, G.B.S.M., *Peptide characterization and application protocols.* 2007, Totowa: Humana Press.

171. Hillenkamp, F.K.M.B.R.C.C.B.T., *Matrix-Assisted Laser Desorption/Ionization Mass Spectrometry of Biopolymers.* Anal. Chem. Analytical Chemistry, 1991. **63**(24): p. 1193A-1203A.

172. Tanaka, K., et al., *Protein and polymer analyses up to m/z 100 000 by laser ionization time-of-flight mass spectrometry.* Rapid Communications in Mass Spectrometry, 1988. **2**(8): p. 151-153.

173. Wiley, W.C. and I.H. McLaren, *Time-of-Flight Mass Spectrometer with Improved Resolution.* Review of Scientific Instruments, 1955. **26**(12): p. 1150-1157.

174. Beychok, S., *Circular Dichroism of Biological Macromolecules.* Science, 1966. **154**(3754): p. 1288-1299.

175. Johnson, W.C., Jr., *Protein secondary structure and circular dichroism: a practical guide.* Proteins, 1990. **7**(3): p. 205-14.

176. Kelly, S.M., T.J. Jess, and N.C. Price, *How to study proteins by circular dichroism.* Biochim Biophys Acta, 2005. **1751**(2): p. 119-39.

177. Greenfield, N.J., *Using circular dichroism collected as a function of temperature to determine the thermodynamics of protein unfolding and binding interactions.* Nature protocols, 2006. **1**(6): p. 2527-2535.

178. Greenfield, N.J., *Analysis of the kinetics of folding of proteins and peptides using circular dichroism.* Nature Protocols, 2006. **1**(6): p. 2891-2899.

179. Greenfield, N.J. and S.E. Hitchcock-Degregori, *Conformational intermediates in the folding of a coiled-coil model peptide of the N-terminus of tropomyosin and αα-tropomyosin.* Protein Science, 1993. **2**(8): p. 1263-1273.

180. Lakowicz, J.R., *Principles of fluorescence spectroscopy.* 2016.

181. Chen, H. and E. Rhoades, *Fluorescence characterization of denatured proteins.* Current opinion in structural biology, 2008. **18 4**: p. 516-24.

182. Hajighasem, A. and K. Kabiri, *Cationic highly alcohol-swellable gels: synthesis and characterization.* Journal of Polymer Research, 2013. **20**(8): p. 218.

183. Murata, H., et al., *Dynamic viscoelastic properties and the age changes of long-term soft denture liners.* Biomaterials, 2000. **21**(14): p. 1421-1427.

184. Grad, E.M., et al., *Influence of Network Topology on the Viscoelastic Properties of Dynamically Crosslinked Hydrogels.* Frontiers in Chemistry, 2020. **8**(536).

185. Williams, G. and D.C. Watts, *Non-symmetrical dielectric relaxation behaviour arising from a simple empirical decay function.* Transactions of the Faraday Society, 1970. **66**(0): p. 80-85.

186. Kar, K., et al., *Self-association of collagen triple helic peptides into higher order structures.* J Biol Chem, 2006. **281**(44): p. 33283-90.

187. Senff, H. and W. Richtering, *Influence of cross-link density on rheological properties of temperature-sensitive microgel suspensions.* Colloid and Polymer Science, 2000. **278**(9): p. 830-840.

188. Berry, G.C. and D.J. Plazek, *On the use of stretched-exponential functions for both linear viscoelastic creep and stress relaxation.* Rheologica Acta, 1997. **36**(3): p. 320-329.

189. Ren, Y., et al., *A collagen mimetic peptide-modified hyaluronic acid hydrogel system with enzymatically mediated degradation for mesenchymal stem cell differentiation.* Materials Science and Engineering: C, 2020. **108**: p. 110276.

190. Mehta, M., et al., *The collagen I mimetic peptide DGEA enhances an osteogenic phenotype in mesenchymal stem cells when presented from cell-encapsulating hydrogels.* Journal of Biomedical Materials Research Part A, 2015. **103**(11): p. 3516-3525.

191. Lee, H.J., et al., *Enhanced Chondrogenesis of Mesenchymal Stem Cells in Collagen Mimetic Peptide-Mediated Microenvironment.* Tissue Engineering Part A, 2008. **14**(11): p. 1843-1851.

192. Yao, M.-H., et al., *Polypeptide-engineered physical hydrogels designed from the coiled-coil region of cartilage oligomeric matrix protein for three-dimensional cell culture.* Journal of Materials Chemistry B, 2014. **2**(20): p. 3123-3132.

193. Rudra, J.S., et al., *Immune responses to coiled coil supramolecular biomaterials.* Biomaterials, 2010. **31**(32): p. 8475-8483.

194. Cipelletti, L. and L. Ramos, *Slow dynamics in glasses, gels and foams.* Current Opinion in Colloid and Interface Science, 2002. **7**: p. 228-234.

195. László, K., et al., *Kinetics of Jammed Systems: PNIPA Gels.* Macromolecular Symposia, 2011. **306-307**(1): p. 27-32.

196. Rogers, M.C., et al., *Microscopic signatures of yielding in concentrated nanoemulsions under large-amplitude oscillatory shear.* Physical Review Materials, 2018. **2**(9): p. 095601.

197. Falus, P., et al., *Crossover from Stretched to Compressed Exponential Relaxations in a Polymer-Based Sponge Phase.* Physical Review Letters, 2006. **97**(6): p. 066102.

198. Lange, F., et al., *Connectivity and Structural Defects in Model Hydrogels: A Combined Proton NMR and Monte Carlo Simulation Study.* Macromolecules, 2011. **44**(24): p. 9666-9674.

199. Deng, L., et al., *Fast and slow dynamics of the cytoskeleton.* Nat Mater, 2006. **5**(8): p. 636-40.

200. Mulla, Y., F.C. MacKintosh, and G.H. Koenderink, *Origin of Slow Stress Relaxation in the Cytoskeleton.* Physical Review Letters, 2019. **122**(21): p. 218102.

201. Sakai, T., et al., *Design and Fabrication of a High-Strength Hydrogel with Ideally Homogeneous Network Structure from Tetrahedron-like Macromonomers.* Macromolecules, 2008. **41**(14): p. 5379-5384.

202. López-García, P., et al., *Fortified Coiled Coils: Enhancing Mechanical Stability with Lactam or Metal Staples.* Angewandte Chemie International Edition in English, 2020. **133**.

203. Kawamoto, K., et al., *Dual Role for 1,2,4,5-Tetrazines in Polymer Networks: Combining Diels–Alder Reactions and Metal Coordination To Generate Functional Supramolecular Gels.* ACS Macro Letters, 2015. **4**(4): p. 458-461.

204. Quinn, S.D., et al., *Real-time probing of β-amyloid self-assembly and inhibition using fluorescence self-quenching between neighbouring dyes.* Molecular BioSystems, 2014. **10**(1): p. 34-44.

205. Garai, K. and C. Frieden, *Quantitative analysis of the time course of Aβ oligomerization and subsequent growth steps using tetramethylrhodamine-labeled Aβ.* Proceedings of the National Academy of Sciences, 2013. **110**(9): p. 3321-3326.

206. Mizuno, K., et al., *Kinetic hysteresis in collagen folding.* Biophysical journal, 2010. **98**(12): p. 3004-3014.

207. Lieleg, O., et al., *Slow dynamics and internal stress relaxation in bundled cytoskeletal networks.* Nature Materials, 2011. **10**(3): p. 236-242.

List of figures

117

List of tables

Appendix

Table of contents

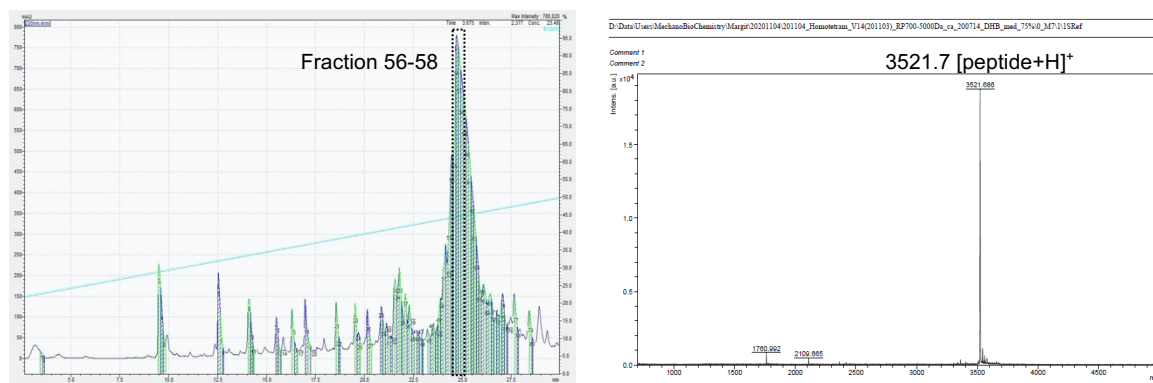### List of supplementary figures

List of supplementary tables

Figure S1. Synthesis and purification information of the CC peptides. A Preparative HPLC chromatogram of the CC-Homo2 (left) and the representative MALDI-TOF spectrum of the purest fraction (right) assigned in the HPLC chromatogram with black dotted box. **B** Preparative HPLC chromatogram of the CC-Homo3 (left) and the representative MALDI-TOF spectrum of the purest fraction (right). **C** Preparative HPLC chromatogram of the CC-Homo4 (left) and the representative MALDI-TOF spectrum of the purest fraction (right). The purification condition in HPLC and the measurement condition of MALDI-TOF were described in the **Methods**.
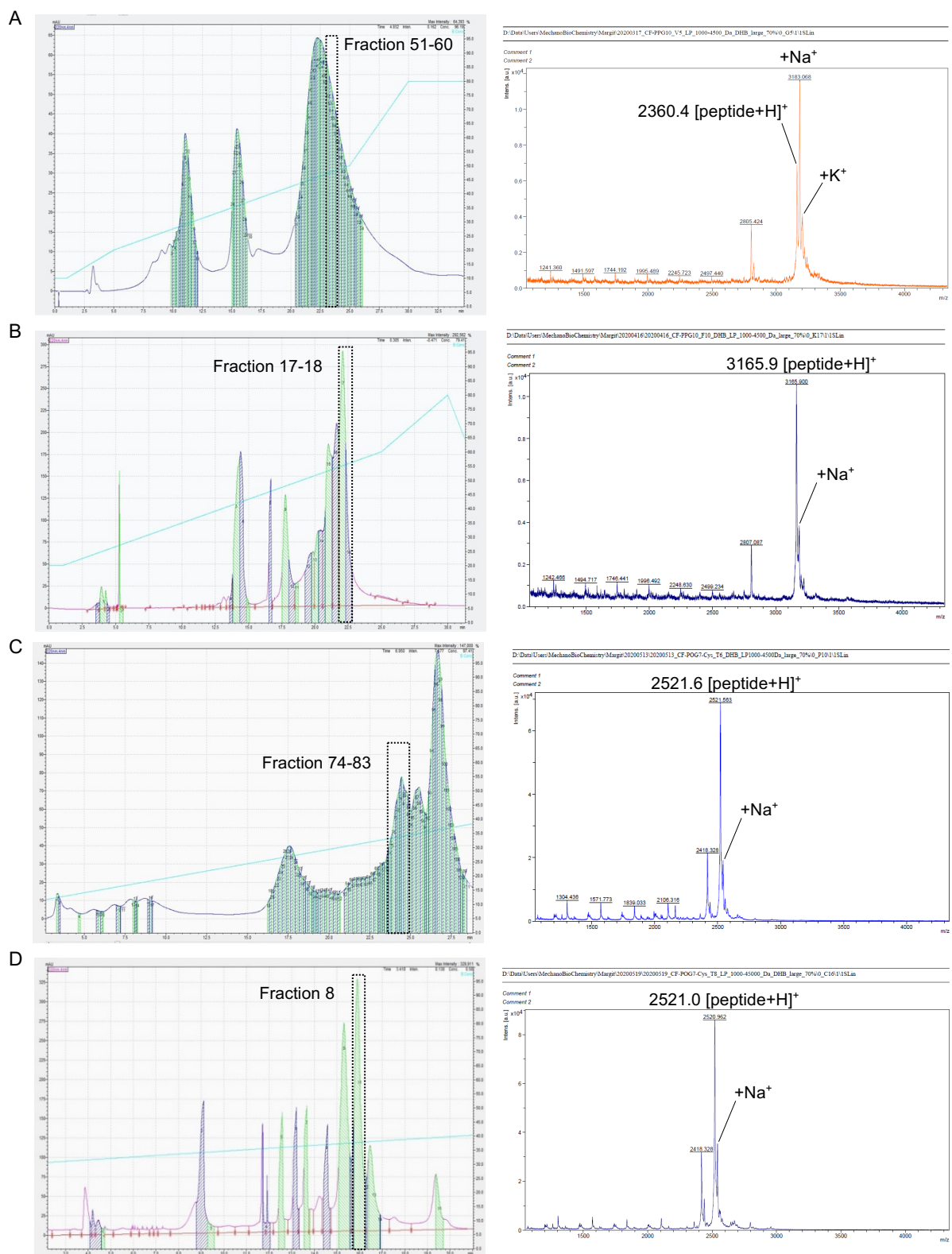
Figure S2. Synthesis and purification information of the CF-labeled CMPs. A Preparative HPLC chromatogram of the CF-(PPG)$_{10}$ peptide (left) and the representative MALDI-TOF spectrum of the purest fraction (right) assigned with black box in the HPLC chromatogram. **B** Analytical HPLC chromatogram of the CF-(PPG)$_{10}$ peptide (left) and the representative MALDI-TOF spectrum of the purest fraction (right). **C** Preparative HPLC chromatogram of the CF-(POG)$_7$ peptide (left) and the representative MALDI-TOF spectra of the purest fraction (right). **D** Analytical HPLC chromatogram of the CF-(POG)$_7$ peptide (left) and the representative MALDI-TOF spectrum of the purest fraction (right). The purification condition of HPLC and the measurement condition of MALDI-TOF were described in the **Methods**.
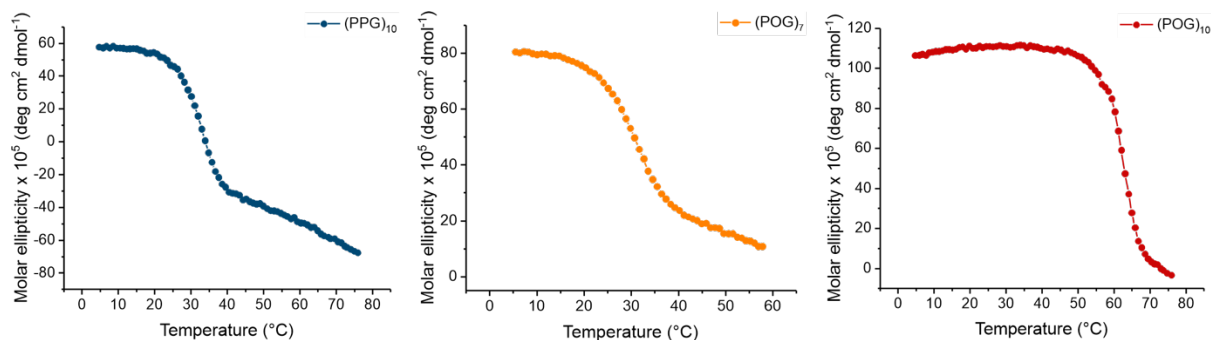
Figure S3. CD thermal denaturation curves of the CMPs. CD spectra of the $(PPG)_{10}$ (dark blue), $(POG)_7$ (orange), and $(POG)_{10}$ (dark red) peptides were measured with a temperature range from 4-60 °C for $(POG)_7$ and 4-80 °C for $(PPG)_{10}$ and $(POG)_{10}$ for the thermal denaturation measurements of each peptide. The molar ellipticities at 225 nm which is assigned for collagen triple helical structure in CD spectroscopy were plotted with the temperature. The molar ellipticities were calculated from the measured ellipticities in mdeg as described in **Methods**.
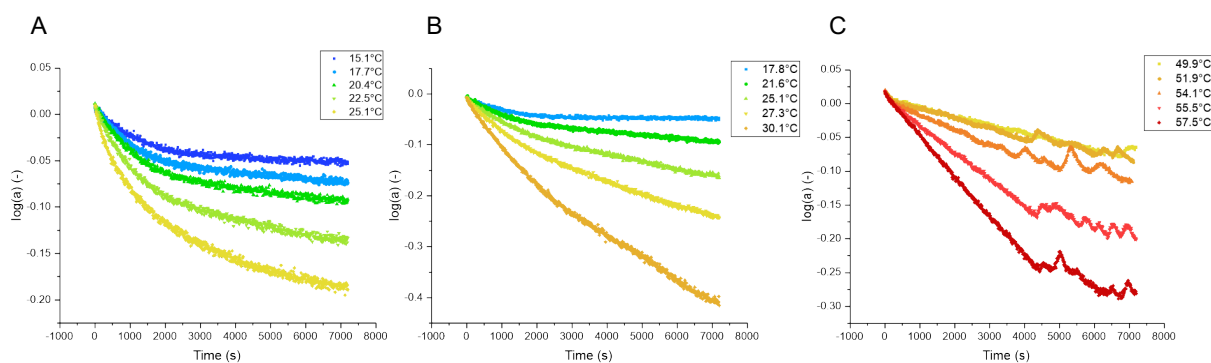
Figure S4. Plots of fraction folded (logarithmic) vs. time (linear) obtained from the CD temperature-jump experiments of $(PPG)_{10}$ (A), $(POG)_7$ (B) and $(POG)_{10}$ (C). The CMPs solutions were prepared in borate buffer (pH 8.9) with a concentration of 1 mg mL^{-1}. The initial linear range from 5-60 min depending on the CMPs was used to obtain the apparent unfolding (dissociation) rates through the linear regression.

125
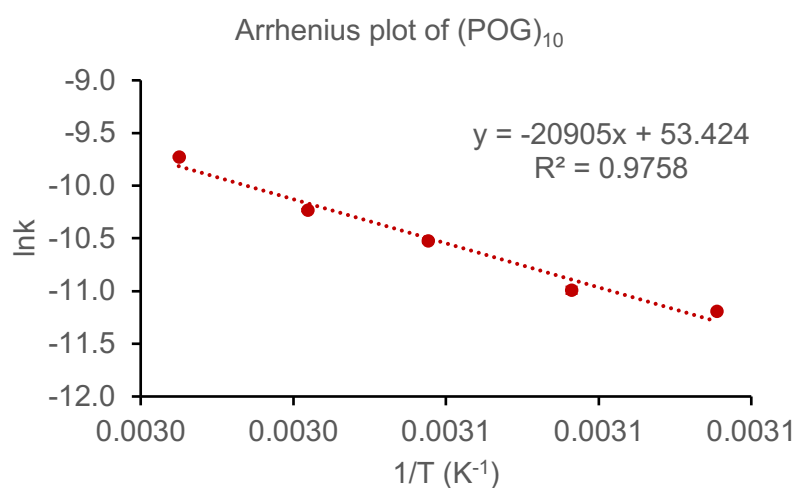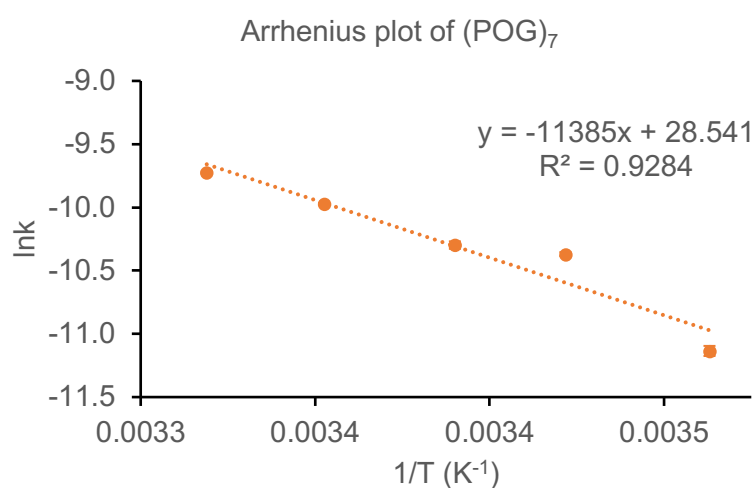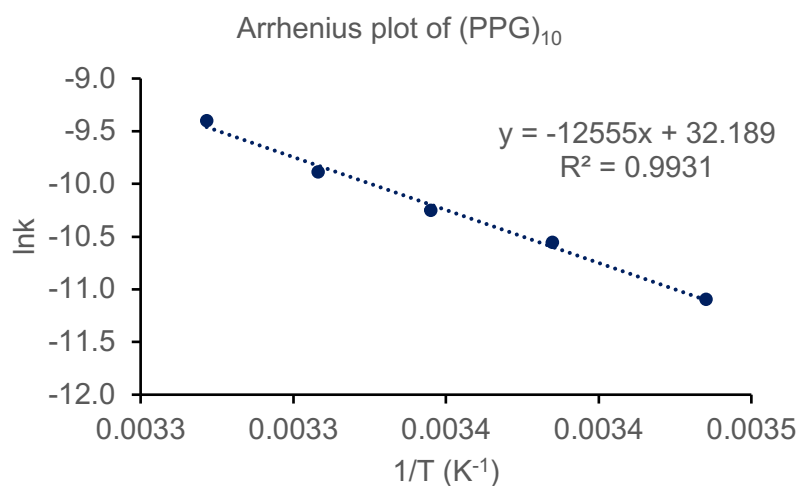
Figure S5. Arrhenius plots of the CMPs. The Arrhenius plots were obtained with the ln(apparent dissociation rates) vs. T^{-1} from the CD temperature-jump experiments (**Figure S4, Table S3**). The activation energies were obtained from the slope of the plots (E_a = -slope/R, when R is gas constant). Error bars represent standard errors.
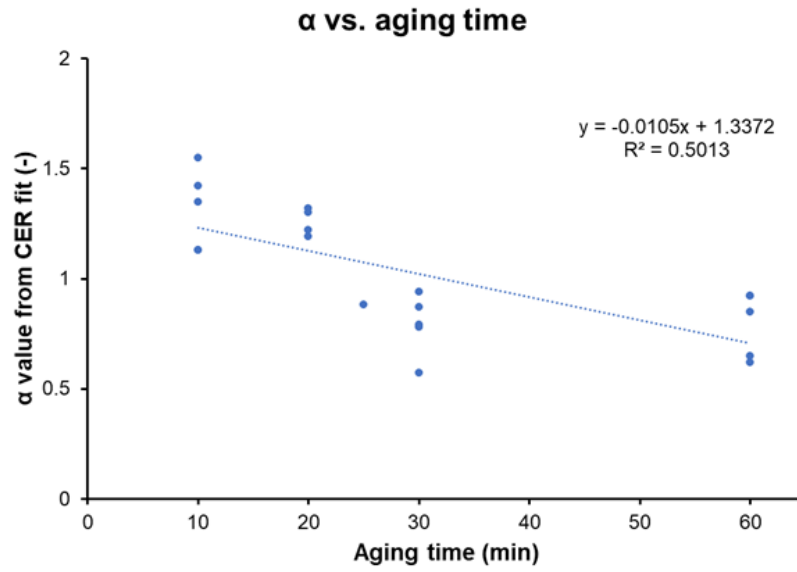
Figure S6. Relationship of the relaxation exponents and the aging times (waiting times) of the (POG)$_{10}$ hydrogels. The five data sets of the stress relaxation tests of the (POG)$_{10}$ hydrogels were used for the analysis (**Table S5**). Fitting parameters were obtained using the KWW equation.
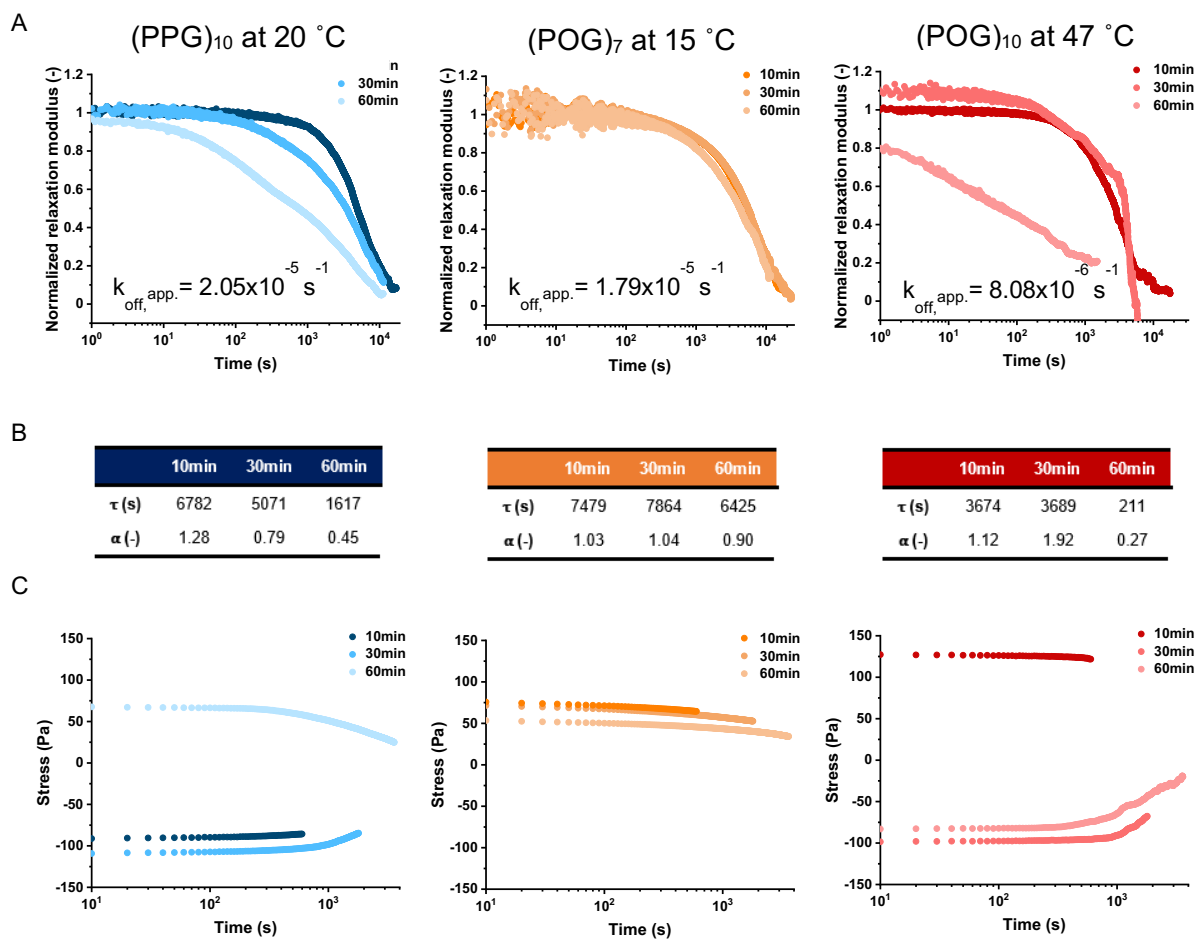
Figure S7. Temperature-controlled stress relaxation tests of the CMP-crosslinked hydrogels measured at the temperatures when the fraction folded values are 0.99. A Relaxation curves from the stress relaxation tests with the standard zero-strain waiting time method. The $(PPG)_{10}$ hydrogels (blue) and the $(POG)_7$ hydrogels (orange) were measured at 20 °C and 15 °C, respectively. The $(POG)_{10}$ hydrogels (red) were measured at 47 °C. Apparent dissociation rate constants ($k_{off,}^{app.}$) at each temperature were calculated from the Arrhenius curves of the CMPs (**Figure S5**) using interpolation or extrapolation. **B** Relaxation times and fitting parameters obtained using the KWW equation. **C** Relaxation of stress applied from the amplitude sweep was monitored during waiting time of 10, 30, and 60 min.
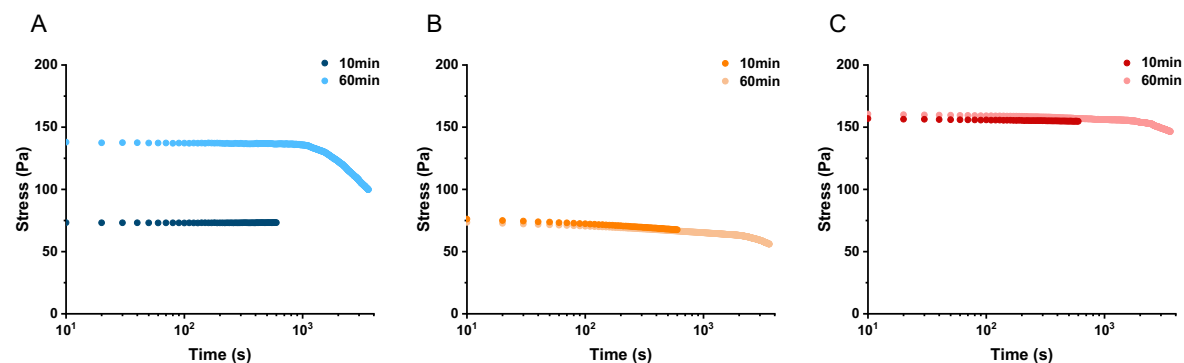
Figure S8. Relaxation of the stresses of the CMPs during the waiting time in the temperature-controlled stress relaxation tests measured at 5°C. Relaxation of the stress applied from the amplitude sweep was shown for the $(PPG)_{10}$- (**A**, blue), the $(POG)_7$- (**B**, orange) and the $(POG)_{10}$- (**C**, red) crosslinked hydrogels with waiting times of 10 and 60 min.

128
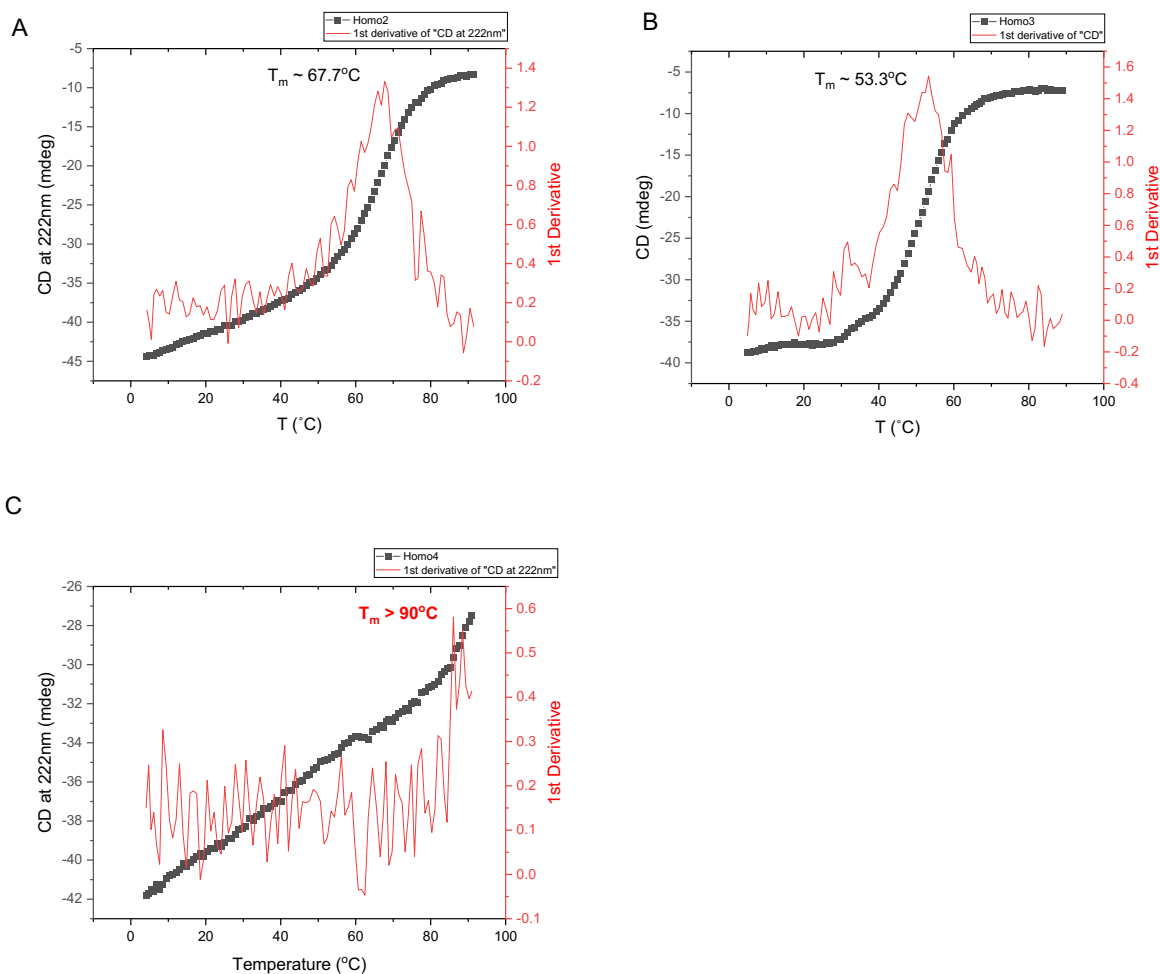
Figure S9. CD thermal denaturation curves and the first derivatives of the CC-Homo2 (A), CC-Homo3 (B), and CC-Homo4 (C). The thermal denaturation measurements were performed in a temperature range from 4-90 ˚C with heating rate of 1 ˚C min⁻¹. The first derivatives of the raw measurement curves were obtained using Origin Pro 2020 (OriginLab Corporation) and the melting temperatures were obtained from the peaks of the first derivative curves. CC-Homo2 had T_m of 67.7˚C and CC-Homo3 showed T_m at 53.3 ˚C, however, CC-homo4 did not show any transition until 99 ˚C, which indicates T_m of CC-Homo4 is higher than 90 ˚C. These melting temperatures can be compared to the values obtained using Global 3 software in **Table S6**.
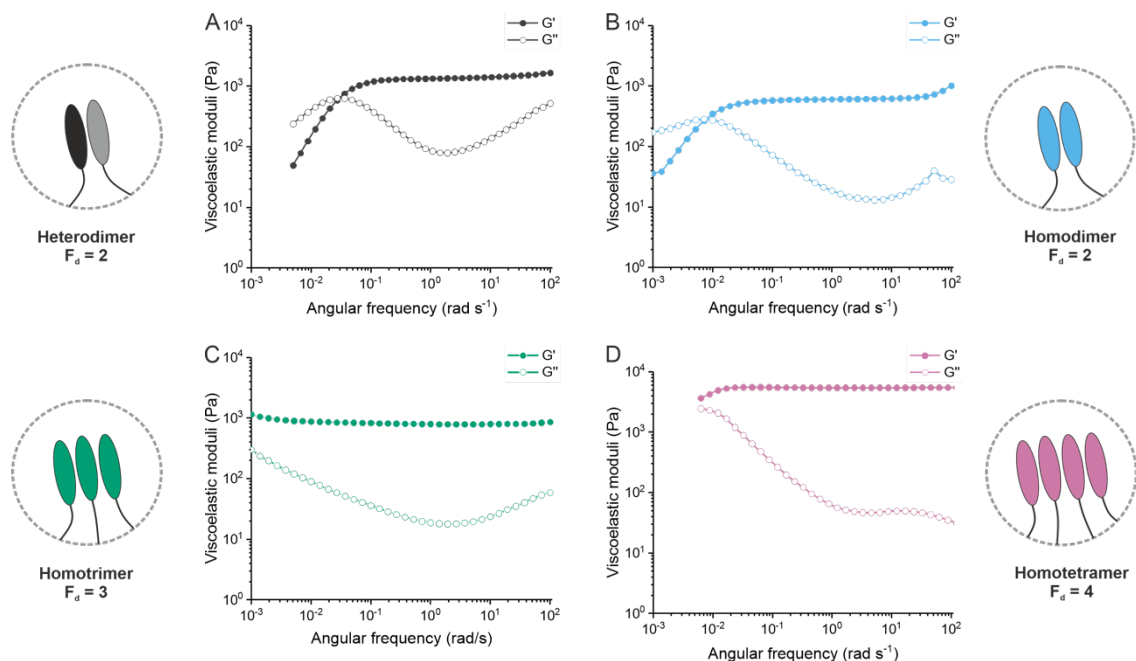
Figure S10. Representative frequency sweeps of the CC-crosslinked hydrogels. Frequency sweeps of the CC-Hetero2 (A, dark gray), CC-Homo2 (B, sky blue), CC-Homo3 (C, bluish green) and CC-Homo4 (D, reddish purple) were shown. The frequency ranges were varied from 100 rad s^{-1} to 0.005 rad s^{-1} when the oscillatory strain amplitude was applied constantly at 1 % for the CC-Heter2 and the CC-Homo4 hydrogels. The frequency ranges were varied from 100 rad s^{-1} to 0.001 rad s^{-1} with a constant strain amplitude of 1 % for the CC-Homo2 and the CC-Homo3 hydrogels. The frequency sweeps were performed starting from the higher frequency to the lower frequency.
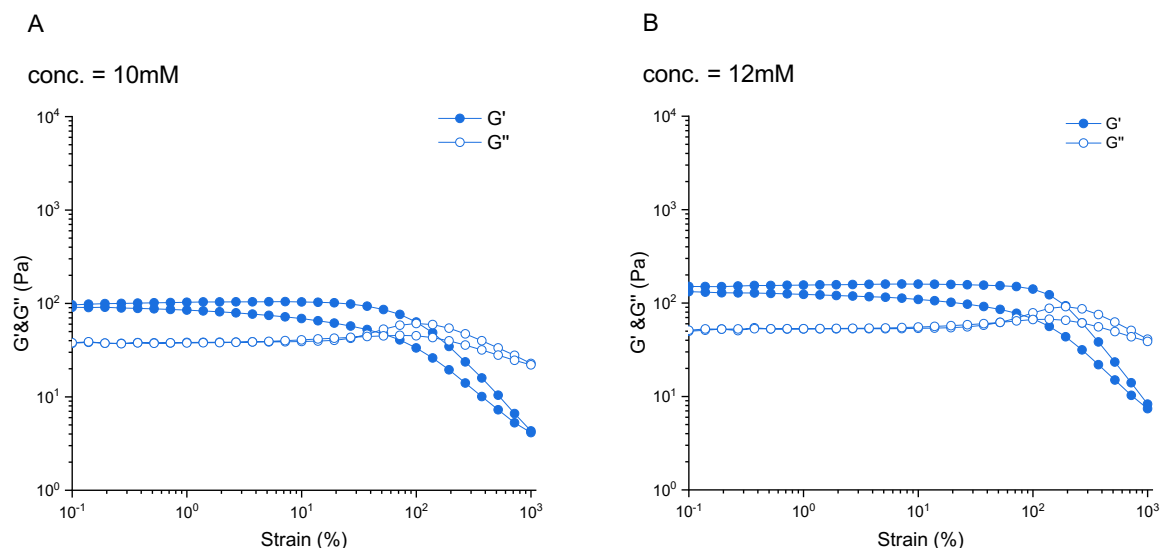
Figure S11. Amplitude sweeps of the CC-Homo3 coupled with the 2-arm linear-PEG hydrogels with higher concentrations. CC-Homo3 with a concentration of 10 mM (**A**) and the CC-Homo3 with a concentration of 12 mM (**B**) were used for the hydrogel preparations. The concentration of the linear PEG was used with the stoichiometric ratio of 1:1 between the thiol groups at the N-termini of the peptides and the maleimide groups at the end of the PEG arms. Amplitude sweeps were performed with strain amplitudes were varied from 0.1 % to 1000 % for ascending and descending sweeps both when the angular frequency was set as 10 rad s^{-1}. The sweeps were repeated two times and the second sweep was shown.
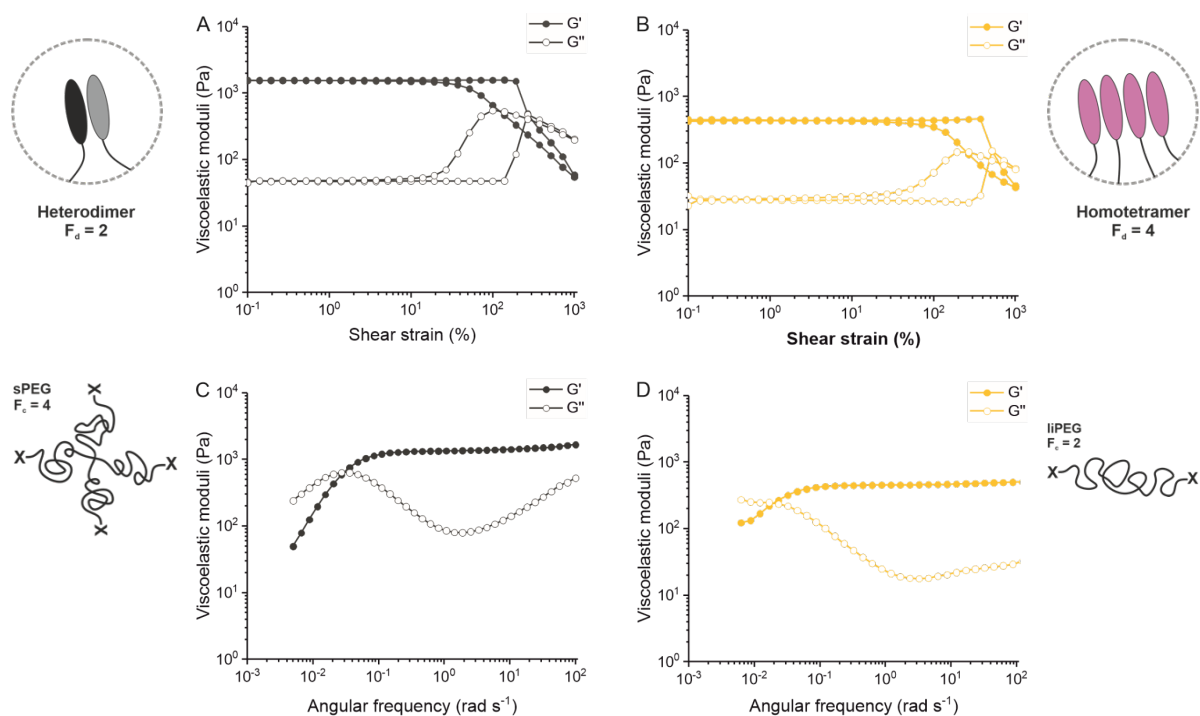
130

Figure S12. Amplitude sweeps and frequency sweeps of the CC-Homo4 coupled with the linear-PEG hydrogels (A and C) and the CC-Hetero2 with the star-PEG hydrogels (B and D). Amplitude sweeps of the CC-Hetero2 with the star-PEG network (**A**) and the CC-Homo4 with the linear-PEG combination (**B**) were performed with stain amplitudes range from 0.1 % to 1000 % with a constant angular frequency of 10 rad s^{-1}. Frequency sweeps of the CC-Hetero2 with the star-PEG network (**C**) and the CC-Homo4 with linear-PEG network (**D**) were performed with frequency range from 100 rad s^{-1} to 0.005 rad s^{-1} with a constant strain amplitude of 1 %.
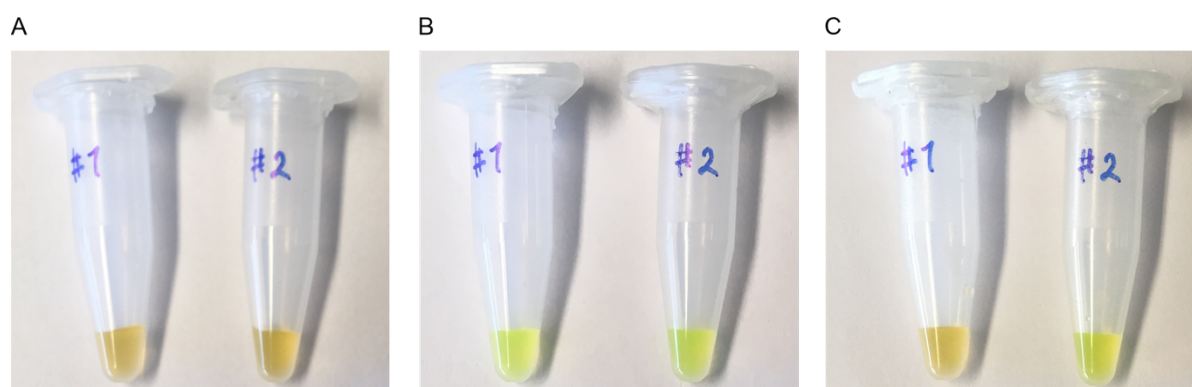
Figure S13. Visual color change in the CF-(POG)$_7$ peptide solutions mixed with buffer solution as a control (labeled as #1 on the tubes, left) and with the unlabeled (POG)$_{10}$ peptide solution as a competitor (labeled as #2, right). The solutions were prepared at room temperature (**A**) and heated at 70 °C for thermal denaturation for 20 min (**B**) and cooled down at 4 °C for re-equilibration for 3 days (**C**).

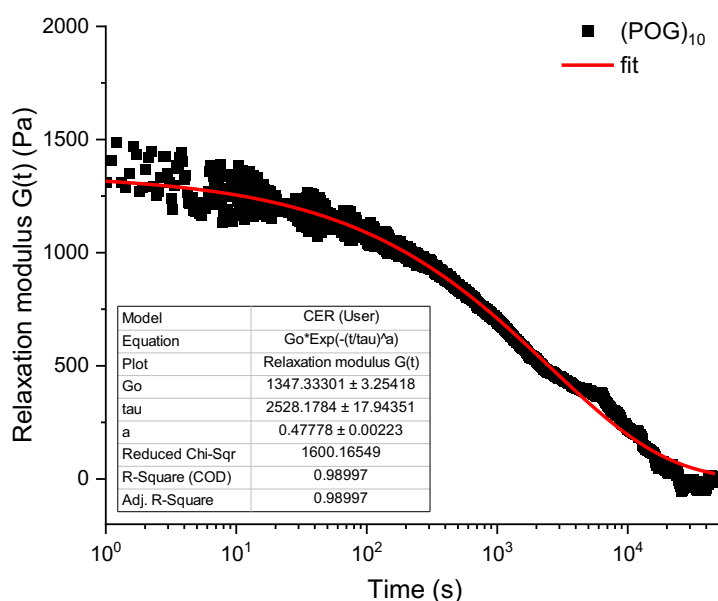| Model	CER (User)
Equation	Go*Exp(-(t/tau)^a)
Plot	Relaxation modulus G(t)
Go	1347.33301 ± 3.25418
tau	2528.1784 ± 17.94351
a	0.47778 ± 0.00223
Reduced Chi-Sqr	1600.16549
R-Square (COD)	0.98997
Adj. R-Square	0.98997

Figure S14. Stress relaxation test of the (POG)$_{10}$-crosslinked hydrogels prepared on rheometer for a gelation without external mechanical perturbation. The (POG)$_{10}$ peptide solution with a concentration of 6 mM was mixed with the 4-arm star-shaped PEG polymer (40 kDa, NHS functionalization) in a Eppendorf tube and quickly transferred on rheometer before a gelation. The gelation occurred for 3 h without any mechanical history except a possibility of internal stress during the network formation on the rheometer. For the stress relaxation test, a strain of 5 % was applied in a stepwise manner and relaxation modulus G(t) was monitored as a function of time. The KWW equation was used for exponential fitting. The relaxation time ("tau" in the fitting table) was about 2,528 s, which was much smaller compared to those of the (POG)$_{10}$-crosslinked hydrogels prepared in Eppendorf tube as the standard method. The relaxation exponent ("a" in the fitting table) showed smaller value of 0.48 with more stretched shape of the curve compared to the the (POG)$_{10}$-crosslinked hydrogels with the standard preparation method.
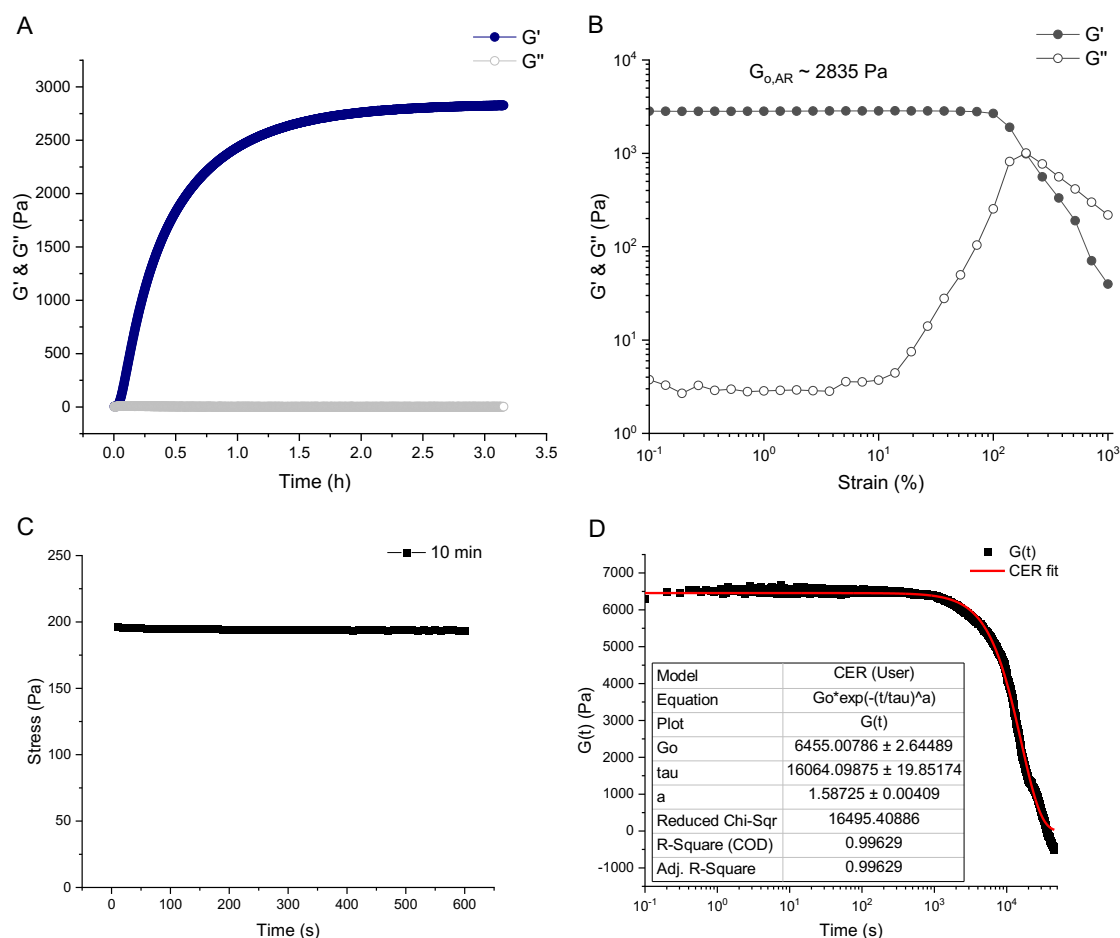
Figure S15. Stress relaxation test of the (POG)₁₀-crosslinked hydrogels prepared on a rheometer for a gelation with the standard measurement protocol. A Time sweeps were performed with an oscillatory strain amplitude of 0.1 % for about 3 h, monitoring G' and G" after the (POG)$_{10}$ peptide solution (6 mM) was mixed with the 4-arm star-shaped PEG polymer and immediately transferred on a rheometer. After 3 h, the G' value seems to reach to the plateau with the plateau modulus around 2,830 Pa. **B** Successive amplitude sweeps with oscillatory strain amplitudes from 0.1 % to 1000 % (ω = 10 rad s^{-1}) were performed. The plateau modulus in the LVE region was 2,835 Pa and the yield strain and flow point were relatively similar with those of the (POG)$_{10}$-crosslinked hydrogels prepared with the standard sample preparation method. **C** After waiting time with zero-strain setup for 10 min and **D** stress relaxation test was performed with a step-strain of 5 % and the relaxation modulus was recorded over time. The relaxation parameters were obtained using the KWW equation.
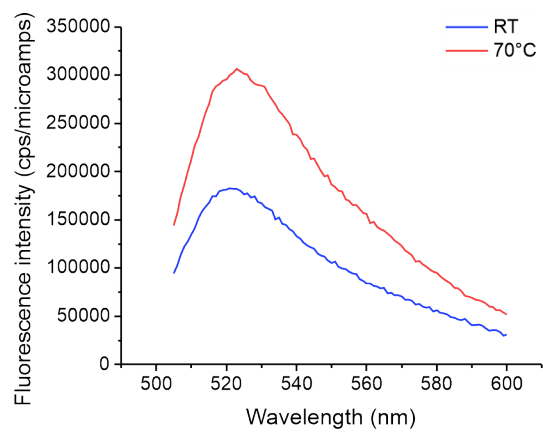
Figure S16. Fluorescence emission spectra obtained after a week of kinetics measurements. Emission spectrum was obtained after finishing a week of kinetics measurements (**Figure 37**) at RT (blue). Then, temperature increased to 70 ˚C and the emission spectrum was measured again (red). The fluorescence intensity increased about 2 times after thermal denaturation.

Table S1. Sequences of the coiled coil A_4B_4 heterodimer (CC-Hetero2). Thermodynamic stability of the A_4B_4 heterodimer (i.e. melting temperature) measured in the literature was used [113].

CC peptides	Sequence	Abbreviation
	gabcdef gabcdef gabcdef gabcdef	
CC-Hetero2, A_4	Ac-CGG EIAALEQ EIAALEK ENAALEW EIAALEQ GG-NH$_2$	CC-Hetero2
CC-Hetero2, B_4	Ac-CGG KIAALKQ KIAALKY KNAALKK KIAALKQ GG-NH$_2$	

Table S2. Melting temperatures (T_m) of the CMPs reported in the literatures. The $(PPG)_{10}$ and $(POG)_{10}$ peptide solutions were prepared in neutral pH and the $(POG)_7$ peptide solution was prepared in an acidic condition with acetic acid (HOAc). The concentrations of the solutions were not identical.

CMPs	T_m	Peptide concentration	Buffer condition	Literature
$(PPG)_{10}$	24.5~32.4 °C	1 mg ml^{-1}	PBS (pH 7.0)	[103]
$(POG)_7$	34 °C	0.2 mM	HOAc (pH 2.9)	[92]
$(POG)_{10}$	57.0~60.2 °C	1 mg ml^{-1}	PBS (pH 7.0)	[103]

Table S3. Apparent dissociation rates of the CMPs obtained from the CD Temperature-jump experiments. The rate constants were obtained with linear regressions from the initial slopes of the CD curves (**Figure S4**) as described in **Methods**.

CMPs	T (K)	k_{off}^{app} Meas.1 (s^{-1})	k_{off}^{app} Meas.2 (s^{-1})	k_{off}^{app} Meas.3 (s^{-1})	k_{off}^{app} Average (s^{-1})	Standard deviation	Standard error
	290.02±0.21	1.58 E-05	1.50 E-05	1.48 E-05	1.52 E-05	5.50 E-07	2.04 E-08
	293.45±0.15	2.51 E-05	2.63 E-05	2.68 E-05	2.61 E-05	8.60 E-07	3.18 E-08
$(PPG)_{10}$	296.22±0.36	3.36 E-05	3.57 E-05	3.73 E-05	3.55 E-05	1.88 E-06	6.95 E-08
	298.82±0.20	4.74 E-05	5.45 E-05	5.11 E-05	5.10 E-05	3.51 E-06	1.30 E-07
	301.48±0.06	7.88 E-05	8.16 E-05	8.83 E-05	8.29 E-05	4.87 E-06	1.80 E-07
	288.15±0.17	1.78 E-05	1.80 E-05	9.65 E-06	1.52 E-05	4.79 E-06	5.32 E-07
	290.92±0.06	2.78 E-05	3.67 E-05	3.03 E-05	3.16 E-05	4.59 E-06	5.10 E-07
$(POG)_7$	293.08±0.04	2.48 E-05	3.93 E-05	3.92 E-05	3.45 E-05	8.36 E-06	9.28 E-07
	295.68±0.06	4.25 E-05	5.01 E-05	4.75 E-05	4.67 E-05	3.88 E-06	4.31 E-07
	298.05±0.17	5.67 E-05	6.48 E-05	5.87 E-05	6.00 E-05	4.23 E-06	4.70 E-07
	323.05±0.00	1.36 E-05	1.25 E-05	1.57 E-05	1.39 E-05	1.63 E-06	1.81 E-07
	325.05±0.10	2.40 E-05	1.50 E-05	1.33 E-05	1.74 E-05	5.76 E-06	6.40 E-07
$(POG)_{10}$	327.05±0.20	3.17 E-05	2.17 E-05	2.84 E-05	2.73 E-05	5.12 E-06	5.69 E-07
	328.75±0.10	3.67 E-05	3.97 E-05	3.21 E-05	3.61 E-05	3.82 E-06	4.24 E-07
	330.58±0.06	6.56 E-05	5.90 E-05	5.53 E-05	5.99 E-05	5.20 E-06	5.78 E-07

Table S4. Viscoelastic parameters of the CMP-crosslinked hydrogels measured from the amplitude sweeps. The three individual batches of the hydrogels were prepared for the measurements. For the amplitude sweeps, the strain amplitudes were varied from 0.1 % to 1000 % while applying an angular frequency of 10 rad s^{-1}. The amplitude sweeps were performed two times, but the parameters were obtained from the second sweeps only.

CMPs	sample batch	G_p (Pa)	LVER (%)	Flow point (%)
(PPG)$_{10}$	1	2935	27	52
	2	2381	14	37
	3	2810	7	27
(POG)$_7$	1	895	100	268
	2	824	100	268
	3	877	100	268
(POG)$_{10}$	1	2340	52	100
	2	2428	37	139
	3	1396	52	139

Table S5. Relaxation times and relaxation exponents of the (POG)$_{10}$-crosslinked hydrogels from the stress relaxation tests of 5 repeats. 5 different batches of the (POG)$_{10}$-crosslinked hydrogels were prepared independently and the relaxation times and the relaxation exponents were obtained using the KWW equation to find the overall trend of the relaxation times and the relaxation exponents with different waiting times (**Figure S6**).

		aging	1min	10min	20min	25min	30min	60min
1st	τ (s)			20,727	5,144	13,341	7,692	5,337
	α (-)			1.42	1.3	0.88	0.87	0.65
2nd	τ (s)		6,547	13,548	10,807		3,481	7,030
	α (-)		1.13	1.13	1.19		0.57	0.62
3rd	τ (s)			24,807	23,883		23,094	18,152
	α (-)			1.35	1.22		0.94	0.92
4th	τ (s)			17,237			7,882	16,619
	α (-)			1.13			0.79	0.92
5th	τ (s)		35,208	26,379	17,769		7,281	10,012
	α (-)		1.27	1.55	1.32		0.78	0.85
average	τ (s)		**20,878**	**20,540**	**14,401**	**13,341**	**9,886**	**11,430**
	α (-)		**1.20**	**1.32**	**1.26**	**0.88**	**0.79**	**0.79**

Table S6. Melting temperatures of the CC peptides. Thermal denaturation of the CC-Homo2, CC-Homo3, and CC-Homo4 were measured using CD spectroscopy. The melting temperatures were obtained using Global 3 software (Applied Photophysics Ltd, Leatherhead, England, see **Methods**) from the thermal denaturation curves. All the peptides were prepared in PBS (pH 7.4) and stored at 4 °C for over 48 h. The CD thermal denaturation measurements were performed with a temperature range from 4 °C to about 90 °C at the heating rate of 1 °C per minute. The Global 3 fitting was done based on the derivative method with 1 transition curve and two baselines correction.

	$T_{m,meas.}$ (°C)	$T_{m,lit.}$ [85] (°C)
Homo2	69.0 ± 0.1	78.15
Homo3	51.8 ± 0.1	56.47
Homo4	No fitting result (T_m > 90 °C)	> 90

Table S7. Relaxation times of the CC-crosslinked hydrogels obtained from the frequency sweeps. 4-arm star-PEG was used for all the hydrogels. The critical frequency (ω_c in Hz) was obtained at the crossover point (G' = G'') during the frequency sweeps (**Figure S10**) and the frequency in Hz (s^{-1}) was calculated from the angular frequency (rad s^{-1}) to obtain the relaxation times with the relationship of $\tau_{FS} = 1/\omega_c$.

CCs Relation parameters	Hetero2	Homo2	Homo3	Homo4
crossover frequency, ω_c [rad s^{-1}]	0.0268	0.0072	-	-
Relaxation times, τ [s]	230	870	-	-

Acknowledgements